

Thesis to obtain the academic degree  
Master of Science

**Edge Modes in  
Magnet-Superconductor Hybrid  
Structures**

Jasmin Bedow  
born in Essen

2020

Lehrstuhl für Theoretische Physik I  
Fakultät Physik  
Technische Universität Dortmund

Department of Physics  
University of Illinois at Chicago

First Corrector: Prof. Dr. Götz S. Uhrig  
Second Corrector: Prof. Dr. Dirk K. Morr  
Date of Submission: August 12th, 2020

## Abstract

Topological superconductivity and the ensuing Majorana zero modes form the basis of topological quantum computing due to their non-Abelian braiding statistics. Magnet-superconductor hybrid (MSH) structures can nowadays be custom-engineered through atomic manipulation and interface engineering techniques. Experimentally, these structures have been proven to exhibit topological superconductivity as well as chiral edge modes emerging in two-dimensional MSH systems or zero-energy vortex bound states occurring at the center of a vortex core in a topological superconductor. In this thesis, we show from a theoretical perspective that topological superconductivity is a robust phenomenon in two-dimensional MSH structures with non-collinear spin structures, namely the recently experimentally discovered triple-Q (3Q) structure as well as a magnetic skyrmion lattice. Furthermore, the emergence of chiral Majorana edge modes at domain walls is investigated. Here, it is demonstrated that topological edge modes can be distinguished from trivial in-gap states through the relative spatial orientations of the occurring supercurrents at the domain wall. Finally, the reactions of a metallic and superconducting system towards magnetic perturbations are discussed, in order to lay the foundations for a theoretical description of moving vortex cores. As these vortex cores possess a localized Majorana zero-energy mode at their center, this could be a future realization of braiding operations of Majorana zero-energy modes, which are a necessity for the realization of topological quantum computation. For this purpose, the induced currents between a singular perturbed metallic or superconducting system site and a scanning tunneling microscopy (STM) tip are simulated as well as the perturbed superconducting order parameter for the case of a superconducting system site.

## Kurzfassung

Topologische Supraleitung und die zugehörigen Majorana Moden bilden die Basis zur Realisierung eines topologischen Quantencomputers aufgrund ihrer nicht-abelschen Vertauschungsrelationen. Magnet-Supraleiter Hybrid Strukturen sind hierfür vielversprechende Kandidaten, die inzwischen individuell erstellt werden können mittels Atomic Manipulation-Methoden und Interface Engineering-Techniken. Experimentell wurde bestätigt, dass sowohl zweidimensionale Beispiele solcher MSH Strukturen chirale Majorana Moden aufzeigen, aber auch sogenannte Null-Energie Vortex Bound States, in Form einer lokalisierten Majorana Mode, im Zentrum eines Vortex in einem topologischen Supraleiter auftreten.

In der nachfolgenden Arbeit wird zunächst für zweidimensionale MSH Strukturen

---

mit nicht kollinearen Spinstrukturen theoretisch gezeigt, dass topologische Supraleitung auftritt und diese ein robustes Phänomen darstellt. Dies wird sowohl für die vor kurzem experimentell entdeckte 3Q Struktur als auch für ein Gitter magnetischer Skyrmionen durchgeführt. Desweiteren wird untersucht, welche Art von Domänenwänden in solchen Strukturen zum Auftreten chiraler Majorana Moden führt. Hier wird demonstriert, dass solche topologischen Randmoden von trivialen In-Gap-Zuständen mithilfe der räumlichen Verteilung der auftretenden Superströme an der Domänenwand unterschieden werden können.

Zuletzt werden die Reaktionen jeweils eines metallischen und eines supraleitenden Systems auf magnetische Störungen untersucht, um die Grundlagen einer theoretischen Beschreibung für bewegte Vortex-Zentren zu legen. Da eine Majorana Mode in deren Zentrum lokalisiert ist, ergibt sich durch dieses Vorgehen ein Kandidat für die Realisierung der Vertauschungsoperationen. Diese sind zwingend notwendig für den Erfolg topologischer Quantencomputer. Zu diesem Zweck werden die induzierten Ströme zwischen einem einzelnen Gitterplatz eines metallischen oder supraleitenden Systems und einer STS Spitze simuliert. Darüber hinaus wird für den Fall des supraleitenden Systems die Zeitabhängigkeit des supraleitenden Ordnungsparameters berechnet.

## List of Publications

Parts of this thesis have been submitted to:

1. E. Mascot, J. Bedow, M. Graham, S. Rachel, and D. K. Morr  
*Topological Superconductivity in Skyrmion Lattices* (2020)  
<https://arxiv.org/abs/2005.00027>
2. J. Bedow, E. Mascot, T. Posske, G. S. Uhrig, R. Wiesendanger, S. Rachel, and D. K. Morr  
*Topological superconductivity induced by a triple-Q magnetic structure* (2020)  
<https://arxiv.org/abs/2006.02039>

These manuscripts were written during the course of my Master's thesis and contain some of the major results presented in this work.

# Table of Contents

<b>1</b>	<b>Introduction</b>	<b>1</b>
<b>2</b>	<b>Theoretical Methods for Magnet-Superconductor Hybrid Structures</b>	<b>4</b>
2.1	Theoretical Model . . . . .	4
2.2	Topological Invariants and Phase Transitions . . . . .	5
2.3	The Chern Number and the Bulk-Boundary Correspondence . . . . .	7
2.4	Local Density of States . . . . .	9
2.5	Supercurrents . . . . .	10
<b>3</b>	<b>The Magnetic Triple-Q Structure</b>	<b>14</b>
3.1	Spin Structure . . . . .	14
3.1.1	Effective Rashba Spin-Orbit Coupling . . . . .	15
3.2	Band Structure . . . . .	18
3.2.1	Symmetry Transformation . . . . .	20
3.3	Topological Phase Diagram . . . . .	23
3.4	Edge Modes on Magnetic Islands . . . . .	27
3.4.1	Circular Islands . . . . .	27
3.4.2	Introducing Disorder . . . . .	29
3.4.3	Supercurrents . . . . .	30
3.5	Edge Modes on Ribbon Structures . . . . .	32
3.5.1	Introducing Disorder . . . . .	34
3.5.2	Theoretical Method for Partially Infinite Systems . . . . .	35
3.5.3	Band Structure . . . . .	37
3.5.4	Local Density of States . . . . .	38
3.6	Experimentally Motivated Model . . . . .	39
3.6.1	AB-Stacked Spin Structure without Electronic Degrees of Freedom . . . . .	40
3.6.2	Hamiltonian for Spins with Electronic Degrees of Freedom . . . . .	41
3.6.3	Band Structure . . . . .	42
3.6.4	Topological Phase Diagram . . . . .	46
<b>4</b>	<b>Magnetic Skyrmions</b>	<b>50</b>
4.1	Spin Structure . . . . .	51
4.2	Phase Diagram . . . . .	52

---

4.3	Edge Modes in Ribbon Structures . . . . .	53
4.3.1	Band Structure . . . . .	53
4.3.2	Local Density of States . . . . .	53
4.3.3	Supercurrents . . . . .	55
<b>5</b>	<b>Domain Walls</b>	<b>58</b>
5.1	Domain Walls Created from Shifts of the Spin Structure . . . . .	59
5.2	Domain with an Inverted Spin Structure . . . . .	60
5.3	Domain with an Inverted Superconducting Order Parameter . . . . .	62
<b>6</b>	<b>Non-Equilibrium Magnetic Perturbations</b>	<b>65</b>
6.1	Metallic System . . . . .	65
6.1.1	Theoretical Method . . . . .	66
6.1.2	Result for the Induced Current . . . . .	70
6.2	Superconducting System . . . . .	71
6.2.1	Time Dependence of the Induced Current for Constant Per- turbations . . . . .	73
6.2.2	Time Dependence of the Induced Current for Instantaneous Perturbations . . . . .	80
6.2.3	Time Dependence of the Superconducting Order Parameter for Instantaneous Perturbations . . . . .	81
<b>7</b>	<b>Conclusion and Outlook</b>	<b>89</b>
	<b>Bibliography</b>	<b>92</b>



# 1 Introduction

Majorana fermions, exotic particles that are their own antiparticle, have been an object of interest in particle physics since they were predicted in 1937 [1]. More recently, these particles also raised the interest of condensed matter physicists in the context of topological superconductivity. Here, Majorana zero-energy modes occur, which can be employed as a new platform of topological quantum computing due to their robustness against local decoherence effects [2]. The basis of this type of quantum computing is formed by the non-Abelian braiding statistics of Majorana zero modes [3, 4]. However, in order to make use of these, the ability to create, control and manipulate topological superconducting phases is a necessity. The first, theoretical example of a topological superconductor was the Kitaev chain [5], which is a chain of electronic sites that exhibit  $p$ -wave superconductivity. This system is depicted in Fig. 1.1 (a). Here, two Majorana modes can be perceived as edge modes when the electrons at each site are expressed in terms of two Majorana fermions. In the topological phase, one can rearrange two Majorana fermions from neighboring sites into an electron, leaving two Majorana fermions at the ends of the chain, as depicted in Fig. 1.1 (b).

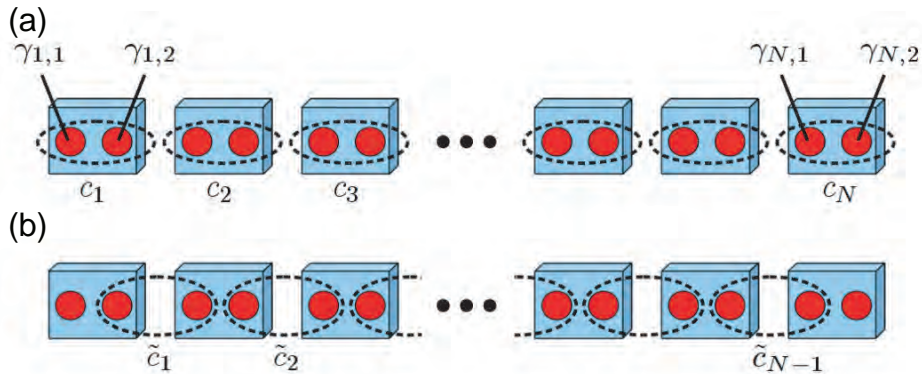


**Fig. 1.1:** Kitaev chain (a) in the trivial phase with each electron  $c_i$  separated into two Majorana fermions  $\gamma_{i,1}$  and  $\gamma_{i,2}$ , (b) in the topological phase, where the Majorana fermions couple to one at a neighboring site leaving two edge modes [4].

However, as materials exhibiting  $p$ -wave superconductivity are rare, experimentally more realizable systems are required. Promising candidates avoiding this problem are

magnet-superconductor hybrid (MSH) systems. In this approach, a layer of magnetic adatoms is placed onto a substrate with *s*-wave superconductivity. Through the proximity effect, superconductivity is also induced within the magnetic layer.

In both theoretical [6–9] and experimental [10–13] investigations of one-dimensional MSH structures, topological superconductivity has been found and the expected Majorana zero modes have been observed. Following this progress in one dimension, two-dimensional MSH structures have been analyzed from theoretical [14–17] and experimental [18–22] points of view as well, which exhibit chiral Majorana edge modes. Still, the engineering of these modes at the atomic level and their clear identification remain a problem.

Atomic manipulation techniques [13] and interface engineering techniques [23] enable the construction of MSH structures and thereby the design of topological superconductors. Thereby, chains of magnetic adatoms in one dimension, so-called Shiba chains, or islands of magnetic adatoms in two dimensions, so-called Shiba islands, can be constructed. The emerging edge modes can be investigated using scanning tunneling spectroscopy (STS) [23].

MSH systems with non-collinear magnetic structures, such as skyrmions, have raised great interest, as they do not only exhibit topological superconductivity, but also enable tuning between different topological phases by varying the skyrmion radius [24]. The wide range of possibilities they offer, originates from a spatially inhomogeneous, effective Rashba spin-orbit coupling. As this coupling is induced by the magnetic skyrmion lattice, there is no need for a material with a Rashba spin-orbit coupling in experimental realizations. In this thesis, some of the topological properties of these helical spin structures in real-space models are assessed.

Furthermore, the recent experimental advance in creating an MSH system, where a triple-Q (3Q) magnetic structure [25] was deposited on the surface of an *s*-wave superconductor [26] in Mn/Re (0001), creates the question whether this spin structure also exhibits topological superconductivity below the critical temperature for superconductivity. In addition, a theoretical prediction, which type of domain wall can be employed to engineer Majorana modes, can be tested experimentally due to the observation of domain walls in FeSe<sub>0.45</sub>Te<sub>0.55</sub> [22]. These domain walls can be of structural, electronic or magnetic character. Assessing this outstanding question also helps in determining how topological modes can be distinguished from trivial in-gap states, which is thereby an important step towards the unambiguous identification of topological states.

In the end, a realization for the braiding of Majorana zero modes also remains an unanswered question in need of a solution. Vortices in superconductors for example are predicted theoretically to exhibit a Majorana fermion at their core [27–30], which was already shown experimentally [20], enabling the creation and control of Majorana modes. Recent experimental advances allow for these vortices to be moved dynamically, presenting a possible strategy of manipulating them at will. However, if

---

this approach is to develop into a strategy towards the braiding of Majorana modes, a theoretical construct is required for this type of mechanism.

In chapter 2.1, the theoretical methods for the study of magnet-superconductor hybrid structures will be introduced. In the following chapter, the spatial structure and the symmetries of the 3Q magnetic structure will be presented. Next, the band structure and phase diagram of an MSH structure with the 3Q spin structure employed will be discussed for a simple as well as an experimentally motivated model. Furthermore, the occurrence of edge modes in real-space structures such as magnetic islands and ribbons will be investigated.

Based on this assessment of the 3Q structure, chapter 4 then studies the topological properties of a magnetic skyrmion lattice. For this ordering of the magnetic layer, the occurring edge modes on magnetic ribbons will be analyzed as well.

Chapter 5 then provides an overview which domain walls lead to edge modes and explores the question whether these are Majorana zero-energy modes or trivial modes. Finally, chapter 6 focuses on a method for the analysis of magnetic perturbations applied to metallic and superconducting sites in real-time, in order to lay the foundation for the simulation of perturbations moving in space.

## 2 Theoretical Methods for Magnet-Superconductor Hybrid Structures

### 2.1 Theoretical Model

In order to study the topological phase diagram of an MSH structure, the starting point here is a model where the spins of the magnetic layer are placed directly above the atoms of the superconducting substrate. This kind of model is described through the Hamiltonian

$$\mathcal{H} = \mathcal{H}_0 + \mathcal{H}_m \quad (2.1a)$$

with

$$\mathcal{H}_0 = -t \sum_{\mathbf{r} \in A, \delta, \sigma} c_{\mathbf{r}, \sigma}^\dagger \tau_z \otimes \sigma_0 c_{\mathbf{r} + \delta, \sigma} - \mu \sum_{\mathbf{r} \in A, \sigma} c_{\mathbf{r}, \sigma}^\dagger c_{\mathbf{r}, \sigma} + \sum_{\mathbf{r}} \left( \Delta c_{\mathbf{r}, \uparrow}^\dagger c_{\mathbf{r}, \downarrow}^\dagger + \text{h.c.} \right), \quad (2.1b)$$

$$\mathcal{H}_m = J \sum_{\mathbf{r} \in A, \alpha, \beta} c_{\mathbf{r}, \alpha}^\dagger (\mathbf{S}_{\mathbf{r}} \cdot \boldsymbol{\sigma})_{\alpha\beta} c_{\mathbf{r}, \beta}, \quad (2.1c)$$

where  $-t$  is the hopping parameter between nearest neighboring sites connected by the vector  $\boldsymbol{\delta}$ ,  $\mu$  is the chemical potential,  $J$  is the strength of the magnetic exchange coupling and  $\Delta$  is the superconducting  $s$ -wave order parameter. On the chosen lattice denoted by  $A$ , an electron of spin  $\sigma$  is created by the fermionic creation operator  $c_{\mathbf{r}, \sigma}^\dagger$ . In the following, a triangular lattice is chosen in contrast to a quadratic one, because the investigated non-collinear spin ordering only corresponds to the ground state of the system on a triangular lattice.

$\mathbf{S}_{\mathbf{r}}$  is the spin  $S$  of the magnetic moment at the site  $\mathbf{r}$  of the lattice, which thereby encodes the chosen ordering of the magnetic layer. As the hard superconducting gap suppresses Kondo screening, the magnetic moments are represented by classical spins. This approximation is valid, provided the spin of the adatoms is sufficiently large [31, 32]. Furthermore, in this model the Fermi energy  $E_F$  is set to zero for simplicity. Finally,  $\boldsymbol{\sigma} = (\sigma_x, \sigma_y, \sigma_z)^T$  is a vector containing all three of the Pauli matrices

$$\sigma_x = \begin{pmatrix} 0 & 1 \\ 1 & 0 \end{pmatrix} \quad \sigma_y = \begin{pmatrix} 0 & -i \\ i & 0 \end{pmatrix} \quad \sigma_z = \begin{pmatrix} 1 & 0 \\ 0 & -1 \end{pmatrix}. \quad (2.2)$$

## 2.2 Topological Invariants and Phase Transitions

Topological properties of quantum states of matter have become of great interest in condensed matter physics since the discovery of the integer quantum Hall effect [33]. Before, topology was already an established field in mathematics, which assesses the global properties of a geometrical object that are preserved under continuous deformations. Such deformations include stretching, bending or twisting, in contrast to tearing or gluing. Here, tearing or gluing are examples of non-adiabatic processes, which are the only way of changing these global properties. Therefore, they are characterized by discrete topological invariants. As the global properties are linked to the intrinsic structure of the investigated system, the invariants have to be inextricably connected to them as well and have to be preserved under adiabatic local transformations. Thereby, two objects are called topologically equivalent when they can be transformed into one another through this type of transformation. Then, their topological invariants have the same values.

A concrete example of this principle can be constructed using the genus  $g$  of an orientable surface. It corresponds to the number of holes in the surface and thereby is intuitive to understand. For example, a sphere such as a basketball has no holes and therefore has genus  $g = 0$ , while a bagel and a cup each have one hole implying  $g = 1$  for them. Thus, the bagel can be transformed into the cup continuously, but not into the basketball. Overall, the genus can only be changed by integer amounts, when holes are added or removed. Thereby, the bagel and the basketball are assigned to different topological classes, while the bagel and the cup belong the same class. In the following, a similar topological invariant, the Chern number, is employed to characterize the investigated system from section 2.1.

Following the discovery of the integer quantum Hall effect in 1980 by von Klitzing [34] and the following theoretical explanation by Thouless, Kohmoto, Nightingala and den Nijs in 1983 [35], the research on topological phases became one of the most popular branches in condensed matter physics. In the integer quantum Hall effect, the Hall conductance changes in a step-wise manner in response to a reduction of the applied strength of the magnetic field. This behaviour was theoretically described through the TKNN integer [35], in order to classify the quantum Hall states, which occur on the boundary of the system. These edge states were shown to be exponentially localized at the boundary of the system. The number of occurring edge states corresponds to the Chern number  $C$  [36, 37] of the filled electronic bands, which also renders the well-known quantized Hall conductivity  $\sigma_{xy} = C \frac{e^2}{h}$ , where  $e$  is the electric charge.

Since then, the number of different topological materials and phases has increased rapidly. In condensed matter physics, the topological invariants in question stem

from the properties of the Hamiltonian. Here, a topological phase with a symmetry-protected topological order, which is the case we are interested in here, although there are also others, is described by a finite energy gap and certain symmetries in the system. This kind of phase cannot be continuously deformed into a different phase, as long as the energy gap and the symmetries are preserved [38]. Thereby, the topological nature of the phase creates the necessity to close the energy gap in order to change the phase. Here, topological superconductors are investigated, which are well-known examples of topological phases with a symmetry-protected order. They are defined as superconductors, in which a topological invariant takes a non-trivial value.

These topological invariants, like the genus of an oriented surface, can only be changed by non-adiabatic processes. Thereby, a quantum phase transition between different phases implies that the gap between distinct phases is closed and then opened again, as depicted in Fig. 2.1.

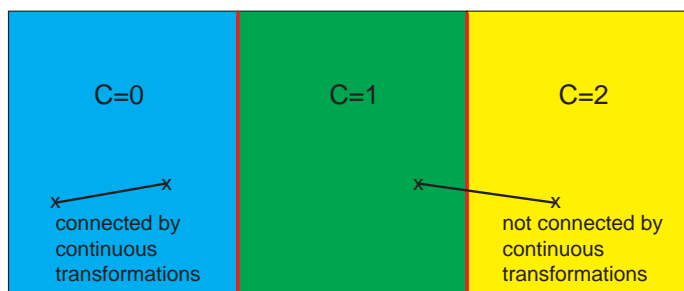


**Fig. 2.1:** Schematic plot of distinct topological phases, where  $C$  refers to the topological invariant describing the investigated system. All three phases share the same symmetries. The phase transitions between different phases, where a gap has to be closed and opened again, are marked in red.

The topology of the phase stems not from the eigenenergies of the system, but is rooted in the eigenstates. Therein, a non-trivial value of a topological invariant leads to the emergence of conducting edge modes, which is explained by the bulk-boundary correspondence [39–42].

Depending on the dimensionality of the system and the present symmetries, numerous possibilities exist for topological superconductors and topological insulators, which are illustrated in the periodic table introduced by Kitaev [43]. Therein, Altland and Zirnbauer [44, 45] pointed out that all possibilities are classified into ten unique classes, which are characterized by the eigenvalues of the squares of the time-reversal

$\mathcal{T}$ , particle-hole  $\mathcal{C}$  and chiral symmetry operators  $\mathcal{S}$ . An excerpt of this table up to three dimensions, which applies to fermionic systems, is shown below in Tab. 2.1 [46].

As can be seen here, the Hamiltonian from section 2 corresponds to a class D topological superconductor, as the particle-hole symmetry is preserved in the system and the spins break the time-reversal symmetry. Thereby, the appropriate topological invariant for this system, the Chern number, takes integer values. In the following section, this invariant and its calculation will be explained. Furthermore, the implied consequences of the bulk-boundary correspondence are introduced.

	class	$\mathcal{T}^2$	$\mathcal{C}^2$	$\mathcal{S}^2$	$d = 1$	$d = 2$	$d = 3$
Wigner-Dyson symmetry classes	A	-	-	-	-	$\mathbb{Z}$	-
	AI	+1	-	-	-	-	-
	AII	-1	-	-	-	$\mathbb{Z}_2$	$\mathbb{Z}_2$
chiral symmetry classes	AIII	-	-	1	$\mathbb{Z}$	-	$\mathbb{Z}$
	BDI	+1	+1	1	$\mathbb{Z}$	-	-
	CII	-1	-1	1	$\mathbb{Z}$	-	$\mathbb{Z}_2$
Bogoliubov - de Gennes symmetry classes	D	-	+1	-	$\mathbb{Z}_2$	$\mathbb{Z}$	-
	C	-	-1	-	-	$\mathbb{Z}$	-
	DIII	-1	+1	1	$\mathbb{Z}_2$	$\mathbb{Z}_2$	$\mathbb{Z}$
	CI	+1	-1	1	-	-	$\mathbb{Z}$

**Table 2.1:** Separation of all possible topological insulators and topological superconductors for non-interacting fermionic Hamiltonians into the ten symmetry classes [46]. The different cases are distinguished by the spatial dimension  $d \in \{1, 2, 3\}$  as well as the eigenvalues of three discrete symmetries, namely the time-reversal symmetry  $\mathcal{T}$ , the particle-hole symmetry  $\mathcal{C}$  and the chiral symmetry  $\mathcal{S}$ . The case that a symmetry is absent is denoted by -. A present symmetry is indicated by  $\pm 1$ , which corresponds to the system's transformation behavior under twofold application of the symmetry operation.

## 2.3 The Chern Number and the Bulk-Boundary Correspondence

The Chern number was originally employed in mathematics for the description of fiber bundles [47]. Its significance in physics was discovered as part of the theoretical

description of the integer quantum Hall effect by Thouless, in which context it was known as the TKNN integer [35]. Its connection to the Chern number was established in 1985 [36].

For the  $n$ -th band, the Chern number is defined as

$$C^{(n)} = \frac{1}{2\pi} \int_{\text{BZ}} dk_x dk_y F_{xy}^{(n)}(\mathbf{k}) \quad (2.3)$$

with the field strength of the Berry connection  $F_{xy}^{(n)}(\mathbf{k}) = \partial_{k_x} \langle u_n(\mathbf{k}) | \partial_{k_y} u_n(\mathbf{k}) \rangle - \partial_{k_y} \langle u_n(\mathbf{k}) | \partial_{k_x} u_n(\mathbf{k}) \rangle$  [42]. Here, the eigenstates  $|u_n(\mathbf{k})\rangle$  of the Hamiltonian are required for the calculation.

When this formula is summed over all bands of the Hamiltonian, an alternative way of calculation [48] is

$$C = \frac{1}{2\pi i} \int_{\text{BZ}} d^2k \text{Tr} \{ P_{\mathbf{k}} [\partial_{k_x} P_{\mathbf{k}}, \partial_{k_y} P_{\mathbf{k}}] \} \quad (2.4)$$

with the projection operator

$$P_{\mathbf{k}} = \sum_{E_n(\mathbf{k}) < 0} |u_n(\mathbf{k})\rangle \langle u_n(\mathbf{k})|. \quad (2.5)$$

As mentioned in the previous section, this topological invariant can only change when the system's energy gap closes, for example when a band crosses the level of the Fermi energy due to a change of parameters. By calculating the Chern number for different parameter sets, the phase diagram can be calculated for a specific MSH structure. The phase transitions of the corresponding Hamiltonian can be found by observing its gap closings, which separate the parameter space into regions of different values for the Chern number.

For the case of MSH structures, there are two prerequisites that have to be fulfilled, so that non-trivial values of the Chern number can occur. Firstly, an effective Rashba spin-orbit coupling  $\alpha$  has to be present. However, this interaction can also be induced intrinsically through non-collinear spin structures. As will be discussed later, this can be shown through a local gauge transformation.

Secondly, the magnetic exchange coupling  $J$  has to be greater than the chosen superconducting order parameter  $\Delta$ . Because time-reversal symmetry is preserved for  $J = 0$ , the system is then in a trivial phase. In order to reach a topological phase, the gap first has to be closed. This is achieved at a critical value for the magnetic exchange coupling  $J$ , which is reached approximately at the magnitude of the superconducting order parameter [49, 50]. As a consequence, only trivial phases were observed so far in MSH structures with ferromagnetic spins for  $J < \Delta$  [16] and this also holds for the spin structures that are discussed in chapters 3 and 4.

Furthermore, the fact that the Chern number can only change when the gap of the Hamiltonian closes, is a consequence of the bulk-boundary correspondence [39]. It states that when a trivial phase of  $C = 0$  is placed next to a topological phase of  $C \neq 0$ , as shown in Fig. 2.2.

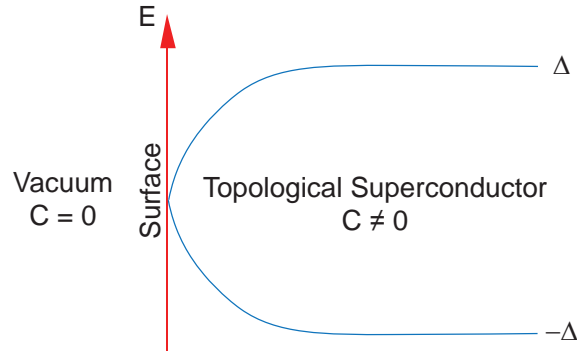


**Fig. 2.2:** Schematic depiction of the bulk-boundary correspondence [51].

Therefore, the bulk gap of the Hamiltonian must close, which results in the emergence of edge modes with an energy equal to zero. Transferred to the example of Magnet-Superconductor Hybrid structures, the common case will be for a magnetic layer to be placed onto a superconducting substrate. As this will be done experimentally through atomic manipulation techniques, a finite number of magnetic adatoms is put on top of the substrate. The rest of the superconducting substrate, which is left uncovered by magnetic adatoms, is in a trivial phase. Therefore when the hybrid structure composed of magnetic adatoms and the superconducting substrate is in a topological phase, the border of the magnetic layer forms a boundary between a topological and a trivial phase. Accordingly, on the edge of the magnetic structure, edge modes will form that can be observed experimentally and simulated theoretically through the quantities introduced in the following section, the local density of states as well as the supercurrents. These occurring edge modes are Majorana modes [15], analogous to the Kitaev model [5] and for two-dimensional systems exhibiting chiral  $p$ -wave superconductivity [29, 52, 53]. As they are thereby their own antiparticle, they have an energy equal to zero.

## 2.4 Local Density of States

One possibility to observe the existence of Majorana modes is by measuring the local density of states (LDOS). This quantity can be employed to illustrate where the

eigenmodes of the Hamiltonian are located spatially at a specific energy. Due to the fact that the edge modes in question are located at the boundary of the system according to the bulk-boundary correspondence, the LDOS can be employed to check for their occurrence on the boundary of the magnetic layer. As Majorana fermions are their own antiparticle, these modes are found at zero energy and thus the LDOS needs to be calculated at an energy of  $E = 0$ .

The LDOS  $N_i(\mathbf{r})$ , where  $i \in \{0, 1, 2, 3\}$  refers to an index in Nambu space, can be derived from the imaginary part of the retarded Green's function as

$$N_i(\mathbf{r}) = -\frac{1}{\pi} \text{Im}[g_{i,i}^R(\mathbf{r}, \mathbf{r}, \omega)], \quad (2.6)$$

where the retarded Green's function is obtained [54] by first diagonalizing the Hamiltonian to find the eigenenergies  $E_k$  and eigenstates  $u_{k,i}(\mathbf{r})$  and inserting them into

$$g_{i,j}^R(\mathbf{r}, \mathbf{r}', \omega) = \sum_k u_{k,i}(\mathbf{r}) u_{k,j}^*(\mathbf{r}') \frac{1}{\omega - E_k + i\delta}. \quad (2.7)$$

The index  $k \in \{1, 2, \dots, \dim \hat{H}\}$  is used here as a counting index for the different eigenenergies of the eigenmodes in real space. Here,  $\dim \hat{H}$  refers to the dimension of the matrix representation  $\hat{H}$  of the Hamiltonian in a finite-sized system. The imaginary part is then given by

$$\text{Im} [g_{i,j}^R(\mathbf{r}, \mathbf{r}', \omega)] = \sum_k u_{k,i}(\mathbf{r}) u_{k,j}^*(\mathbf{r}') \frac{\delta}{(E_k - \omega)^2 + \delta^2} \quad (2.8a)$$

$$= \pi \sum_k u_{k,i}(\mathbf{r}) u_{k,j}^*(\mathbf{r}') \delta(E_k - \omega) \quad (2.8b)$$

for  $\delta \rightarrow 0^+$ . Over the course of this thesis, the two electronic components of the LDOS  $N_i(\mathbf{r})$ , which correspond to  $i = 0 = \uparrow$  and  $i = 1 = \downarrow$ , are summed over, yielding the total LDOS

$$N(\mathbf{r}) = N_{\uparrow}(\mathbf{r}) + N_{\downarrow}(\mathbf{r}). \quad (2.9)$$

## 2.5 Supercurrents

Supercurrents are defined as currents that flow in the system even when no voltage is applied to it from the outside of the system. In general, the supercurrent [16] between two sites  $\mathbf{r}, \mathbf{r}'$  is obtained from

$$I_{\mathbf{r},\mathbf{r}'}^i = -\frac{2e}{\hbar} \int \frac{d\omega}{2\pi} \text{Re} [t_{\mathbf{r},\mathbf{r}'}^{ii} g_{i,i}^{<}(\mathbf{r}, \mathbf{r}', \omega)] , \quad (2.10)$$

where  $t_{\mathbf{r},\mathbf{r}'}^{ij}$  refers to the hopping parameter between sites  $\mathbf{r}$  and  $\mathbf{r}'$ , with  $(i, j)$  referring to indices in Nambu space. In Eq. (2.10), only diagonal elements of the supercurrent in Nambu space are taken into account, because the Hamiltonian in Eq. (2.1c) does not contain any spin-flipping processes. In Nambu space, the spinor for one site  $\mathbf{r}$  is given as  $\Psi_{\mathbf{r}} = (c_{\mathbf{r},\uparrow}^\dagger, c_{\mathbf{r},\downarrow}^\dagger, c_{\mathbf{r},\downarrow}, -c_{\mathbf{r},\uparrow})$ . In real time, the greater, lesser, retarded and advanced Green's functions are respectively given as

$$g_{i,j}^>(\mathbf{r}, \mathbf{r}', t) = -i \left\langle (\Psi_{\mathbf{r}})_i(t) (\Psi_{\mathbf{r}'}^\dagger)_j(0) \right\rangle, \quad (2.11a)$$

$$g_{i,j}^<(\mathbf{r}, \mathbf{r}', t) = i \left\langle (\Psi_{\mathbf{r}'}^\dagger)_j(0) (\Psi_{\mathbf{r}})_i(t) \right\rangle, \quad (2.11b)$$

$$g_{i,j}^R(\mathbf{r}, \mathbf{r}', t) = -i\Theta(t) \left\langle \left\{ (\Psi_{\mathbf{r}})_i(t), (\Psi_{\mathbf{r}'}^\dagger)_j(0) \right\} \right\rangle \quad (2.11c)$$

and

$$g_{i,j}^A(\mathbf{r}, \mathbf{r}', t) = i\Theta(-t) \left\langle \left\{ (\Psi_{\mathbf{r}})_i(t), (\Psi_{\mathbf{r}'}^\dagger)_j(0) \right\} \right\rangle, \quad (2.11d)$$

where  $\hbar$  is set to unity during the course of the calculation of  $g_{i,i}^<(\mathbf{r}, \mathbf{r}', \omega)$ . From these formulas, we directly obtain the relations

$$g_{i,j}^R(\mathbf{r}, \mathbf{r}', t) = \Theta(t) (g_{i,j}^>(\mathbf{r}, \mathbf{r}', t) - g_{i,j}^<(\mathbf{r}, \mathbf{r}', t)), \quad (2.12a)$$

$$g_{i,j}^A(\mathbf{r}, \mathbf{r}', t) = -\Theta(-t) (g_{i,j}^>(\mathbf{r}, \mathbf{r}', t) - g_{i,j}^<(\mathbf{r}, \mathbf{r}', t)), \quad (2.12b)$$

and

$$g_{i,j}^R(\mathbf{r}, \mathbf{r}', t) - g_{i,j}^A(\mathbf{r}, \mathbf{r}', t) = g_{i,j}^>(\mathbf{r}, \mathbf{r}', t) - g_{i,j}^<(\mathbf{r}, \mathbf{r}', t). \quad (2.13)$$

By calculating the spectral representation of these Green's functions, another relation between them can be established. The greater Green's function is given through

$$g_{i,j}^>(\mathbf{r}, \mathbf{r}', t) = -\frac{i}{Z} \text{Tr} \left( e^{iHt} (\Psi_{\mathbf{r}})_i e^{-iHt} (\Psi_{\mathbf{r}'}^\dagger)_j e^{-\beta H} \right) \quad (2.14a)$$

$$= -\frac{i}{Z} \sum_{m,n} \langle m | (\Psi_{\mathbf{r}})_i | n \rangle \langle n | (\Psi_{\mathbf{r}'}^\dagger)_j | m \rangle e^{i(E_m - E_n)t} e^{-\beta E_m}, \quad (2.14b)$$

which renders

$$g_{i,j}^>(\mathbf{r}, \mathbf{r}', \omega) = \frac{2\pi i}{Z} \sum_{m,n} \langle m | (\Psi_{\mathbf{r}})_i | n \rangle \langle n | (\Psi_{\mathbf{r}'}^\dagger)_j | m \rangle e^{-\beta E_m} \delta(E_m - E_n + \omega) \quad (2.14c)$$

when it is expressed in dependence of  $\omega$  with the eigenstates  $|n\rangle$  and eigenvalues  $E_m$  of the Hamiltonian. Analogously, the lesser Green's function reads

$$g_{i,j}^<(\mathbf{r}, \mathbf{r}', t) = \frac{i}{Z} \text{Tr} \left( (\Psi_{\mathbf{r}'}^\dagger)_j e^{iHt} (\Psi_{\mathbf{r}})_i e^{-iHt} e^{-\beta H} \right) \quad (2.15a)$$

$$= \frac{i}{Z} \sum_{m,n} \langle n | (\Psi_{\mathbf{r}'}^\dagger)_j | m \rangle \langle m | (\Psi_{\mathbf{r}})_i | n \rangle e^{i(E_m - E_n)t} e^{-\beta E_n}, \quad (2.15b)$$

resulting in

$$g_{i,j}^<(\mathbf{r}, \mathbf{r}', \omega) = \frac{2\pi i}{Z} \sum_{m,n} \langle m | (\Psi_{\mathbf{r}})_i | n \rangle \langle n | (\Psi_{\mathbf{r}'})_j^\dagger | m \rangle e^{-\beta E_n} \delta(E_m - E_n + \omega) . \quad (2.15c)$$

From the Dirac  $\delta$ -distribution follows  $E_n = E_m + \omega$ , resulting in the relation

$$g_{i,j}^<(\mathbf{r}, \mathbf{r}', \omega) = -g_{i,j}^>(\mathbf{r}, \mathbf{r}', \omega) e^{-\beta\omega} . \quad (2.16)$$

Since Eq. (2.13) can be Fourier transformed to frequency space, the relation

$$g_{i,j}^>(\mathbf{r}, \mathbf{r}', \omega) - g_{i,j}^<(\mathbf{r}, \mathbf{r}', \omega) = g_{i,j}^R(\mathbf{r}, \mathbf{r}', \omega) - g_{i,j}^A(\mathbf{r}, \mathbf{r}', \omega) \quad (2.17)$$

follows, which then yields

$$-g_{i,j}^<(\mathbf{r}, \mathbf{r}', \omega) (1 + e^{\beta\omega}) = g_{i,j}^R(\mathbf{r}, \mathbf{r}', \omega) - g_{i,j}^A(\mathbf{r}, \mathbf{r}', \omega) \quad (2.18)$$

and can be rearranged to

$$g_{i,j}^<(\mathbf{r}, \mathbf{r}', \omega) = -n_{\text{F}}(\omega) (g_{i,j}^R(\mathbf{r}, \mathbf{r}', \omega) - g_{i,j}^A(\mathbf{r}, \mathbf{r}', \omega)) \quad (2.19)$$

with Eq. (2.16) and the Fermi-Dirac distribution function  $n_{\text{F}}(\omega)$ .

As previously explained in section 2.4, the retarded and advanced Green's functions can be expressed through the eigenfunctions  $u_{k,i}(\mathbf{r})$  and eigenenergies  $E_k$  of the diagonalized Hamiltonian as

$$g_{i,j}^<(\mathbf{r}, \mathbf{r}', \omega) = -n_{\text{F}}(\omega) \sum_k u_{k,i}(\mathbf{r}) u_{k,j}^*(\mathbf{r}') \left( \frac{1}{\omega + i\delta - E_k} - \frac{1}{\omega - i\delta - E_k} \right) \quad (2.20a)$$

$$= -n_{\text{F}}(\omega) \sum_k u_{k,i}(\mathbf{r}) u_{k,j}^*(\mathbf{r}') \frac{-2i\delta}{(\omega - E_k)^2 + \delta^2} \quad (2.20b)$$

$$= 2\pi i n_{\text{F}}(\omega) \sum_k u_{k,i}(\mathbf{r}) u_{k,j}^*(\mathbf{r}') \delta(\omega - E_k) . \quad (2.20c)$$

Substituting this into the formula (2.10) yields

$$I_{\mathbf{r},\mathbf{r}'}^i = -\frac{2e}{\hbar} \int \frac{d\omega}{2\pi} \text{Re} \left[ t_{\mathbf{r},\mathbf{r}'}^{ii} 2\pi i n_{\text{F}}(\omega) \sum_k u_{k,i}(\mathbf{r}) u_{k,i}^*(\mathbf{r}') \delta(\omega - E_k) \right] \quad (2.21a)$$

$$= \frac{2e}{\hbar} \int d\omega \text{Im} \left[ t_{\mathbf{r},\mathbf{r}'}^{ii} n_{\text{F}}(\omega) \sum_k u_{k,i}(\mathbf{r}) u_{k,i}^*(\mathbf{r}') \delta(\omega - E_k) \right] \quad (2.21b)$$

$$= \frac{2e}{\hbar} t_{\mathbf{r},\mathbf{r}'}^{ii} \sum_k n_{\text{F}}(E_k) u_{k,i}(\mathbf{r}) u_{k,i}^*(\mathbf{r}') , \quad (2.21c)$$

where we used  $\text{Re}(iz) = -\text{Im}(z)$ . Here, it can be seen that the total current for one spin orientation is calculated from a sum over all the contributions from the different eigenmodes of the Hamiltonian. This also allows to compute the contribution to the total current carried by specific eigenmodes. Furthermore, it should be noted that the energy eigenvalues come in pairs  $\pm E_k$ , so that the summation over all energy eigenvalues in Eq. (2.21) combined with the Fermi-Dirac distribution  $n_{\text{F}}(E_k)$  is equivalent to a sum of all negative eigenvalues at a temperature of  $T = 0$ .

Now we employ that in our model the hopping parameter is only non-vanishing between neighboring sites  $t_{\mathbf{r},\mathbf{r}+\boldsymbol{\delta}}^i = -t$  and arrive at the final result for the current between these sites

$$I_{\mathbf{r},\mathbf{r}+\boldsymbol{\delta}}^i = \frac{2e}{\hbar}(-t) \sum_k n_{\text{F}}(E_k) u_{k,i}(\mathbf{r}) u_{k,i}^*(\mathbf{r} + \boldsymbol{\delta}). \quad (2.22)$$

In comparison, the current between all other sites vanishes due to the non-existent hopping parameter between those sites. The total supercurrent between neighboring sites is then given by the sum of the electronic components with  $i = 0 = \uparrow$  and  $i = 1 = \downarrow$

$$I_{\mathbf{r},\mathbf{r}+\boldsymbol{\delta}} = I_{\mathbf{r},\mathbf{r}+\boldsymbol{\delta}}^{\uparrow} + I_{\mathbf{r},\mathbf{r}+\boldsymbol{\delta}}^{\downarrow}. \quad (2.23)$$

For a graphic representation of the current's flow through one site, the sum over all currents to neighboring sites multiplied by the normalized vector  $\boldsymbol{\delta}$  connecting the two sites is taken, yielding the vectorized current at one site  $\mathbf{r}$  as

$$\mathbf{I}_{\mathbf{r}} = \sum_{\boldsymbol{\delta}} I_{\mathbf{r},\mathbf{r}+\boldsymbol{\delta}} \cdot \frac{\boldsymbol{\delta}}{|\boldsymbol{\delta}|}. \quad (2.24)$$

Physically, it can be seen that the supercurrent calculated from Eq. (2.21) is related to the correlations between different sites. As in the investigated model, only nearest-neighboring sites interact through the hopping parameter, the calculated supercurrent gives an account of the correlations between two neighboring sites, arising from all eigenmodes of the Hamiltonian with a negative energy for a temperature of  $T = 0$ .

## 3 The Magnetic Triple-Q Structure

### 3.1 Spin Structure

The triple-Q state or 3Q structure has been predicted theoretically [25] and also recently been discovered experimentally [26]. It is modelled on a triangular lattice, given through the lattice vectors  $\mathbf{a}_1 = a_0(1, 0)^T$  and  $\mathbf{a}_2 = a_0\left(\frac{1}{2}, \frac{\sqrt{3}}{2}\right)^T$  with the lattice constant  $a_0$ . We begin by considering a model in which the magnetic adatoms are placed directly above the atoms of the superconducting substrate, as demonstrated in Fig. 3.1. In the following, this model will be referred to as model I.

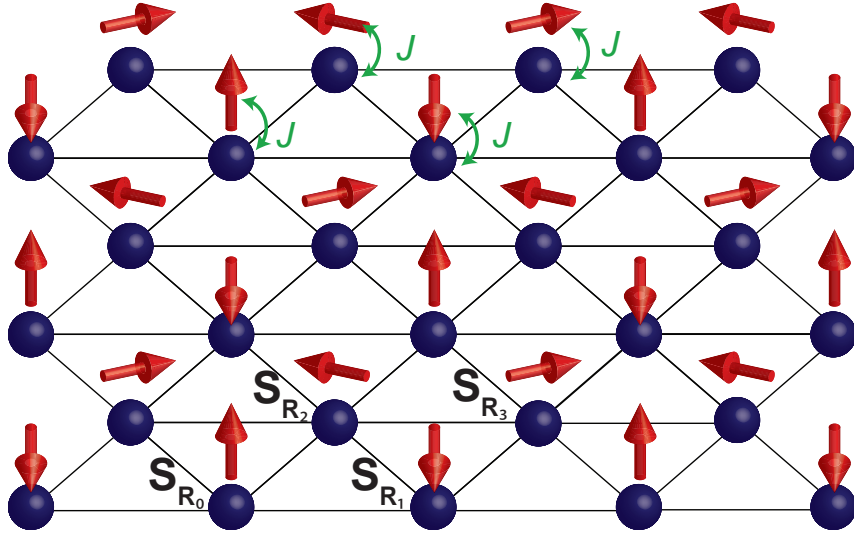


**Fig. 3.1:** Spatial plot of the 3Q ordered spin structure on the triangular lattice [55].

Here, each spin's orientation is chosen out of four possible orientations

$$\mathbf{S}_{\mathbf{R}_i} = S \begin{cases} (0, 0, 1)^T, & \mathbf{R}_0 = \mathbf{0} \\ (0, -\sqrt{8}/3, -1/3)^T, & \mathbf{R}_1 = \mathbf{a}_1 \\ (-\sqrt{6}/3, \sqrt{2}/3, -1/3)^T, & \mathbf{R}_2 = \mathbf{a}_2 \\ (\sqrt{6}/3, \sqrt{2}/3, -1/3)^T, & \mathbf{R}_3 = \mathbf{a}_1 + \mathbf{a}_2 \end{cases}, \quad (3.1)$$

which are all assumed within the lattice's unit cell consisting of four atoms. These orientations are determined by the vectors pointing outwards from the center of a tetrahedron towards its corners.

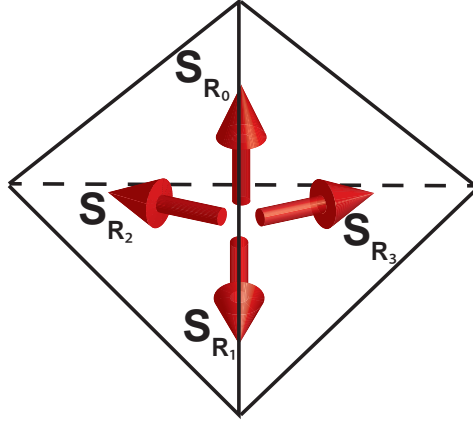


**Fig. 3.2:** The four spin orientations from the  $2 \times 2$  unit cell of the magnetic 3Q structure arranged in a tetrahedron [56].

### 3.1.1 Effective Rashba Spin-Orbit Coupling

An important fact to notice is that the Hamiltonian from Eq. (2.1c) does not contain an interaction term referring to an intrinsic Rashba spin-orbit coupling. An effective form of this interaction is induced by the chosen non-collinear spin structure, which can be seen by performing a local gauge transformation on the spin's orientation to align them ferromagnetically.

As MSH systems that contain a ferromagnetic order and an intrinsic Rashba spin-orbit coupling have already been proven to exhibit topological superconductivity [14–16], this kind of transformation allows for a test whether a chosen spin structure realizes this scenario. In order to conduct this transformation, the rotated fermionic operators  $d_{\mathbf{r},\uparrow/\downarrow}^{(\dagger)}$  are defined as

$$\begin{pmatrix} c_{\mathbf{r}\uparrow} \\ c_{\mathbf{r}\downarrow} \end{pmatrix} = \hat{U}_{\mathbf{r}} \begin{pmatrix} d_{\mathbf{r}\uparrow} \\ d_{\mathbf{r}\downarrow} \end{pmatrix} \quad (3.2)$$

with the transformation matrix  $\hat{U}_{\mathbf{r}}$ . The transformation rotating all spins to be aligned in  $z$ -direction [24] is given by

$$\hat{U}_{\mathbf{r}} = e^{i\frac{\theta_{\mathbf{r}}}{2}\sigma \cdot \hat{n}_{\mathbf{r}}} \quad (3.3)$$

with the angle of rotation

$$\cos(\theta_{\mathbf{r}}) = \frac{S_{\mathbf{r}}}{|S_{\mathbf{r}}|} \cdot \hat{z} \quad (3.4)$$

and the rotation axis

$$\hat{n}_{\mathbf{r}} = \frac{S_{\mathbf{r}} \times \hat{z}}{|S_{\mathbf{r}} \times \hat{z}|}. \quad (3.5)$$

For the four different spins in the 3Q state from Eq. (3.1), the four different matrices  $\hat{U}_{\mathbf{r}_i}$  for the local gauge transformation are given through

$$\hat{U}_{\mathbf{r}_0} = \mathbf{1}_{2 \times 2}, \quad (3.6a)$$

$$\hat{U}_{\mathbf{r}_1} = \begin{pmatrix} \frac{1}{\sqrt{3}} & -i\sqrt{\frac{2}{3}} \\ -i\sqrt{\frac{2}{3}} & \frac{1}{\sqrt{3}} \end{pmatrix}, \quad (3.6b)$$

$$\hat{U}_{\mathbf{r}_2} = \begin{pmatrix} \frac{1}{\sqrt{3}} & \frac{1}{\sqrt{2}} + i\frac{1}{\sqrt{6}} \\ -\frac{1}{\sqrt{2}} + i\frac{1}{\sqrt{6}} & \frac{1}{\sqrt{3}} \end{pmatrix} \quad (3.6c)$$

and

$$\hat{U}_{\mathbf{r}_3} = \begin{pmatrix} \frac{1}{\sqrt{3}} & -\frac{1}{\sqrt{2}} + i\frac{1}{\sqrt{6}} \\ \frac{1}{\sqrt{2}} + i\frac{1}{\sqrt{6}} & \frac{1}{\sqrt{3}} \end{pmatrix}. \quad (3.6d)$$

The Hamiltonian, written in the basis of the creation operators  $d_{\mathbf{r},\uparrow/\downarrow}^\dagger$ , then takes the form

$$H = \sum_{\mathbf{r},\mathbf{r}',\alpha,\beta} (-t_{\mathbf{r},\mathbf{r}'} \hat{U}_{\mathbf{r}}^\dagger \hat{U}_{\mathbf{r}'})_{\alpha\beta} d_{\mathbf{r}\alpha}^\dagger d_{\mathbf{r}\beta} + \Delta \sum_{\mathbf{r}} (d_{\mathbf{r}\uparrow}^\dagger d_{\mathbf{r}\downarrow}^\dagger + \text{h.c.}) + \sum_{\mathbf{r},\alpha} (JS\sigma_{\alpha\alpha}^z - \mu) d_{\mathbf{r}\alpha}^\dagger d_{\mathbf{r}\alpha}. \quad (3.7)$$

For the terms in the Hamiltonian expressing the chemical potential as well as the s-wave superconductivity, the Hamiltonian is already proportional to the identity matrix with respect to different spin orientations prior to the transformation. Therefore, applying the unitary transformation to the fermionic operators leaves these terms unchanged.

The hopping term in the transformed Hamiltonian is now a matrix

$$-\hat{t}_{ij} = -t_{\mathbf{r}_i,\mathbf{r}'_j} \cdot \hat{U}_{\mathbf{r}_i}^\dagger \cdot \hat{U}_{\mathbf{r}'_j} = \begin{pmatrix} -\tilde{t}_{\mathbf{r}_i,\mathbf{r}'_j} & -\alpha_{\mathbf{r}_i,\mathbf{r}'_j}^* \\ \alpha_{\mathbf{r}_i,\mathbf{r}'_j} & -\tilde{t}_{\mathbf{r}_i,\mathbf{r}'_j}^* \end{pmatrix}, \quad (3.8)$$

in which the diagonal terms represent the effective hopping, whereas the off-diagonal terms show the intrinsic Rashba spin-orbit coupling induced by the spin structure. On the triangular lattice with 3Q-ordered spins, six different unique bonds between the different spins at nearest-neighboring sites exist, as depicted in Fig. 3.3. Here, for each pair of spins  $\mathbf{S}_{\mathbf{R}_i}$  and  $\mathbf{S}_{\mathbf{R}_j}$  with  $i \neq j$ , only one direction of the bond  $\mathbf{r}_{ij}$  connecting them is shown. For reasons of visibility, only the positions of the sites, where the different spins are located, are depicted there.

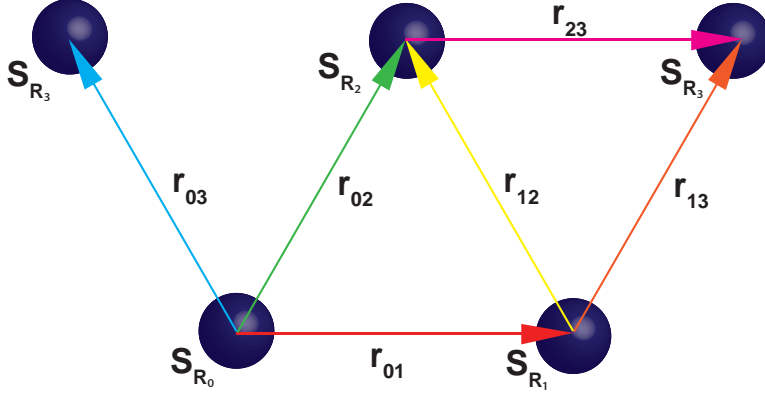


**Fig. 3.3:** Schematic plot of the six different unique bonds  $\mathbf{r}_{ij}$  between spins of different orientation  $\mathbf{S}_{\mathbf{R}_i}$  and  $\mathbf{S}_{\mathbf{R}_j}$  with  $i \neq j$  at nearest neighboring sites.

For these bonds, the induced couplings are calculated and the resulting matrices are given as

$$\hat{t}_{01} = t \begin{pmatrix} \frac{1}{\sqrt{3}} & -i\sqrt{\frac{2}{3}} \\ -i\sqrt{\frac{2}{3}} & \frac{1}{\sqrt{3}} \end{pmatrix}, \quad \hat{t}_{02} = t \begin{pmatrix} \frac{1}{\sqrt{3}} & \frac{1}{\sqrt{2}} + i\frac{1}{\sqrt{6}} \\ -\frac{1}{\sqrt{2}} + i\frac{1}{\sqrt{6}} & \frac{1}{\sqrt{3}} \end{pmatrix}, \quad (3.9a)$$

$$\hat{t}_{03} = t \begin{pmatrix} \frac{1}{\sqrt{3}} & -\frac{1}{\sqrt{2}} + i\frac{1}{\sqrt{6}} \\ \frac{1}{\sqrt{2}} + i\frac{1}{\sqrt{6}} & \frac{1}{\sqrt{3}} \end{pmatrix}, \quad \hat{t}_{12} = t \begin{pmatrix} -\frac{i}{\sqrt{3}} & \frac{1}{\sqrt{6}} + \frac{i}{\sqrt{2}} \\ -\frac{1}{\sqrt{6}} + \frac{i}{\sqrt{2}} & \frac{i}{\sqrt{3}} \end{pmatrix}, \quad (3.9b)$$

$$\hat{t}_{13} = t \begin{pmatrix} \frac{i}{\sqrt{3}} & -\frac{1}{\sqrt{6}} + \frac{i}{\sqrt{2}} \\ \frac{1}{\sqrt{6}} + \frac{i}{\sqrt{2}} & -\frac{i}{\sqrt{3}} \end{pmatrix}, \quad \text{and} \quad \hat{t}_{23} = t \begin{pmatrix} -\frac{i}{\sqrt{3}} & -\sqrt{\frac{2}{3}} \\ \sqrt{\frac{2}{3}} & \frac{i}{\sqrt{3}} \end{pmatrix}. \quad (3.9c)$$

Here, the hopping matrices of bonds of opposite direction are the respective hermitian

conjugates  $\hat{t}_{ij} = \hat{t}_{ji}^\dagger = t \cdot \hat{U}_{\mathbf{r}_i}^\dagger \cdot \hat{U}_{\mathbf{r}_j}$ . By taking into account the absolute value for all different bonds, it can be deduced that the magnitude of the effective Rashba spin-orbit coupling is uniform and has a value of  $\alpha = |\alpha_{\mathbf{r}_i, \mathbf{r}_j}| = \sqrt{\frac{2}{3}}t$ , whereas the phase of the induced coupling varies between the different unique bonds. The effective hopping has a reduced magnitude of  $\tilde{t} = \sqrt{\frac{1}{3}}t$  compared to its original value.

### 3.2 Band Structure

In order to calculate the band structure, the Hamiltonian from Eq. (2.1c) has to be transformed using crystal momenta  $\mathbf{k}$  from the reduced Brillouin zone (RBZ). The discrete Fourier transformation and its inverse achieving this aim is given through

$$c_{\mathbf{r}, \mathbf{R}_i} = \frac{1}{\sqrt{N_1 N_2}} \sum_{\mathbf{k} \in \text{RBZ}} c_{\mathbf{k}, \mathbf{R}_i} e^{i\mathbf{k} \cdot \mathbf{r}} \quad (3.10)$$

$$c_{\mathbf{k}, \mathbf{R}_i} = \frac{1}{\sqrt{N_1 N_2}} \sum_{\mathbf{r} \in A} c_{\mathbf{r}, \mathbf{R}_i} e^{-i\mathbf{k} \cdot \mathbf{r}}, \quad (3.11)$$

where the sum is taken over all the crystal momenta from the reduced Brillouin zone, which is spanned by the two reciprocal lattice vectors  $\mathbf{b}_1 = \frac{\pi}{a_0} \left(1, -\frac{1}{\sqrt{3}}\right)^\top$  and  $\mathbf{b}_2 = \frac{\pi}{a_0} \left(0, \frac{2}{\sqrt{3}}\right)^\top$ .

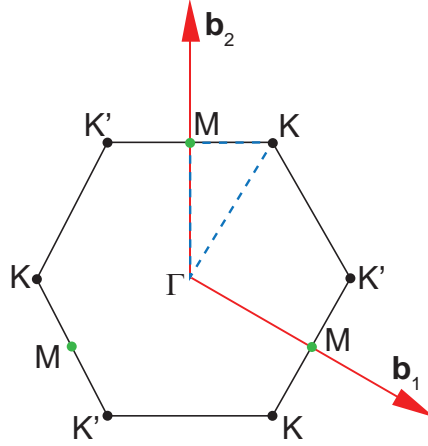


**Fig. 3.4:** Schematic plot of the reduced Brillouin zone for a triangular lattice with the reciprocal lattice vectors  $\mathbf{b}_1$  and  $\mathbf{b}_2$  and the high-symmetry points  $\Gamma$ , M, K and  $K'$  marked. The blue dashed line depicts the chosen path for the band structures calculated in Fig. 3.6.

The usage of the reduced Brillouin zone implies in this case that the transformed Hamiltonian is a  $16 \times 16$  matrix. This dimensionality results from the four atoms in the unit cell combined with the dimension of Nambu space, which is employed in order to include both spin orientations for both electronic and hole-like operators. The transformed Hamiltonian in  $\mathbf{k}$ -space reads

$$\mathcal{H} = \sum_{\mathbf{k} \in \text{RBZ}} c_{\mathbf{k}}^\dagger H(\mathbf{k}) c_{\mathbf{k}}. \quad (3.12)$$

Here, the matrix representation  $H(\mathbf{k})$  of the Hamiltonian acts on the combined vector of creation and annihilation operators, which is given through

$$c_{\mathbf{k}} = \begin{pmatrix} c_{\mathbf{k},\mathbf{r}_0} \\ c_{\mathbf{k},\mathbf{r}_1} \\ c_{\mathbf{k},\mathbf{r}_2} \\ c_{\mathbf{k},\mathbf{r}_3} \end{pmatrix} \quad (3.13)$$

where  $c_{\mathbf{k},\mathbf{r}_i}$  is combined of electronic and hole-like components for both spin orientations

$$c_{\mathbf{k},\mathbf{r}_i} = \begin{pmatrix} c_{\mathbf{k},\mathbf{r}_i,\uparrow} \\ c_{\mathbf{k},\mathbf{r}_i,\downarrow} \\ c_{\mathbf{k},\mathbf{r}_i,\downarrow}^\dagger \\ -c_{\mathbf{k},\mathbf{r}_i,\uparrow}^\dagger \end{pmatrix}. \quad (3.14)$$

Thereby, a spinor of 16 creation and annihilation operators is defined. The matrix representation  $H(\mathbf{k})$  of the Hamiltonian reads

$$H(\mathbf{k}) = \begin{pmatrix} -\mu\tau_z \otimes \sigma_0 + \Delta\tau_x \otimes \sigma_0 + J\tau_0 \otimes (\mathbf{S}_1 \cdot \boldsymbol{\sigma}) & -tc_{\mathbf{a}_1}\tau_z \otimes \sigma_0 & & & \\ & -tc_{\mathbf{a}_1}\tau_z \otimes \sigma_0 & -\mu\tau_z \otimes \sigma_0 + \Delta\tau_x \otimes \sigma_0 + J\tau_0 \otimes (\mathbf{S}_2 \cdot \boldsymbol{\sigma}) & \dots & \\ & -tc_{\mathbf{a}_2}\tau_z \otimes \sigma_0 & & -tc_{\mathbf{a}_2-\mathbf{a}_1}\tau_z \otimes \sigma_0 & \\ & -tc_{\mathbf{a}_2-\mathbf{a}_1}\tau_z \otimes \sigma_0 & & -tc_{\mathbf{a}_2}\tau_z \otimes \sigma_0 & \\ \dots & -tc_{\mathbf{a}_2}\tau_z \otimes \sigma_0 & & -tc_{\mathbf{a}_2-\mathbf{a}_1}\tau_z \otimes \sigma_0 & \\ \dots & -\mu\tau_z \otimes \sigma_0 + \Delta\tau_x \otimes \sigma_0 + J\tau_0 \otimes (\mathbf{S}_3 \cdot \boldsymbol{\sigma}) & & -tc_{\mathbf{a}_1}\tau_z \otimes \sigma_0 & \\ & -tc_{\mathbf{a}_1}\tau_z \otimes \sigma_0 & & -\mu\tau_z \otimes \sigma_0 + \Delta\tau_x \otimes \sigma_0 + J\tau_0 \otimes (\mathbf{S}_4 \cdot \boldsymbol{\sigma}) & \end{pmatrix}, \quad (3.15a)$$

where the abbreviations

$$c_{\mathbf{a}_1}(\mathbf{k}) = \cos(\mathbf{k} \cdot \mathbf{a}_1), \quad (3.15b)$$

$$c_{\mathbf{a}_2}(\mathbf{k}) = \cos(\mathbf{k} \cdot \mathbf{a}_2), \quad (3.15c)$$

$$c_{\mathbf{a}_2-\mathbf{a}_1}(\mathbf{k}) = \cos(\mathbf{k} \cdot (\mathbf{a}_2 - \mathbf{a}_1)) \quad (3.15d)$$

are employed. In the matrix  $H(\mathbf{k})$ , we left out the dependence of  $c_{\mathbf{a}_2}$ ,  $c_{\mathbf{a}_1}$  and  $c_{\mathbf{a}_2-\mathbf{a}_1}$  on  $\mathbf{k}$  for the sake of brevity. The matrices  $\tau_x$ ,  $\tau_y$  and  $\tau_z$  have the same matrix representation as the Pauli matrices from Eq. (2.2), but act in Nambu space and are therefore applied to the combined vector of electronic and hole-like creation operators of the same spin  $(c_{\mathbf{r},\sigma}^\dagger, c_{\mathbf{r},\sigma})^\top$ .

### 3.2.1 Symmetry Transformation

For the diagonalization of the Hamiltonian for the 3Q structure, previously introduced in Eq. (3.15d), the symmetry within the spin structure provides a way to block-diagonalize the matrix representation before employing a numeric diagonalization routine. This symmetry originates from the fact that the different spin orientations can be transformed into one another in pairs. In Fig. 3.2, the spin orientations are shown as the four orientations from the center of a tetrahedron to its corners. Here, it can be seen that the spin orientations belong to the tetrahedron group. Thereby, if the spin structure is rotated by  $\pi$  around one of the axes determined by

$$\mathbf{n} = \frac{\mathbf{S}_{\mathbf{R}_i} + \mathbf{S}_{\mathbf{R}_j}}{|\mathbf{S}_{\mathbf{R}_i} + \mathbf{S}_{\mathbf{R}_j}|} \text{ with } i \neq j, \quad (3.16)$$

the spins  $\mathbf{S}_{\mathbf{R}_i}$  and  $\mathbf{S}_{\mathbf{R}_j}$  are rotated into one another as well as the other pair of spins. Combined with a translation on the triangular lattice, e.g. a translation by  $\mathbf{a}_1$  when  $\mathbf{S}_{\mathbf{R}_0}$  and  $\mathbf{S}_{\mathbf{R}_1}$  are rotated into one another, the entire spin structure is left invariant on the triangular lattice.

For the 3Q structure, a translation by  $\mathbf{a}_1$  is equivalent to an exchange of the sites, where the spins  $\mathbf{S}_{\mathbf{r}_0}$  and  $\mathbf{S}_{\mathbf{r}_1}$  are located. As a matrix, the operation of translation can thus be expressed as

$$\hat{T} = \begin{pmatrix} 0 & 1 & 0 & 0 \\ 1 & 0 & 0 & 0 \\ 0 & 0 & 0 & 1 \\ 0 & 0 & 1 & 0 \end{pmatrix} \otimes \mathbb{1}_{4 \times 4} \quad (3.17)$$

and the rotation of the spins through

$$\hat{R} = e^{i\frac{\pi}{2}\mathbb{1}_{4 \times 4} \otimes (\mathbf{n} \cdot \boldsymbol{\sigma})} = i\mathbb{1}_{4 \times 4} \otimes (\mathbf{n} \cdot \boldsymbol{\sigma}) \quad (3.18a)$$

$$= \mathbb{1}_{4 \times 4} \otimes \begin{pmatrix} \frac{i}{\sqrt{3}} & -\sqrt{\frac{2}{3}} & 0 & 0 \\ \sqrt{\frac{2}{3}} & -\frac{i}{\sqrt{3}} & 0 & 0 \\ 0 & 0 & \frac{i}{\sqrt{3}} & -\sqrt{\frac{2}{3}} \\ 0 & 0 & \sqrt{\frac{2}{3}} & -\frac{i}{\sqrt{3}} \end{pmatrix}. \quad (3.18b)$$

These two matrices are split into the Kronecker product of two  $4 \times 4$  matrices, of which the first matrix acts on the four fermionic operators with the same index in Nambu space at the four different spatial sites in the unit cell and the second matrix acts on the four electronic and hole-like fermionic operators of both spin orientations at one of these sites, as given in Eq. (3.14). The combined matrix  $\hat{S} = \hat{T} \cdot \hat{R}$  then leaves the Fourier transformed Hamiltonian invariant as

$$\hat{H}(\mathbf{k}) = \hat{S}^\dagger \hat{H}(\mathbf{k}) \hat{S}. \quad (3.19)$$

Thereby, a transformation  $\hat{U}_{\hat{S}}$  which diagonalizes  $\hat{S}$  through the operation  $\hat{U}_{\hat{S}}^\dagger \cdot \hat{S} \cdot \hat{U}_{\hat{S}}$  will also block-diagonalize  $H(k)$ . For reasons of simplicity, the task of finding the transformation  $\hat{U}_{\hat{S}}$  can be split into diagonalizing  $\hat{T}$  as well as  $\hat{R}$  and then multiplying the two resulting transformations  $\hat{U}_{\hat{T}}$  and  $\hat{U}_{\hat{R}}$ . These two matrices are composed of the respective sets of eigenvectors as

$$\hat{U}_{\hat{T}} = \frac{1}{\sqrt{2}} \begin{pmatrix} 1 & -1 & 0 & 0 \\ 1 & 1 & 0 & 0 \\ 0 & 0 & 1 & -1 \\ 0 & 0 & 1 & 1 \end{pmatrix} \otimes \mathbb{1}_{4 \times 4} \quad (3.20)$$

and

$$\hat{U}_{\hat{R}} = \mathbb{1}_{4 \times 4} \otimes \begin{pmatrix} \sqrt{\frac{1}{6}(3 + \sqrt{3})} & -\frac{i}{\sqrt{3 + \sqrt{3}}} & 0 & 0 \\ -\frac{i}{\sqrt{3 + \sqrt{3}}} & \sqrt{\frac{1}{6}(3 + \sqrt{3})} & 0 & 0 \\ 0 & 0 & \sqrt{\frac{1}{6}(3 + \sqrt{3})} & -\frac{i}{\sqrt{3 + \sqrt{3}}} \\ 0 & 0 & -\frac{i}{\sqrt{3 + \sqrt{3}}} & \sqrt{\frac{1}{6}(3 + \sqrt{3})} \end{pmatrix}. \quad (3.21)$$

The unitary transformation, given through

$$\hat{U}_{\hat{S}} = \hat{U}_{\hat{T}} \cdot \hat{U}_{\hat{R}} \cdot \hat{P} \quad (3.22)$$

with

$$\hat{P} = \begin{pmatrix} 1 & 0 & 0 & 0 & 0 & 0 & 0 & 0 & 0 & 0 & 0 & 0 & 0 & 0 & 0 \\ 0 & 0 & 0 & 0 & 0 & 0 & 0 & 0 & 1 & 0 & 0 & 0 & 0 & 0 & 0 \\ 0 & 1 & 0 & 0 & 0 & 0 & 0 & 0 & 0 & 0 & 0 & 0 & 0 & 0 & 0 \\ 0 & 0 & 0 & 0 & 0 & 0 & 0 & 0 & 0 & 1 & 0 & 0 & 0 & 0 & 0 \\ 0 & 0 & 0 & 0 & 0 & 0 & 0 & 0 & 0 & 0 & 1 & 0 & 0 & 0 & 0 \\ 0 & 0 & 1 & 0 & 0 & 0 & 0 & 0 & 0 & 0 & 0 & 0 & 0 & 0 & 0 \\ 0 & 0 & 0 & 0 & 0 & 0 & 0 & 0 & 0 & 0 & 0 & 1 & 0 & 0 & 0 \\ 0 & 0 & 0 & 1 & 0 & 0 & 0 & 0 & 0 & 0 & 0 & 0 & 0 & 0 & 0 \\ 0 & 0 & 0 & 0 & 1 & 0 & 0 & 0 & 0 & 0 & 0 & 0 & 0 & 0 & 0 \\ 0 & 0 & 0 & 0 & 0 & 0 & 0 & 0 & 0 & 0 & 0 & 1 & 0 & 0 & 0 \\ 0 & 0 & 0 & 0 & 0 & 1 & 0 & 0 & 0 & 0 & 0 & 0 & 0 & 0 & 0 \\ 0 & 0 & 0 & 0 & 0 & 0 & 0 & 0 & 0 & 0 & 0 & 0 & 1 & 0 & 0 \\ 0 & 0 & 0 & 0 & 0 & 0 & 0 & 0 & 0 & 0 & 0 & 0 & 0 & 1 & 0 \\ 0 & 0 & 0 & 0 & 0 & 0 & 1 & 0 & 0 & 0 & 0 & 0 & 0 & 0 & 0 \\ 0 & 0 & 0 & 0 & 0 & 0 & 0 & 0 & 0 & 0 & 0 & 0 & 0 & 0 & 1 \\ 0 & 0 & 0 & 0 & 0 & 0 & 0 & 1 & 0 & 0 & 0 & 0 & 0 & 0 & 0 \end{pmatrix}, \quad (3.23)$$

then not only diagonalizes  $\hat{S}$ , but also sorts its eigenvalues  $\pm i$  by the sign of their imaginary parts, which is achieved through  $\hat{P}$ . Using this transformation, the matrix representation of the Hamiltonian can then be block-diagonalized into two  $8 \times 8$ -blocks, resulting in the transformed matrix

$$\hat{U}_{\hat{S}}^\dagger \hat{H}(\mathbf{k}) \hat{U}_{\hat{S}} = \begin{pmatrix} \hat{H}'(\mathbf{k}) & 0 \\ 0 & (i \mathbb{1}_{2 \times 2} \otimes \tau_z \otimes \sigma_y) \cdot \hat{H}'(\mathbf{k})^* \cdot (i \mathbb{1}_{2 \times 2} \otimes \tau_z \otimes \sigma_y) \end{pmatrix}, \quad (3.24)$$

where the first  $8 \times 8$  block is given through

$$\hat{H}'(\mathbf{k}) = \begin{pmatrix} \hat{A} & \hat{B} \\ \hat{B} & \hat{C} \end{pmatrix}, \quad (3.25)$$

with

$$\hat{A} = \begin{pmatrix} \frac{J}{\sqrt{3}} - 2tc_{a_0,0} - \mu & \Delta & i\sqrt{\frac{2}{3}}J & 0 \\ \Delta & \frac{J}{\sqrt{3}} + 2tc_{a_0,0} + \mu & 0 & i\sqrt{\frac{2}{3}}J \\ -i\sqrt{\frac{2}{3}}J & 0 & -\frac{J}{\sqrt{3}} + 2tc_{a_0,0} - \mu & \Delta \\ 0 & -i\sqrt{\frac{2}{3}}J & \Delta & -\frac{J}{\sqrt{3}} - 2tc_{a_0,0} + \mu \end{pmatrix}, \quad (3.26)$$

$$\hat{B} = \begin{pmatrix} -4tc_{\frac{1}{2}a_0, \frac{\sqrt{3}}{2}a_0}(k_y) & 0 & 0 & 0 \\ 0 & 4tc_{\frac{1}{2}a_0, \frac{\sqrt{3}}{2}a_0}(k_y) & 0 & 0 \\ 0 & 0 & 4ts_{\frac{1}{2}a_0, \frac{\sqrt{3}}{2}a_0} & 0 \\ 0 & 0 & 0 & -4ts_{\frac{1}{2}a_0, \frac{\sqrt{3}}{2}a_0} \end{pmatrix} \quad (3.27)$$

and

$$\hat{C} = \begin{pmatrix} -\frac{J}{\sqrt{3}} - 2tc_{a_0,0} - \mu & \Delta & \sqrt{\frac{2}{3}}J & 0 \\ \Delta & -\frac{J}{\sqrt{3}} + 2tc_{a_0,0} + \mu & 0 & \sqrt{\frac{2}{3}}J \\ \sqrt{\frac{2}{3}}J & 0 & \frac{J}{\sqrt{3}} + 2tc_{a_0,0} - \mu & \Delta \\ 0 & \sqrt{\frac{2}{3}}J & \Delta & \frac{J}{\sqrt{3}} - 2tc_{a_0,0} + \mu \end{pmatrix}. \quad (3.28)$$

Here, the abbreviations

$$c_{\frac{1}{2}a_0, \frac{\sqrt{3}}{2}a_0}(k_x, k_y) = \cos\left(\frac{1}{2}k_x a_0\right) \cos\left(\frac{\sqrt{3}}{2}k_y a_0\right), \quad (3.29a)$$

$$c_{a_0,0}(k_x, k_y) = \cos(k_x a_0), \quad (3.29b)$$

and

$$s_{\frac{1}{2}a_0, \frac{\sqrt{3}}{2}a_0}(k_x, k_y) = \sin\left(\frac{1}{2}k_x a_0\right) \sin\left(\frac{\sqrt{3}}{2}k_y a_0\right) \quad (3.29c)$$

were introduced. Due to the fact that the two blocks of the Hamiltonian have the same eigenvalues independent of the investigated crystal momentum, all eigenvalues are doubly degenerate, which results in doubly degenerate bands.

### 3.3 Topological Phase Diagram

Using the pre-diagonalized matrix representation of the Hamiltonian in Eq. (3.28), the Chern number can be calculated. In order to compute the Chern number

numerically, the reduced Brillouin zone from the Fourier transformation has to be discretized using a grid of crystal momenta. This grid  $\hat{k}$  of size  $n_k \times n_k$  was chosen as

$$\mathbf{k}_{i,j} = \frac{i}{n_k} \mathbf{b}_1 + \frac{j}{n_k} \mathbf{b}_2 \quad \text{with } i \in \{0, 1, \dots, n_k - 1\}, j \in \{0, 1, \dots, n_k - 1\}, \quad (3.30)$$

with  $n_k \in \mathbb{N}$  determining the fineness of the grid. Here,  $n_k = 1000$  was chosen. Next, the Hamiltonian was diagonalized numerically for each of these points in the reduced Brillouin zone yielding the eigenenergies  $E_n(\mathbf{k}_{i,j})$  and eigenstates  $|u_n(\mathbf{k}_{i,j})\rangle$ , from which the smallest positive energy eigenvalue was determined and the projection operator was calculated as

$$P(\mathbf{k}_{i,j}) = \sum_{E_n(\mathbf{k}_{i,j}) < 0} |u_n(\mathbf{k}_{i,j})\rangle \langle u_n(\mathbf{k}_{i,j})|. \quad (3.31)$$

Afterwards, the integrand from Eq. (2.4) is calculated for each of these discretized values of the crystal momentum. Therein, the partial derivatives in direction of  $k_1$  and  $k_2$  are approximated using the central finite differences method [57–59]. Here, the partial derivative by  $k_1$  is computed to eigh-order accuracy by

$$\begin{aligned} \partial_{k_1} P(\mathbf{k}_{i,j}) &= \frac{1}{280} P(\mathbf{k}_{(i-4)\%n_k,j}) - \frac{4}{105} P(\mathbf{k}_{(i-3)\%n_k,j}) + \frac{1}{5} P(\mathbf{k}_{(i-2)\%n_k,j}) \\ &\quad - \frac{1}{5} P(\mathbf{k}_{(i-1)\%n_k,j}) + \frac{1}{5} P(\mathbf{k}_{(i+1)\%n_k,j}) - \frac{1}{5} P(\mathbf{k}_{(i+2)\%n_k,j}) \\ &\quad + \frac{4}{105} P(\mathbf{k}_{(i+3)\%n_k,j}) - \frac{1}{280} P(\mathbf{k}_{(i+4)\%n_k,j}) + \mathcal{O}\left(\left(\frac{2\pi}{n_k}\right)^8\right) \end{aligned} \quad (3.32)$$

and the partial derivative by  $k_2$  analogously, where the periodicity of  $k_1$  is taken into account by employing the modulus operation. It is important to note here that because the Chern number is calculated for a triangular lattice, it is not efficient to calculate the derivatives with respect to  $k_x$  and  $k_y$ . Instead, it is calculated in direction of  $k_1$  and  $k_2$ , which point in the direction of the reciprocal lattice vectors  $\mathbf{b}_1$  and  $\mathbf{b}_2$ . Nevertheless, the result for the two procedures is the same. Afterwards, the computed derivatives are placed in Eq. (2.4), where the integral is replaced by a sum over all contributions from each  $\mathbf{k}_{i,j}$  for the discretized Brillouin zone.

The result for the Chern number is shown in Fig. 3.5 (a), where it was calculated for  $\mu \in [-5.0t, 5.0t]$ ,  $JS \in [0.0t, 3.0t]$  and  $\Delta = 0.4t$ . The value of the superconducting order parameter was chosen much larger than the values occurring in realistic scenarios, because the computation of the Chern number takes much longer for very small values of  $\Delta$ . Instead of discretizing the parameter space into equidistant points, the Chern number was calculated for singular parameter sets  $(\mu, \Delta, JS)$  by employing

a learner from the Python package Adaptive [60]. Therein, the Chern number is sampled in the chosen parameter space defined by the intervals for  $\mu$  and  $JS$ . In each sampling step, the Chern number is then calculated at a set of parameters, in whose surrounding region the loss of the learner is still high. Thereby, the phase transitions between regions of different Chern numbers are sampled better. In the phase diagram, it can be seen that the doubly-degenerate bands result in the occurrence of solely even-valued Chern numbers.

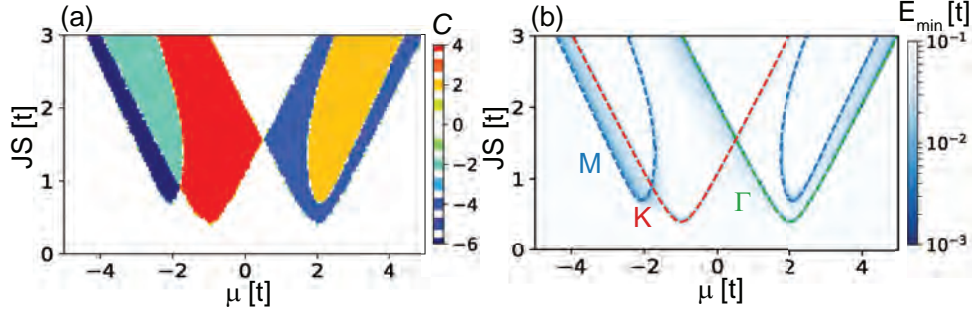


**Fig. 3.5:** (a) Phase diagram for an MSH structure with a 3Q-ordered magnetic layer, (b) lowest positive energy eigenvalue for all crystal momenta in the reduced Brillouin zone of the Hamiltonian with the 3Q-ordered spin structure.

Fig. 3.5 (b) depicts the lowest energy eigenvalue in the entire Brillouin zone. Next, by analyzing the band structure at the high symmetry points of the reduced Brillouin zone displayed in Fig. 3.4, it can be seen that the gap closings visible in Fig. 3.5 (b) occur at the high symmetry points  $\Gamma$ ,  $M$  as well as  $(K, K')$ .

By calculating the dispersion at these points, the analytic expressions for the gap closings can be calculated. At  $\Gamma$  as well as  $K$  and  $K'$ , this relation is quadratic, resulting in the two parabolically shaped branches in Fig. 3.5 (b). The gap closing is determined by

$$J^2 - \Delta^2 = (\mu - \mu_0)^2, \quad (3.33)$$

where  $\mu_0 = 2t$  at  $\Gamma$  and  $\mu_0 = -t$  at  $(K, K')$ .

These relations are found by an analytic diagonalization of the Hamiltonian at these high symmetry points in Mathematica [61]. At the points  $K$  and  $K'$ , the gap closings are exactly the same, for which the band structure is depicted in Fig. 3.6 (c) for the set of parameters  $(\mu, \Delta, JS) = (-1.0t, 0.4t, 0.4t)$ . For the three band structures shown here, the Hamiltonian was diagonalized for each of 700 equidistant points along a line in the Brillouin zone. This line starts at  $\Gamma$ , proceeds to the point  $M$  and then  $K$  and returns to  $\Gamma$ , as marked by the dashed blue line in Fig. 3.4.

For the gap closing at  $K$ , a Dirac cone emerges in the band structure. Thereby, performing a Taylor expansion at  $K$  at a specific set of parameters, for which the

gap closes at K, yields a linear expression in  $\mathbf{k}$ . Combining this linearity with the fact that the gap closes both at K and K' and the double degeneracy of the bands, gives a multiplicity of 4 for this gap closing and thereby explains a change in the Chern number by  $\Delta C = 4$ .

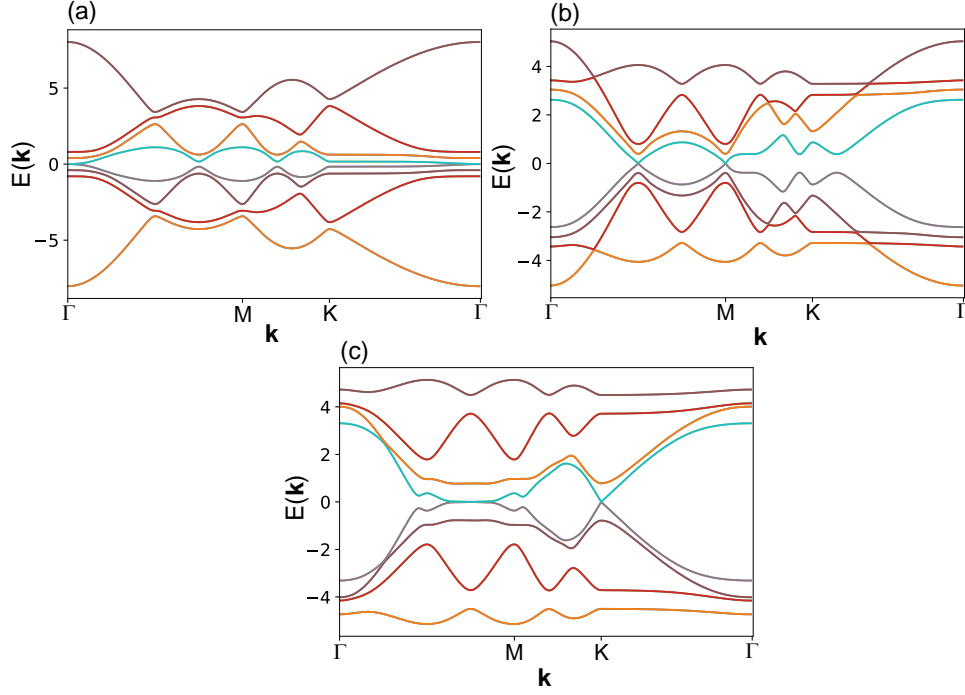


**Fig. 3.6:** Band structure (a) at  $(\mu, \Delta, JS) = (2.0t, 0.4t, 0.4t)$  exhibiting a quadratic gap closing at  $\Gamma$ , (b) at  $(\mu, \Delta, JS) = (-2.0t, 0.4t, 0.71t)$  exhibiting a linear gap closing at M and (c) at  $(\mu, \Delta, JS) = (-1.0t, 0.4t, 0.4t)$  exhibiting a linear gap closing at K.

For the high symmetry point  $\Gamma$ , the scenario is more complicated. For this high symmetry point, two degenerate bands have a gap closing, but a transition from the trivial phase to a topological phase of  $C = 4$  occurs. When the dispersion is analyzed for this gap closing, which is portrayed in Fig. 3.6 (a) at  $(\mu, \Delta, JS) = (-1.0t, 0.4t, 0.4t)$ , it shows a quadratic dependence on  $\mathbf{k}$ . For small values of  $|\mathbf{k}|$ , this dispersion was fitted at the phase transition at the set of parameters  $(\mu, \Delta, JS) = (-1.0t, 0.4t, 0.4t)$  along three lines in the Brillouin zone, namely from  $\Gamma$  to the end points M, K and  $\frac{M+K}{2}$ . For these lines, the fitting function  $a|k|^2 + e$  yields almost equal values for  $a$  and  $e \approx 0$  in all three cases. Therefore, the dispersion appears isotropic in close proximity to  $\Gamma$ . Overall, the quadratic character of the gap closing combined with the double degeneracy of the bands seems to generate the phase

transition of  $\Delta C = 4$ .

Finally, the gap closing at M is determined by the analytic expression

$$(3J^2 + 4t^2 - 3\Delta^2 - 3\mu^2)^2 = 16t^2(3\mu^2 - 8t^2 - 6\Delta^2), \quad (3.34)$$

which is found from an analytic diagonalization of the Hamiltonian at this high symmetry point in Mathematica [61]. This relation between  $J$  and  $\mu$  results in four branches for a specific value of  $\Delta$ , which causes two symmetric phases around  $\mu = 0$  to emerge in the phase diagram in Fig. 3.5. The gap closing at M once again shows a linear Dirac cone in the band structure, which is presented in Fig. 3.6 (b) for the set of parameters  $(\mu, \Delta, JS) = (-2.0t, 0.4t, 0.71t)$ . Combined with the double degeneracy of the bands as well as the multiplicity of 3 for the high symmetry point M in the Brillouin zone, these gap closings induce a change in the Chern number by  $\Delta C = \pm 6$ . Where phases originating from gap closings at different high symmetry points overlap, the respective Chern numbers are added. Thereby, the section in the phase diagram, where the left phase originating from M with a Chern number of  $C = -6$  overlaps with the phase of  $C = 4$  originating from K, has a Chern number of  $C = -2$ . Similarly, the section where the right phase originating from M is seen has an overall Chern number of  $C = 2$ , because this phase is fully immersed in the phase originating from the gap closing at  $\Gamma$ .

## 3.4 Edge Modes on Magnetic Islands

For the topological phase, Majorana zero-energy modes are predicted to occur on boundaries connecting to regions in the trivial phase. For MSH structures, such a boundary is determined by the edge of the magnetic adatoms placed onto the superconducting substrate. Thereby, the topological character of the system can be analyzed in real space by computing the local density of states. In order to simulate a lattice of  $N_1 \times N_2$  sites in real space, the numerical calculations were performed using the Kwant python package [62]. By employing the methods from Kwant, both one- and two-dimensional lattices can be created including on-site elements of the Hamiltonian as well as hopping terms and their eigenenergies and eigenstates can be calculated. Therein,  $N_1$  refers to the number of sites in direction of  $\mathbf{a}_1$  and  $N_2$  to the number of sites in direction of  $\mathbf{a}_2$ .

### 3.4.1 Circular Islands

Firstly, a circular island of magnetic adatoms was considered, as illustrated in Fig. 3.7 (a), where the four colors red, blue, green and yellow represent the four possible

spin orientations as they are ordered in Eq. (3.1). The black color shows where no magnetic adatoms are placed onto the superconducting substrate.

The local density of states at zero energy is calculated from Eq. (2.6), for which the eigenenergies and eigenstates are needed. These can be calculated in real space by diagonalizing the Hamiltonian in Eq. (2.1c). Here, the Hamiltonian was diagonalized for a  $70 \times 70$  lattice with periodic boundary conditions. The result of calculating the local density of states (LDOS) at an energy of zero for this system is shown in Fig. 3.7 (b) for the chosen parameter set of  $(\mu, \Delta, JS) = (-1.0t, 0.4t, 1.5t)$ . These parameters correspond to the topological phase with a Chern number of  $C = 4$ .

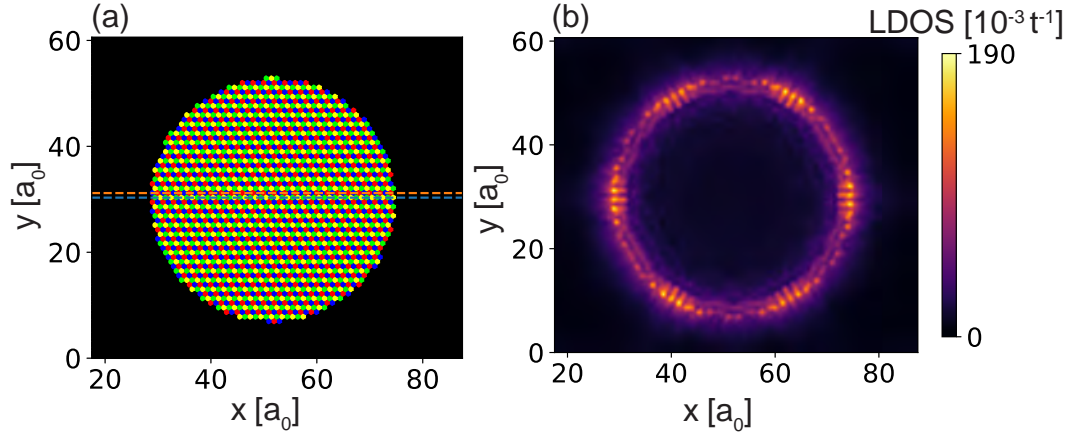


**Fig. 3.7:** (a) Spatial plot of the island of magnetic adatoms with the colors representing the four spin orientations of the 3Q structure, where the blue and orange dashed lines denote the  $y$ -coordinate where the horizontal cuts for Fig. 3.8 are taken, (b) Zero-energy LDOS of the island of magnetic adatoms in the  $C = 4$ -phase with the magnitude described by a linear color scale.

The computed result in Fig. 3.7 (b) clearly shows that the LDOS is localized at the edge of the island, shown in Fig. 3.7 (a). Thereby, the expected Majorana modes are present and can be detected experimentally. Fig. 3.8 shows a plot of the LDOS dependent on  $x$  at  $y \in \{35, 36\} \frac{\sqrt{3}}{2} a_0$ . These values for  $y$  correspond to the sites at the middle of the island, which are also marked by two dashed lines in the same colors in Fig. 3.7 (a).

By looking at this type of cuts through the island along one line through the island, it can be seen that the LDOS declines rapidly from the edge of the island towards its center. At both values for  $y$  the LDOS is not symmetric, because the maxima in the LDOS from Fig. 3.7 (b) are especially prominent at every second site along the edge. Thereby, a site with a less prominent maximum of the LDOS lies across the cut along  $y = \frac{\sqrt{3}}{2} 35 a_0$ , which corresponds to the blue line in Fig. 3.8. However, the

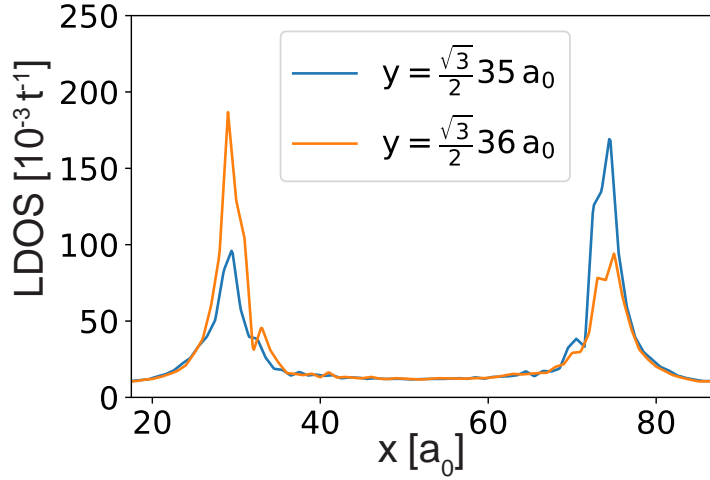


**Fig. 3.8:** Line-cuts of the LDOS on the circular island at  $y \in \{35, 36\} \frac{\sqrt{3}}{2} a_0$  in the  $C = 4$ -phase.

orange line corresponding to the LDOS at  $y = \frac{\sqrt{3}}{2} 36 a_0$  is approximately the mirrored version of the blue line around the center of the island. The deviations in the course of the two lines can be traced back to numerical inaccuracies, which would not be present for larger systems. Thereby, it can be seen that these two line-cuts of the LDOS through the island are symmetric to one another.

### 3.4.2 Introducing Disorder

Majorana zero-energy modes are especially interesting as a candidate for quantum computation, as they are robust to disorder. In order to test whether the edge modes on the island are stable towards disorder, one possibility is to simulate an irregularly shaped island.

As the  $C_3$ -symmetry of the spin structure is then no longer present on the lattice, the system is more disordered. The chosen shape for the island is shown in Fig. 3.9 (a), which was generated from a black-and-white picture [63]. This picture was imported into the code, where the colors were used as a True/False mask. The color white here stands for the space, where the magnetic adatoms are located, and the color black denotes where no magnetic adatoms are placed above the superconducting substrate. Thereby, any island generated during an experiment can be simulated from a black-and-white picture of the island's shape. The result for the computation of the zero-energy LDOS on a lattice of  $N_1 = 70$  and  $N_2 = 70$  sites is shown in Fig. 3.9 (b). Despite the irregular shape of the magnetic island, the local density of

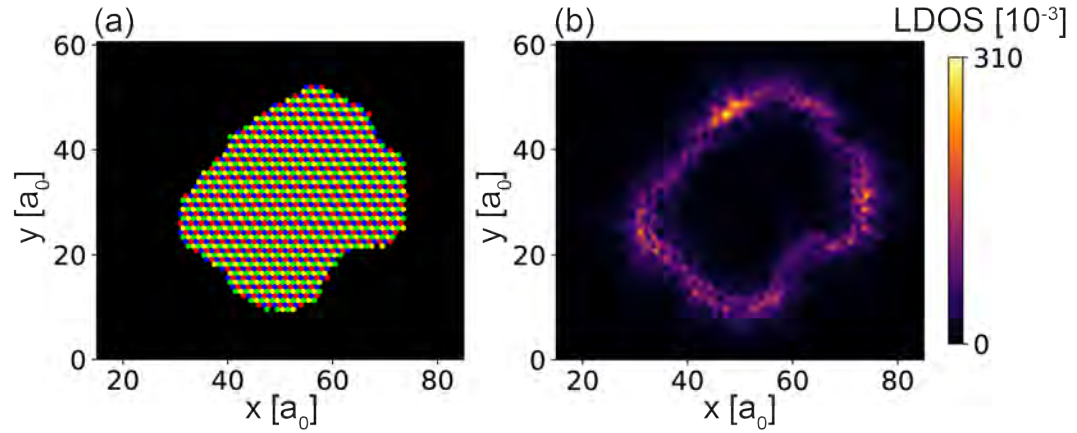


**Fig. 3.9:** (a) Spatial plot of the irregularly shaped island of magnetic adatoms with the colors representing the four different spin orientations of the 3Q structure, (b) zero-energy LDOS of the irregularly shaped island of magnetic adatoms in the  $C = 4$ -phase.

states still exhibits high peaks on the edge of the island. Thereby, the calculated edge modes are stable towards disorder, as they remain localized on the boundary of the island and therefore appear to be topologically protected from disorder.

### 3.4.3 Supercurrents

Next, the supercurrents were calculated for this shape of the magnetic island, as explained in section 2.5. As the eigenenergies and corresponding eigenvectors of the Hamiltonian were already calculated previously, all prerequisites for the calculation are given. The result for the supercurrent from all occupied energy modes is shown in Fig. 3.10. As explained before, all contributions from the bonds to the nearest neighboring sites were averaged with the connecting vectors as weights, rendering a vectorized graphic representation of the supercurrent flowing through each site.

This plot shows that the supercurrent is localized on the very edge of the island and proceeds counter-clockwise around the entire boundary for this phase. Therefore, the current possesses a clear chirality. Calculating the current for other topological phases leads to the conclusion that the direction of the current flips when the sign of the Chern number is inverted  $C \rightarrow -C$ .

As the current calculated here stems from a sum over the different contributions from all occupied eigenstates, it can also be separated into partial sums over certain energy ranges. In Fig. 3.11, the entire current and its separation into

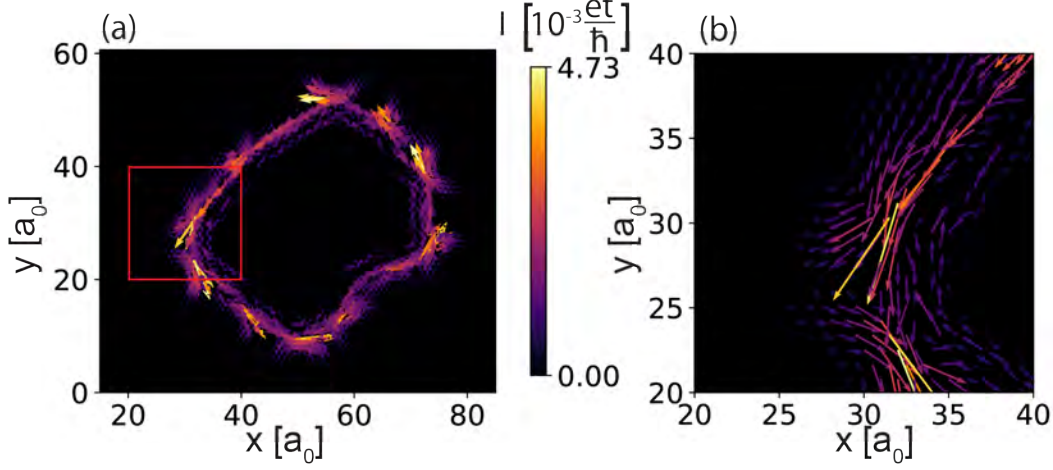


**Fig. 3.10:** (a) Calculated supercurrent flowing through each site, with the arrows denoting the current's orientation, for the 3Q structure in the  $C = 4$ -phase, and (b) zoomed-in area on the island marked by the red square in (a).

three contributing energy ranges is shown, in order to compare the topological  $C = 4$ -phase at  $(\mu, \Delta, JS) = (-1.0t, 0.4t, 1.0t)$  with the trivial  $C = 0$ -phase at  $(\mu, \Delta, JS) = (-4.0t, 0.4t, 1.0t)$ . Inside the magnetic island, the gap width is reduced to an effective gap width  $\Delta_{\text{eff}}$ , which is demonstrated later in section 3.5.3. Therefore, the entire energy range  $[E_{\text{min}}, 0]$  is split into energies below the superconducting order parameter  $[E_{\text{min}}, -\Delta]$  denoted by 'Bulk', between the superconducting order parameter and the effective reduced gap on the island  $(-\Delta, -\Delta_{\text{eff}})$  denoted by 'Between', and energies above the effective gap  $[-\Delta_{\text{eff}}, 0]$  denoted by 'In-Eff-Gap'. As only the occurring Majorana modes possess energies greater than the effective gap, because they traverse the entire gap width, they are the only modes contributing to the third energy interval.

The result in Fig. 3.11 shows that in the topological case, all three energy intervals show ordered supercurrents localized on the edge of the magnetic island with defined chiralities. While the contributions from the first energy interval, the bulk modes, move clockwise around the island, the other two contributions move counter-clockwise around the island with the Majorana modes from the third interval generating the greatest magnitude of the supercurrent.

Compared to the supercurrent for the topological phase, the supercurrent in the trivial phase is smaller by a factor of approximately 10. Nevertheless, there is still a localized current visible on the edge of the current running clockwise around the

island. As no Majorana modes traverse the superconducting gap, the third energy interval does not contribute anything to the overall supercurrent. The two other energy intervals show very disordered contributions of no defined chirality, which also penetrate into the inside of the island.

These results suggest the conclusion that a strong, ordered supercurrent in contrast to a weaker, disordered one can be employed as a means to distinguish topological from trivial phases.

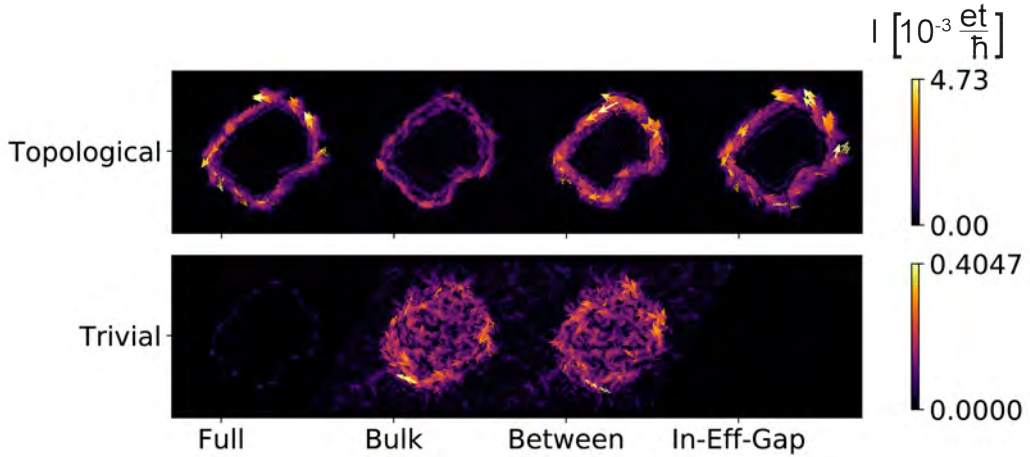


**Fig. 3.11:** Separated supercurrent contributions for the 3Q structure in the  $C = 4$ -phase and the trivial phase at  $(\mu, \Delta, JS) = (-4.0t, 0.4t, 1.0t)$ .

### 3.5 Edge Modes on Ribbon Structures

Taking an approach to MSH systems by simulating islands of magnetic adatoms comes with certain disadvantages. Simulating these islands requires the diagonalization of quadratic matrices with dimension  $4N_1N_2$ . In order to achieve a good accuracy,  $N_1$  and  $N_2$  have to be very large numbers, leading to long computation times. These large matrices also take up a lot of storage space, which renders this method less efficient.

Treating the Hamiltonian in the reduced Brillouin zone through a Fourier transformation allows for a more efficient calculation. However, Fourier transforming the Hamiltonian requires a fully translationally invariant system and thus does not allow edges to be included in the system. So, for the purpose of observing Majorana modes on the edges of the magnetic layer combined with the effectiveness of the reduced Brillouin zone, partially infinite systems suggest themselves.

Therefore, systems that are infinite along one direction of the triangular lattice, e.g. in direction of  $\mathbf{a}_1$  are now analyzed. In the other direction of  $\mathbf{a}_2$ , the system remains finite. In the finite direction, the magnetic adatoms are only placed on a part of the simulated sites, creating two edges. Here, periodic boundary conditions are employed as well.

The spatial structure of this kind of system is shown in Fig. 3.12 and will be referred to as a ribbon of magnetic adatoms from hereon. By employing this kind of magnetic structure for the computations, the size of the matrices that need to be diagonalized is reduced to  $8N_1$ . This dimension includes the number of sites in direction of  $\mathbf{a}_1$ , the two sites of the unit cell in direction of  $\mathbf{a}_2$  and the dimension of the employed Nambu space.

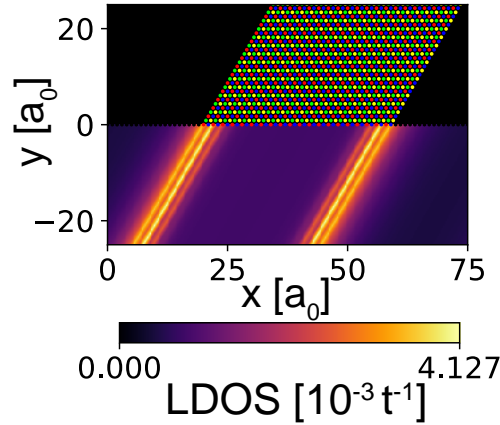


**Fig. 3.12:** Spatial plot of the ribbon structure with displayed zero-energy LDOS for  $(\mu, \Delta, JS) = (-1.0t, 0.4t, 1.0t)$  in the topological phase of  $C = 4$ .

Beforehand, the LDOS was calculated in real space for a system with 80 sites in direction of  $\mathbf{a}_1$  and 40 sites in direction of  $\mathbf{a}_2$  analogously to the procedure for island structures from before. Here, half of the system's sites are covered with magnetic adatoms, creating a ribbon of infinite direction in  $\mathbf{a}_2$ , which is shown in Fig. 3.12. The result for the LDOS is depicted Fig. 3.12 as well, which shows edge modes emerging on the boundary of the magnetic layer. It was calculated for the set of parameters of  $(\mu, \Delta, JS) = (-1.0t, 0.4t, 1.0t)$ , which corresponds to a Chern number of  $C = 4$ . Thereby, it can be deduced that the possibility to predict the experimental results during STS measurements is maintained when magnetic ribbons are investigated instead of magnetic islands.

Next, the supercurrent was calculated for this system and the same set of parameters. The result is depicted in Fig. 3.13.

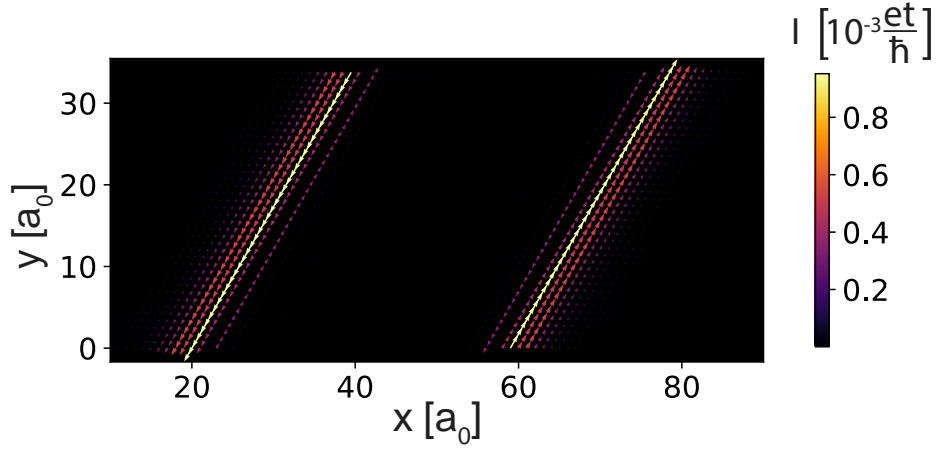


**Fig. 3.13:** Calculated supercurrent on the ribbon structure for  $(\mu, \Delta, JS) = (-1.0t, 0.4t, 1.0t)$  in the topological phase of  $C = 4$ .

Here, the supercurrent points along the boundary of the ribbon, wherein its orientation is opposite on the two different edges. Apart from a small contribution further inside the ribbon, all of the supercurrents on one edge have the same orientation. The magnitude of the computed supercurrents also declines rapidly away from the boundary of the magnetic ribbon. Therefore, this result demonstrates a localization on the boundary of the ribbon and a defined chirality along the edges.

### 3.5.1 Introducing Disorder

Just like for the island of magnetic adatoms, a ribbon with perfectly ordered edges is unlikely to be created experimentally. Therefore, the robustness of the Majorana zero-energy modes towards disorder needs to be tested. In order to create the disordered edges displayed in Fig. 3.14, a random walk is conducted both on the left as well as on the right edge. From the original starting points  $\mathbf{r}_L, \mathbf{r}_R = (\frac{N_1}{4}, \frac{3N_1}{4})\mathbf{a}_1$  of the edge at  $y = 0$ , each position of the edge along the ribbon is determined by drawing a random number out of  $[-1, 0, 1]$ . Adding the randomly determined number to the previous position of the edge allows the edge to be moved one site to the left, to remain the same or to be moved one site to the right.

Next, the local density of states was calculated for this specific ribbon in real space with the result shown in Fig. 3.15. This calculation was conducted for the same set of parameters as for the data shown in Fig. 3.12. The Majorana modes on the edge

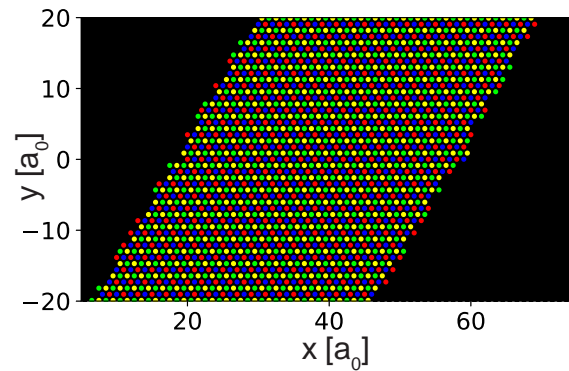


**Fig. 3.14:** Spatial plot of the ribbon structure with irregular edges.

of the ribbon remain localized, but spread out more into the center of the ribbon. Therefore, it can be concluded that they are stable towards disorder.

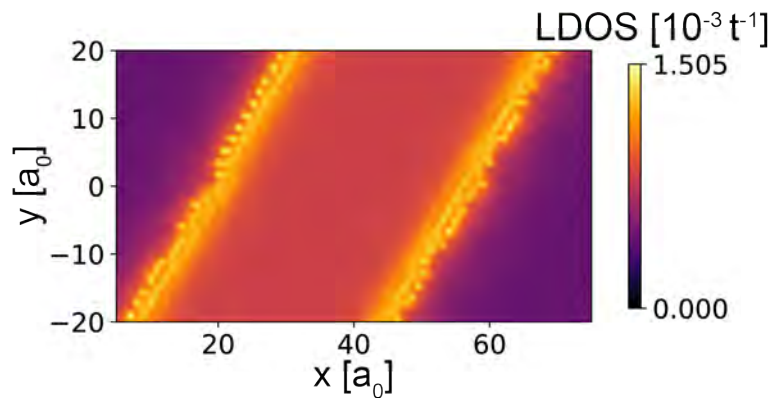


**Fig. 3.15:** Zero-energy LDOS for the ribbon structure in real space with disordered edges.

### 3.5.2 Theoretical Method for Partially Infinite Systems

For the theoretical analysis of a ribbon structure, the creation and annihilation operators as well as the Hamiltonian have to be Fourier transformed in one direction.



### 3.5.3 Band Structure

With the transformed form of the Hamiltonian from Eq. (3.39), the band structure can be calculated in dependence of  $k_{\parallel}$ . In order to do so, a Kwant simulation of a chain of atoms with the on-site and hopping matrix given through Eq. (3.39) was programmed. Then, this matrix was diagonalized for a certain number of points for  $k_{\parallel} \in \left[-\frac{\pi}{2a_0}, \frac{\pi}{2a_0}\right]$ . To obtain the band structure depicted below in Fig. 3.16, a chain of 120 unit cells was simulated for the set of parameters  $(\mu, \Delta, JS) = (-1.0t, 0.4t, 1.0t)$ , with the domain of definition for  $k_{\parallel}$  being split into  $n_k = 700$  points.

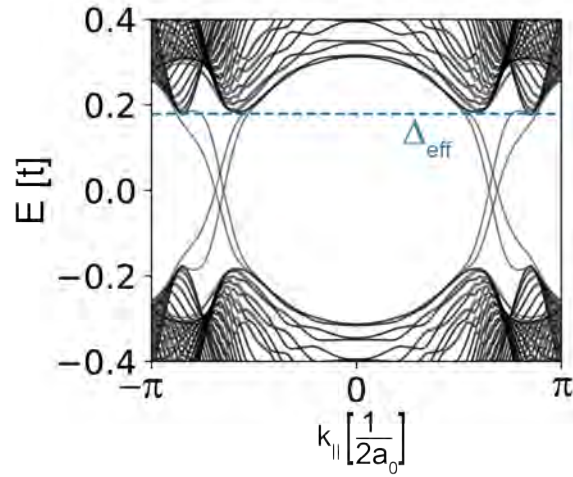


**Fig. 3.16:** Dispersion in dependence of  $k_{\parallel}$  in the  $C = 4$ -phase.

Here, the band structure is shown for energies  $E \in [-\Delta, \Delta]$ . The bands are symmetric around  $k_{\parallel} = 0$  and also around  $E = 0$  due to particle-hole symmetry. The bulk bands emerge at almost half the size of the superconducting order parameter, which shows that it is reduced to a much smaller effective gap width  $\Delta_{\text{eff}}$  by the magnetic structure. These bulk bands are characterized by a continuum of bands emerging above the reduced gap  $|E| \geq \Delta_{\text{eff}}$ . This reduced gap width is an effect of the added magnetic layer and will be discussed further in the following.

Inside the effective gap, eight modes can be perceived that traject across the superconducting gap between the lower and the upper bulk. Four of these are right movers with  $\frac{\partial E}{\partial k_{\parallel}} > 0$  localized on the upper edge of the ribbon and four modes are left movers localized on the other edge, respectively. This number of emerging Majorana modes corresponds to the Chern number  $C = 4$  of the analyzed topological phase [36]. As these modes cross the superconducting gap, they can be distinguished from trivial modes without this property. Still, this criterion is not sufficient to fully declare the

crossing modes as topological modes.

### 3.5.4 Local Density of States

For the Fourier transformed ribbon, the LDOS can be calculated both in dependence of the position in the finite direction of the ribbon as well as of the crystal momentum  $k_{\parallel}$  parallel to the stripe. The LDOS is calculated for an energy range of  $E \in [-0.4t, 0.4t]$  separated into 1601 equidistant points, by taking the eigenvalues and eigenvectors from the diagonalized Hamiltonian for the discretized range of  $k_{\parallel}$  and inserting them into Eq. (2.9) for each value of  $k_{\parallel}$ . In Fig. 3.17, the dependence on  $k_{\parallel}$  was integrated out as determined by

$$N(\mathbf{r}, \omega) = \int_{-\frac{\pi}{2a_0}}^{\frac{\pi}{2a_0}} N(k_{\parallel}, \mathbf{r}, \omega) dk_{\parallel} . \quad (3.40)$$

For the equidistant points, into which the interval for  $k_{\parallel}$  is discretized, this integral is approximated through the trapezoidal rule, rendering

$$N(\mathbf{r}, \omega) = \frac{\pi}{a_0 n_k} \sum_{n=0}^{n_k-1} N_{\mathbf{r}}(k_{\parallel, n}, \omega) \quad (3.41)$$

for  $k_{\parallel, n} = \frac{\pi}{2a_0 n_k} (n - \frac{n_k}{2})$  for  $n \in \{\mathbb{Z} \mid 0 \leq n \leq n_k\}$ .

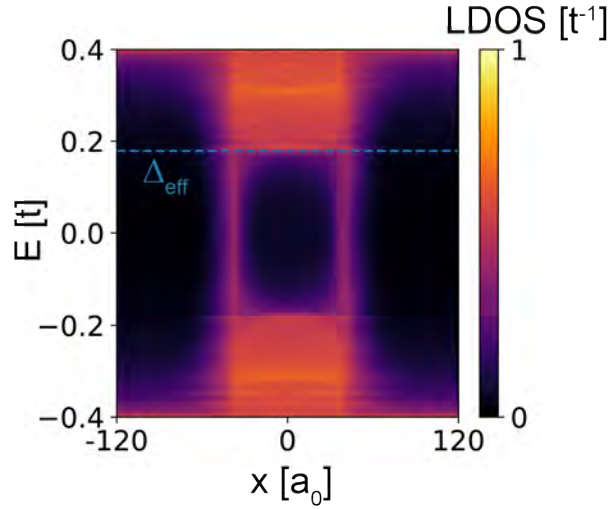
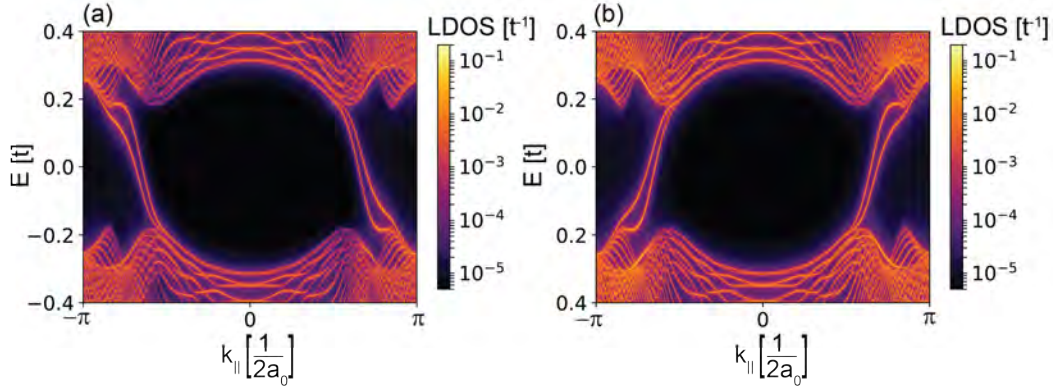


Fig. 3.17: Energy-dependent LDOS along the ribbon.

The result for this line-cut of the energy-resolved LDOS  $N(\mathbf{r}, E)$  along  $\mathbf{a}_2$ , shown in Fig. 3.17, reveals that the observed Majorana modes remain localized at the ribbon's edges for increasing energy. However, due to the modes' localization lengths, which increase with increasing energy [64], the modes also extend further away from the edge with increasing energy. Fig. 3.17 also shows that, inside the ribbon, the superconducting gap is suppressed by the presence of the magnetic 3Q structure, resulting in the aforementioned effective gap.

The Majorana modes on the ribbon also have a well-defined chirality, as it can be seen from an analysis of the momentum-resolved LDOS  $N(\mathbf{r}_1, k_{\parallel}, \omega)$  in Fig. 3.18. When  $\mathbf{r}_1 = \mathbf{r}_{L,R}$  is chosen as the lower or upper edge of the ribbon, respectively, we can see that all Majorana modes on the lower edge are left movers with  $\frac{\partial E}{\partial k_{\parallel}} < 0$  and all modes on the upper edge are right movers with  $\frac{\partial E}{\partial k_{\parallel}} > 0$ . The indices were chosen here to resemble 'Left' and 'Right', as the lower edge becomes the left edge on the chain, to which the two-dimensional system is transformed to, and the upper edge becomes the right one analogously.



**Fig. 3.18:** Spectral weight in the  $C = 4$ -phase (a) at the lower edge of the stripe  $\mathbf{r}_1 = \mathbf{r}_L$ , (b) at the upper edge  $\mathbf{r}_1 = \mathbf{r}_R$ .

### 3.6 Experimentally Motivated Model

From an experimental point of view, the triple-Q spin structure investigated so far is not an accurate representation of the experimentally realized spin structure. For a realization of the spin structure investigated here, the superconducting layer could be built out of atoms like rhenium and the magnetic layer could be built out of atoms like iron [23] or manganese [26]. Therein, the position of the magnetic adatoms will

not be directly above the sites where the superconducting atoms are located, because the magnetic adatoms are placed as an additional layer above the superconducting substrate without a layer inbetween [65]. Instead, their position is shifted to the center of three superconducting atoms, resulting in a close-packed structure. This AB-stacked positioning is shown in Fig. 3.19, where the position of the spins with respect to the triangular lattice below them is marked by red crosses.

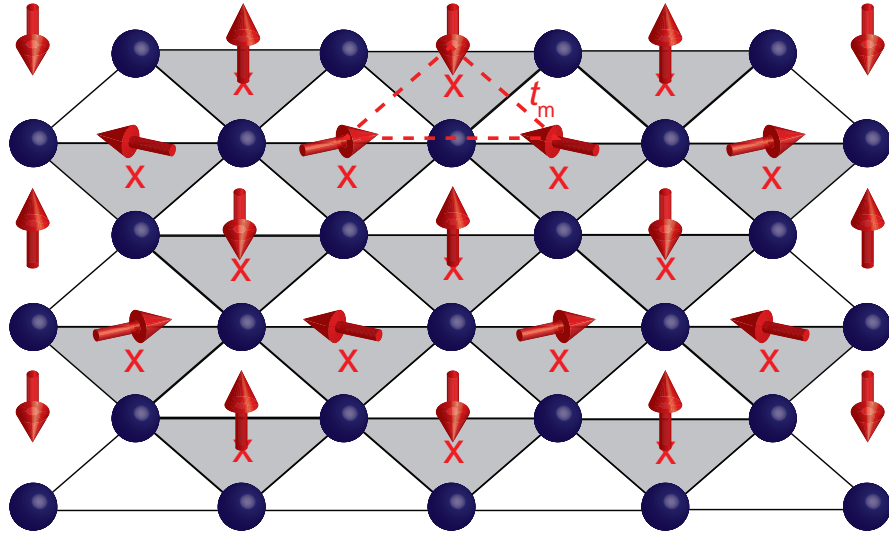


**Fig. 3.19:** Spatial spin structure for an AB-stacked magnetic layer, where the red crosses show the spatial positioning of the magnetic adatoms above the triangular lattice.

### 3.6.1 AB-Stacked Spin Structure without Electronic Degrees of Freedom

If the model analogous to model I from section 2.1 is investigated for an AB-stacked spin structure, every atom of the superconducting substrate interacts with three spins through the magnetic exchange coupling. As it can be seen in Fig. 3.19, the magnetic layer is shifted by a vector of  $(\overline{\mathbf{ab}})_0 = a_0 \left(0, \frac{1}{\sqrt{3}}\right)^T$ . Thereby, each atom in the superconducting substrate interacts with the magnetic adatoms placed at the

positions defined by the three connecting vectors

$$\overline{(\mathbf{ab})}_0 = a_0 \left( 0, \frac{1}{\sqrt{3}} \right)^T \quad (3.42a)$$

$$\overline{(\mathbf{ab})}_1 = a_0 \left( -\frac{1}{2}, -\frac{1}{2\sqrt{3}} \right)^T \quad (3.42b)$$

$$\overline{(\mathbf{ab})}_2 = a_0 \left( \frac{1}{2}, -\frac{1}{2\sqrt{3}} \right)^T. \quad (3.42c)$$

The adapted version of the magnetic exchange coupling term in the Hamiltonian then reads

$$\mathcal{H}'_m = J_{AB} \sum_{\mathbf{r} \in A, i \in \{0,1,2\}} c_{\mathbf{r}}^\dagger (\tau_0 \otimes (\mathbf{S}_{\mathbf{r}+\overline{(\mathbf{ab})}_i} \cdot \boldsymbol{\sigma})) c_{\mathbf{r}} \quad (3.43a)$$

$$= J_{AB} \sum_{\mathbf{r} \in A} c_{\mathbf{r}}^\dagger \left( \tau_0 \otimes \left( \sum_{i \in \{0,1,2\}} \mathbf{S}_{\mathbf{r}+\overline{(\mathbf{ab})}_i} \cdot \boldsymbol{\sigma} \right) \right) c_{\mathbf{r}} \quad (3.43b)$$

$$= J_{AB} \sum_{\mathbf{r} \in A} c_{\mathbf{r}}^\dagger (\tau_0 \otimes (\tilde{\mathbf{S}}_{\mathbf{r}} \cdot \boldsymbol{\sigma})) c_{\mathbf{r}}. \quad (3.43c)$$

This version of the Hamiltonian can be rearranged to match the Hamiltonian for the AA-stacked spin structure by summing over the three spins, with which the atom in the superconducting substrate interacts. In doing so in Eq. (3.43c), the averaged spin  $\tilde{\mathbf{S}}_{\mathbf{r}} = \sum_{i \in \{0,1,2\}} \mathbf{S}_{\mathbf{r}+\overline{(\mathbf{ab})}_i}$  at site  $\mathbf{r}$  is defined. These averaged spins are given by

$$\tilde{\mathbf{S}}_{\mathbf{R}_i} = S \begin{cases} (0, \sqrt{8}/3, 1/3)^T, & \mathbf{R}_0 = \mathbf{0} \\ (0, 0, -1)^T, & \mathbf{R}_1 = \mathbf{a}_1 \\ (-\sqrt{6}/3, -\sqrt{2}/3, 1/3)^T, & \mathbf{R}_2 = \mathbf{a}_2 \\ (\sqrt{6}/3, -\sqrt{2}/3, 1/3)^T, & \mathbf{R}_3 = \mathbf{a}_1 + \mathbf{a}_2 \end{cases} \quad (3.44)$$

in the unit cell, which corresponds to the inverted spin orientations from the original 3Q structure from Eq. (3.44). Thereby, the magnetic exchange coupling term matches the former version as well, with the same magnetic exchange coupling of  $J_{AB} = J$ . Due to this fact, this AB-stacked spin structure will render the same phase diagram with inverted signs of the Chern number as the AA-stacked spin structure. The inversion of the Chern numbers' sign is the result from the effective inversion of the spins.

### 3.6.2 Hamiltonian for Spins with Electronic Degrees of Freedom

In experiments, the magnetic layer will be built out of atoms such as manganese. Not only will these atoms have a spin that interacts with the superconducting substrate,

they will also have electronic degrees of freedom and thereby a band structure of their own. Thus, these electronic degrees of freedom for the magnetic layer have to be included in the computed model as well, in order to arrive at an experimentally more realistic simulation. For the combined structure of both the superconducting and magnetic layers, the Hamiltonian for this experimentally motivated model reads

$$\mathcal{H} = \mathcal{H}_0 + \mathcal{H}_m'' + \mathcal{H}_{\text{hyb}} \quad (3.45a)$$

with

$$\mathcal{H}_m'' = -t_m \sum_{\mathbf{r}, \mathbf{r}' \in M, \sigma} d_{\mathbf{r}, \sigma}^\dagger d_{\mathbf{r}', \sigma} - \mu_m \sum_{\mathbf{r} \in M, \sigma} d_{\mathbf{r}, \sigma}^\dagger d_{\mathbf{r}, \sigma} + J \sum_{\mathbf{r} \in M, \alpha, \beta} d_{\mathbf{r}, \alpha}^\dagger (\mathbf{S}_{\mathbf{r}} \cdot \boldsymbol{\sigma})_{\alpha\beta} d_{\mathbf{r}, \beta}, \quad (3.45b)$$

$$\mathcal{H}_{\text{hyb}} = -t_{\text{hyb}} \sum_{\mathbf{r} \in A, \mathbf{r}' \in M, \sigma} (c_{\mathbf{r}, \sigma}^\dagger d_{\mathbf{r}', \sigma} + \text{h.c.}), \quad (3.45c)$$

where  $\mathcal{H}_0$  from Eq. (2.1b) is employed. In this model, the magnetic layer has a band structure characterized by its own hopping amplitude  $t_m$ , chemical potential  $\mu_m$  and the magnetic exchange coupling  $J$ , which are solely applied to the creation and annihilation operators  $d_{\mathbf{r}}^{(\dagger)}$  for the magnetic layer. Here, the fermionic operators describing the magnetic layer also act on a triangular sublattice, which is denoted by  $M$ . The positioning of  $M$  relative to the lattice of the superconducting substrate can be seen in Fig. 3.19, where the positioning of the magnetic adatoms is illustrated by the red marks. These two sublattices  $A$  and  $M$  interact through a hybridization term  $\mathcal{H}_{\text{hyb}}$ , which consists of a hopping between nearest neighboring sites of the two lattices with a hopping parameter  $t_{\text{hyb}}$ . This model will be referred to as model II from this point.

#### 3.6.3 Band Structure

To calculate the topological invariant for model II, it first has to be Fourier transformed to the reduced Brillouin zone from section 3.2. The RBZ remains the same, since the size of the unit cell is left unchanged through the modifications. The transformation and its inverse are given through

$$c_{\mathbf{r}, \mathbf{R}_i} = \frac{1}{\sqrt{N_1 N_2}} \sum_{\mathbf{k} \in \text{RBZ}} c_{\mathbf{k}, \mathbf{R}_i} e^{i\mathbf{k} \cdot \mathbf{r}}, \quad (3.46)$$

$$c_{\mathbf{k}, \mathbf{R}_i} = \frac{1}{\sqrt{N_1 N_2}} \sum_{\mathbf{r} \in A} c_{\mathbf{r}, \mathbf{R}_i} e^{-i\mathbf{k} \cdot \mathbf{r}}, \quad (3.47)$$

as for model I and

$$d_{\mathbf{r}', \mathbf{R}_i + \overline{(\mathbf{ab})}_0} = \frac{1}{\sqrt{N_1 N_2}} \sum_{\mathbf{k} \in \text{RBZ}} c_{\mathbf{k}, \mathbf{R}_i + \overline{(\mathbf{ab})}_0} e^{i\mathbf{k} \cdot \mathbf{r}'}, \quad (3.48)$$

$$d_{\mathbf{k}, \mathbf{R}_i + \overline{(\mathbf{ab})}_0} = \frac{1}{\sqrt{N_1 N_2}} \sum_{\mathbf{r}' \in M} c_{\mathbf{r}', \mathbf{R}_i + \overline{(\mathbf{ab})}_0} e^{-i\mathbf{k} \cdot \mathbf{r}'}. \quad (3.49)$$

The Fourier transformed Hamiltonian then reads

$$\mathcal{H} = \sum_{\mathbf{k} \in \text{RBZ}} f_{\mathbf{k}}^\dagger \hat{H}_{\text{AB}}(\mathbf{k}) f_{\mathbf{k}} \quad (3.50)$$

with

$$\hat{H}_{\text{AB}}(\mathbf{k}) = \begin{pmatrix} \hat{A}_{\text{AB}} & \hat{C}_{\text{AB}} \\ \hat{C}_{\text{AB}}^\dagger & \hat{D}_{\text{AB}} \end{pmatrix} \quad (3.51)$$

where the matrices

$$\begin{aligned} \hat{A}_{\text{AB}} &= \begin{pmatrix} \Delta\tau_x - \mu\tau_z & -2tc_0\tau_z & -2tc_1\tau_z & -2tc_2\tau_z \\ -2tc_0\tau_z & \Delta\tau_x - \mu\tau_z & -2tc_2\tau_z & -2tc_1\tau_z \\ -2tc_1\tau_z & -2tc_2\tau_z & \Delta\tau_x - \mu\tau_z & -2tc_0\tau_z \\ -2tc_2\tau_z & -2tc_1\tau_z & -2tc_0\tau_z & \Delta\tau_x - \mu\tau_z \end{pmatrix} \otimes \sigma_0, \\ \hat{B}_{\text{AB}} &= \begin{pmatrix} -\mu_m\tau_z & -2t_m c_0\tau_z & -2t_m c_1\tau_z & -2t_m c_2\tau_z \\ -2t_m c_0\tau_z & -\mu_m\tau_z & -2t_m c_2\tau_z & -2t_m c_1\tau_z \\ -2t_m c_1\tau_z & -2t_m c_2\tau_z & -\mu_m\tau_z & -2t_m c_0\tau_z \\ -2t_m c_2\tau_z & -2t_m c_1\tau_z & -2c_0\tau_z & -\mu_m\tau_z \end{pmatrix} \otimes \sigma_0 \\ &+ \begin{pmatrix} J\tau_0 \otimes (\mathbf{S}_0 \cdot \boldsymbol{\sigma}) & 0 & 0 & 0 \\ 0 & J\tau_0 \otimes (\mathbf{S}_1 \cdot \boldsymbol{\sigma}) & 0 & 0 \\ 0 & 0 & J\tau_0 \otimes (\mathbf{S}_2 \cdot \boldsymbol{\sigma}) & 0 \\ 0 & 0 & 0 & J\tau_0 \otimes (\mathbf{S}_3 \cdot \boldsymbol{\sigma}) \end{pmatrix}, \end{aligned} \quad (3.52)$$

and

$$\hat{C}_{\text{AB}} = \begin{pmatrix} -t_{\text{hyb}} e_0 \tau_z & 0 & -t_{\text{hyb}} e_1 \tau_z & -t_{\text{hyb}} e_2 \tau_z \\ 0 & t_{\text{hyb}} e_0 \tau_z & -t_{\text{hyb}} e_2 \tau_z & -t_{\text{hyb}} e_1 \tau_z \\ -t_{\text{hyb}} e_1 \tau_z & -t_{\text{hyb}} e_2 \tau_z & -t_{\text{hyb}} e_0 \tau_z & 0 \\ -t_{\text{hyb}} e_2 \tau_z & -t_{\text{hyb}} e_1 \tau_z & 0 & -t_{\text{hyb}} e_0 \tau_z \end{pmatrix} \otimes \sigma_0 \quad (3.54)$$

as well as the combined spinors

$$f_{\mathbf{k}} = (c_{\mathbf{k}, \mathbf{R}_0}, c_{\mathbf{k}, \mathbf{R}_1}, c_{\mathbf{k}, \mathbf{R}_2}, c_{\mathbf{k}, \mathbf{R}_3}, d_{\mathbf{k}, \mathbf{R}_0 + \overline{(\mathbf{ab})}_0}, d_{\mathbf{k}, \mathbf{R}_1 + \overline{(\mathbf{ab})}_0}, d_{\mathbf{k}, \mathbf{R}_2 + \overline{(\mathbf{ab})}_0}, d_{\mathbf{k}, \mathbf{R}_3 + \overline{(\mathbf{ab})}_0})^T. \quad (3.55)$$

were employed. Here, we defined the abbreviations

$$c_0 = \cos(\mathbf{k} \cdot \mathbf{a}_1), \quad e_0 = e^{-i\mathbf{k} \cdot \overline{(\mathbf{ab})}_0}, \quad (3.56a)$$

$$c_1 = \cos(\mathbf{k} \cdot \mathbf{a}_2), \quad e_1 = e^{-i\mathbf{k} \cdot \overline{(\mathbf{ab})}_1}, \quad (3.56b)$$

$$c_2 = \cos(\mathbf{k} \cdot (\mathbf{a}_2 - \mathbf{a}_1)), \quad e_2 = e^{-i\mathbf{k} \cdot \overline{(\mathbf{ab})}_2}. \quad (3.56c)$$

The employed spinors are given by

$$c_{\mathbf{k}, \mathbf{R}_i} = (c_{\mathbf{k}, \mathbf{R}_i, \uparrow}, c_{\mathbf{k}, \mathbf{R}_i, \downarrow}, c_{\mathbf{k}, \mathbf{R}_i, \downarrow}^\dagger, -c_{\mathbf{k}, \mathbf{R}_i, \uparrow}^\dagger)^\text{T} \quad (3.57)$$

as before and

$$d_{\mathbf{k}, \mathbf{R}_i + \overline{(\mathbf{ab})}_0} = (d_{\mathbf{k}, \mathbf{R}_i + \overline{(\mathbf{ab})}_0, \uparrow}, d_{\mathbf{k}, \mathbf{R}_i + \overline{(\mathbf{ab})}_0, \downarrow}, d_{\mathbf{k}, \mathbf{R}_i + \overline{(\mathbf{ab})}_0, \downarrow}^\dagger, -d_{\mathbf{k}, \mathbf{R}_i + \overline{(\mathbf{ab})}_0, \uparrow}^\dagger)^\text{T}, \quad (3.58)$$

which both contain all particle- and hole-like creation and annihilation operators for both spin orientations.

The AB-stacked system in model II incorporates the same symmetry as the AA-stacked system from model I, described in section 3.2.1. By extending the already found symmetry transformation so that it is applied to both layers in the structure it can be used for  $\hat{H}_{\text{AB}}(\mathbf{k})$  as well.

With another projection matrix

$$\hat{P}_2 = \begin{pmatrix} 1 & 0 & 0 & 0 \\ 0 & 0 & 1 & 0 \\ 0 & 1 & 0 & 0 \\ 0 & 0 & 0 & 1 \end{pmatrix} \otimes \mathbb{1}_{8 \times 8} \quad (3.59)$$

the full transformation with  $\hat{U}_{\hat{S}}$  from Eq. (3.22) is modified to read

$$\hat{U}_{\hat{S}_{\text{AB}}} = \begin{pmatrix} \hat{U}_{\hat{S}} & 0 \\ 0 & \hat{U}_{\hat{S}} \end{pmatrix} \cdot \hat{P}_2. \quad (3.60)$$

The matrix  $\hat{P}_2$  serves the purpose of rendering the transformed Hamiltonian in two  $16 \times 16$  blocks. It is found through the condition that  $\hat{U}_{\hat{S}_{\text{AB}}}$  then should render the extended version  $\hat{S}_{\text{AB}}$  of the symmetry matrix  $\hat{S}$  diagonal with its eigenvalues sorted by magnitude, where we defined  $\hat{S}_{\text{AB}}$  as

$$\hat{S}_{\text{AB}} = \begin{pmatrix} \hat{S} & 0 \\ 0 & \hat{S} \end{pmatrix}. \quad (3.61)$$

By applying the transformation  $\hat{U}_{\hat{S}_{AB}}$  to  $\hat{H}_{AB}(\mathbf{k})$ , it takes the form

$$\hat{\tilde{H}}_{AB}(\mathbf{k}) = \hat{U}_{\hat{S}_{AB}}^\dagger \hat{H}_{AB}(\mathbf{k}) \hat{U}_{\hat{S}_{AB}} \quad (3.62a)$$

$$= \begin{pmatrix} \hat{H}'_{AB}(\mathbf{k}) & 0 \\ 0 & (i\mathbb{1}_{4 \times 4} \otimes \tau_z \otimes \sigma_y) \hat{H}'_{AB}(-\mathbf{k})^* (i\mathbb{1}_{4 \times 4} \otimes \tau_z \otimes \sigma_y) \end{pmatrix}. \quad (3.62b)$$

In this equation, the block-matrix  $\hat{H}'_{AB}(\mathbf{k})$  is derived as

$$\hat{H}'_{AB}(\mathbf{k}) = \begin{pmatrix} \hat{A}'_{AB} & \hat{C}'_{AB} \\ (\hat{C}'_{AB})^\dagger & \hat{B}'_{AB} \end{pmatrix} \quad (3.63)$$

with

$$\hat{A}'_{AB} = \begin{pmatrix} (-2tc_0 - \mu)\sigma_z + \Delta\sigma_x & 0 & & & \\ 0 & (2tc_0 - \mu)\sigma_z + \Delta\sigma_x & & & \dots \\ -4tc_1c_2\sigma_z & 0 & & & \\ 0 & 4ts_1s_2\sigma_z & & & \\ -4tc_1c_2\sigma_z & 0 & & & \\ 0 & 4ts_1s_2\sigma_z & & & \\ \dots & (-2tc_0 - \mu)\sigma_z + \Delta\sigma_x & & & \\ & 0 & & & \\ & (2tc_0 - \mu)\sigma_z + \Delta\sigma_x & & & \end{pmatrix}, \quad (3.64)$$

$$\hat{B}'_{AB} = \begin{pmatrix} \frac{J}{\sqrt{3}}\sigma_0 - (2t_m c_0 + \mu_m)\sigma_z & i\sqrt{\frac{2}{3}}J\sigma_0 & & & \\ -i\sqrt{\frac{2}{3}}J\sigma_0 & -\frac{J}{\sqrt{3}}\sigma_0 + (2t_m c_0 - \mu_m)\sigma_z & & & \dots \\ -4t_m c_1 c_2 \sigma_z & 0 & & & \\ 0 & 4t_m s_1 s_2 \sigma_z & & & \\ -4t_m c_1 c_2 \sigma_z & 0 & & & \\ 0 & 4t_m s_1 s_2 \sigma_z & & & \\ \dots & -\frac{J}{\sqrt{3}}\sigma_0 - (2t_m c_0 + \mu_m)\sigma_z & & & \\ & \sqrt{\frac{2}{3}}J\sigma_0 & & & \\ & \frac{J}{\sqrt{3}}\sigma_0 + (2t_m c_0 - \mu_m)\sigma_z & & & \end{pmatrix}, \quad (3.65)$$

and

$$\hat{C}'_{AB} = \begin{pmatrix} -t_{\text{hyb}}e_1\sigma_z & 0 & -2t_{\text{hyb}}c_1e_2\sigma_z & 0 \\ 0 & -t_{\text{hyb}}e_1\sigma_z & 0 & -2it_{\text{hyb}}s_1e_2\sigma_z \\ -2t_{\text{hyb}}c_1e_2\sigma_z & 0 & -t_{\text{hyb}}e_1\sigma_z & 0 \\ 0 & -2it_{\text{hyb}}s_1e_2\sigma_z & 0 & -t_{\text{hyb}}e_1\sigma_z \end{pmatrix} \quad (3.66)$$

from calculations in Mathematica [61]. For reasons of brevity, we introduced the abbreviations

$$c_0 = \cos(k_x a_0), \quad c_1 = \cos\left(\frac{k_x a_0}{2}\right), \quad c_2 = \cos\left(\frac{\sqrt{3}k_y a_0}{2}\right), \quad (3.67a)$$

$$s_1 = \sin\left(\frac{1}{2}k_x a_0\right), \quad s_2 = \sin\left(\frac{\sqrt{3}k_y a_0}{2}\right), \quad (3.67b)$$

$$e_1 = e^{i\frac{1}{\sqrt{3}}k_y a_0} \quad \text{and} \quad e_2 = e^{i\frac{5\sqrt{3}}{6}k_y a_0}. \quad (3.67c)$$

### 3.6.4 Topological Phase Diagram

Now, with the block-diagonalized matrix representation of the Hamiltonian, the Chern number is calculated for model II as well analogously to the procedure described in section 3.3. To derive a topological phase diagram, we choose the same value for both chemical potentials  $\mu = \mu_m$  for reasons of simplicity and evaluate the Chern number in relation to the magnetic exchange coupling  $J$ .

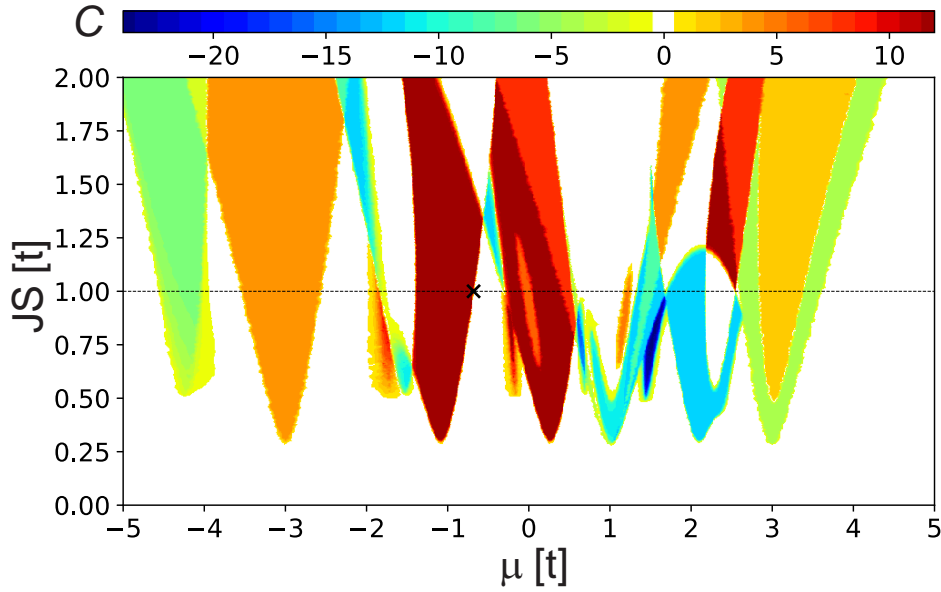


**Fig. 3.20:** Topological phase diagram for the AB-stacked spin structure in dependence of  $\mu$  and  $J$ , with the phase transition of  $\Delta C = 12$  marked by a black cross, for which the dispersion of the lowest lying energy band is analyzed in Fig. 3.21. The dashed black line marks the shared region of this phase diagram with Fig. 3.22 (a).

For the result in Fig. 3.20, the superconducting order parameter was set to  $\Delta = 0.3t$  and the different hopping parameters  $t = t_m = t_{\text{hyb}}$  were set to equal values with all energies measured in units of  $t$ . Compared to the former phase diagram, a larger number of topological phases emerges with a greater range of values for the Chern numbers. This makes the sampling of the Chern number across the entire parameter space much more time-consuming than for model I. Therefore, the boundaries surrounding each phase are blurry as a result of the remaining numerical inaccuracy. For model II, the Chern number takes its values from  $\{\mathbb{N} \mid -24 \leq C \leq 12\}$ . Due to the symmetry present in the magnetic layer and the resulting double degenerate bands, the topological invariant can only take even values.

Furthermore, all phase transitions originated from gap closings at the high-symmetry points  $\Gamma$ , K and M in model I. This is no longer the case when the magnetic adatoms have electronic degrees of freedom of their own. For example, the phase with a Chern number of  $C = 12$  originates from a gap closing in the Brillouin zone along the line between  $\Gamma$  and K. For the purpose of illustrating this, the lowest-lying energy band  $E_k$  is depicted in Fig. 3.21 for the set of parameters marked by the black cross in Fig. 3.20 at the transition between the  $C = 12$ - and  $C = 0$ -phases.

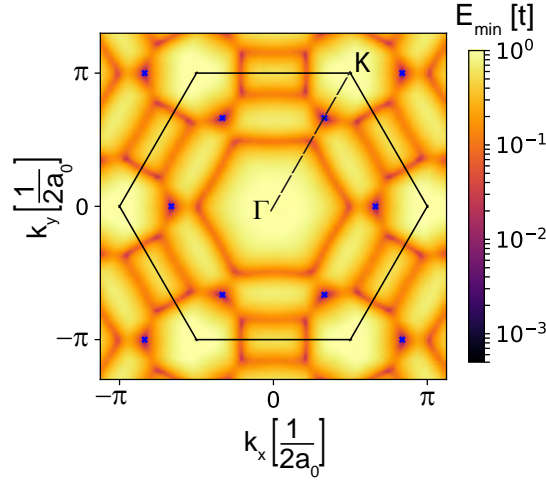


**Fig. 3.21:** Lowest-lying energy band  $E_k$  at  $(\mu, \Delta, JS) = (-0.681t, 0.4t, 1.0t)$  with the occurring gap closings away from high symmetry points marked by blue crosses and the reduced Brillouin zone marked by the black hexagonal.

The set of parameters, for which this phase transition occurs, was found through a minimization of this dispersion by varying  $\mu$  for a set magnetic exchange coupling  $J = 1.0t$ . The ideal value for the chemical potential is found to be  $\mu = -0.681t$ . The point on the line between  $\Gamma$  and K, where the gap closes, is marked by the blue crosses in Fig. 3.21. In the reduced Brillouin zone, which is marked by the

black hexagonal, lie six of these points. Combined with the double degeneracy of the bands, this renders the change in the Chern number of  $\Delta C = 12$  at this specific phase transition.

Another interesting property of model II is the possibility to tune the chemical potential of the superconducting layer  $\mu$  and the magnetic layer  $\mu_m$  to different values. Therefore, another phase diagram in dependence of  $\mu$  and  $\mu_m$  was calculated for a set value of the magnetic exchange coupling of  $J = 1.0t$  and two different values for  $t_{\text{hyb}} \in \{0.5t, 1.0t\}$ . The results for these two analyzed sets of parameters are depicted in Fig. 3.22 (a) and (b).

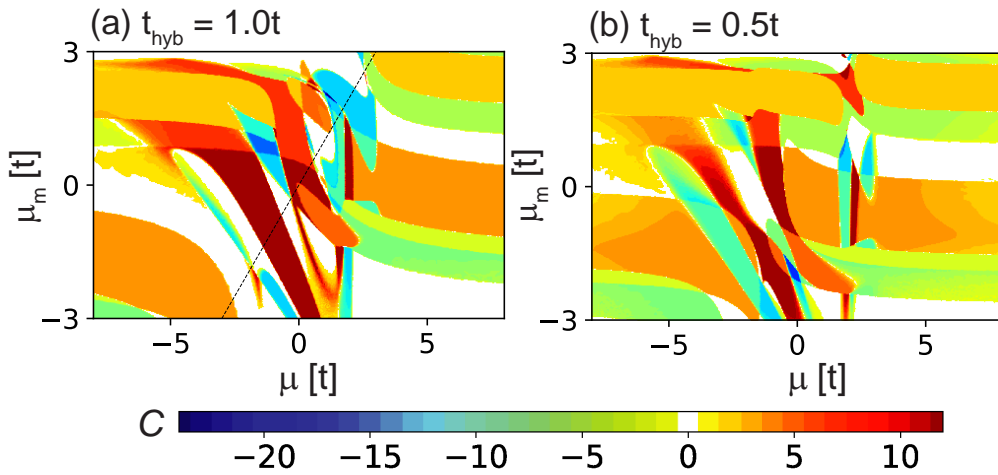


**Fig. 3.22:** Phase diagram for the AB-stacked spin structure with electronic degrees of freedom in dependence of  $\mu, \mu_m$  for two different values for the hopping parameter (a)  $t_{\text{hyb}} = 1.0t$ , (b)  $t_{\text{hyb}} = 0.5t$  with the black dashed line marking the shared parameter space with Fig. 3.20.

Here, it can be seen that differences in the two chemical potentials also have a great influence on the structure of the  $(\mu, J)$ -dependent phase diagram. The  $J = 1.0t$  line in Fig. 3.20 corresponds to the dashed diagonal line in Fig. 3.22 (a). The  $(\mu, \mu_m)$ -diagram also demonstrates that topological phases exist over a wide range of parameters and are thereby a robust phenomenon associated with the 3Q-structure. However, the large number of phases that occur in this phase diagram also has its disadvantages. Thereby, the number of required sampling points is much higher, which is the reason for the blurry phase boundaries and the erratic behaviour occurring around  $(\mu, JS) = (-5.0t, 0.5t)$ .

Another important thing to notice is that only trivial phases occur for large  $|\mu_m|$ . This is due to the fact that for  $|\mu_b| \approx 3.0t$ , the bands from the magnetic layer are

fully occupied and render non-topological phases.

Finally, Fig. 3.22 (b) shows that the topological character of the system is also robust for a weaker hybridization between the separate band structures of the two layers, which corresponds to a greater vertical distance between the two layers. This change in the set of parameters does not result in a change of the values of the Chern number, but instead shifts the formed phases already present in Fig. 3.22 (a) to overlap differently.

Overall, it can be concluded that the 3Q magnetic structure exhibits topological superconductivity for both model I and model II, when it is placed on a superconducting substrate. Model II especially shows that experiments employing this magnetic structure are prone to succeed, as it takes both the shift in the spatial positioning of the superconducting and magnetic layers as well as the electronic properties of the magnetic layer into account.

## 4 Magnetic Skyrmions

Magnetic skyrmions are stable, topological helical magnetic spin structures. In principle, a magnetic skyrmion is characterized by any spin structure, which can be mapped once to the sphere and whose center magnetization points in the other direction than its outward magnetization. Thereby, a number of possibilities arise for magnetic skyrmions, an example of which is shown in Fig. 4.1. The field of magnetic skyrmions has attracted a lot of research regarding their topological properties as their spin structure can be characterized by a winding number, their controlled creation and annihilation, as well as the applications of this spin structure [66].

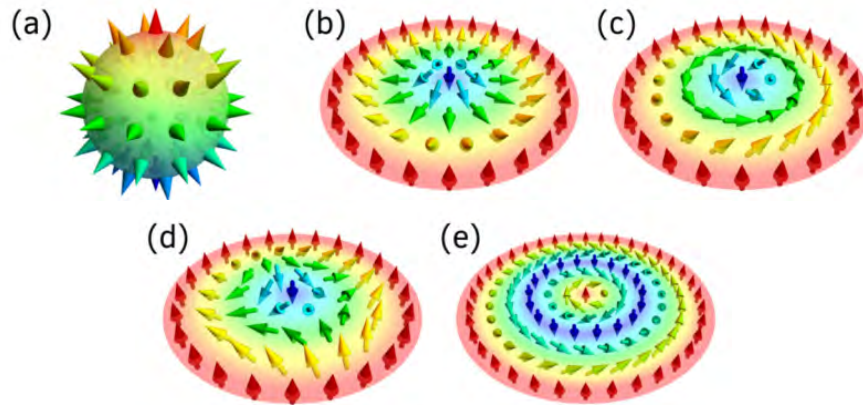


**Fig. 4.1:** Different spatial spin structures of magnetic skyrmions. (a) Hedgehog, (b) Néel-type skyrmion, (c) Bloch-type skyrmion, (d) Antiskyrmion and (e) Skyrmionium, [66].

Nowadays, single magnetic skyrmions can be written and deleted in a controlled fashion [67], which makes them a very attractive candidate for experimental realizations. Thereby, they are also a suitable candidate as a chosen spin structure in an MSH system. For this scenario, we have recently analyzed the topological properties [24], which showed that topological superconductivity not only emerges. Moreover, as the skyrmion radius can be tuned through external magnetic fields, this type of MSH structure enables the tuning through different topological phases at will. Here, the results for ribbon structures covered with magnetic skyrmions are discussed, as the spatial distribution of the computed supercurrents offers a unique way to distinguish

between topological and trivial phases.

## 4.1 Spin Structure

On a triangular lattice with  $N_1 \times N_2$  sites, the center of each skyrmion  $\mathbf{R}_{i,j}$  is defined as

$$\mathbf{R}_{i,j} = i d \mathbf{a}_1 + j d \mathbf{a}_2 + \mathbf{r}_0, \quad \text{with } 0 \leq i < M_1, 0 \leq j < M_2, i, j \in \mathbb{N}, \quad (4.1)$$

where  $\mathbf{r}_0$  defines an offset from the origin of the lattice, e.g. to create ribbon structures where no skyrmions are placed at the very edge of the lattice. Here, the radius  $R$  of a skyrmion is defined by the number of sites between a spin pointing straight up and a spin pointing straight down. Here, the skyrmion centers are placed so that two skyrmion centers are separated by the diameter  $d = 2R$  of the skyrmions. Therefore, the two skyrmions are at a minimal distance from one another.  $M_1$  and  $M_2$  correspond to the number of skyrmions in directions of  $\mathbf{a}_1$  and  $\mathbf{a}_2$ , respectively. For a completely covered ribbon, the previous parameters are chosen as  $\mathbf{r}_0 = \mathbf{0}$ ,  $M_1 = \frac{N_1}{d}$  and  $M_2 = \frac{N_2}{d}$ . We then determine the nearest skyrmion center for a chosen site  $\mathbf{r}$  by finding  $\min_{i,j} (|\mathbf{r} - \mathbf{R}_{i,j}|)$ . The spin orientation at this specific site [24] is then obtained from

$$\mathbf{S}_{\mathbf{r}} = \begin{pmatrix} \cos(\phi) \sin(\theta) \\ \sin(\phi) \sin(\theta) \\ \cos(\theta) \end{pmatrix} \quad (4.2)$$

with

$$\phi_{\mathbf{r}} = n \cdot \arctan \frac{\mathbf{r}'_x}{\mathbf{r}'_y} + \gamma \cdot \pi, \quad (4.3a)$$

$$\theta_{\mathbf{r}} = k \cdot \pi \cdot \tilde{r}, \quad (4.3b)$$

$$\tilde{r} = \min \left( \frac{|\mathbf{r}'|}{R}, 1 \right) \quad (4.3c)$$

and

$$\mathbf{r}' = \min_{i,j} (\mathbf{r} - \mathbf{R}_{i,j}). \quad (4.3d)$$

Here,  $k$  corresponds to the number of spatial rotations inside one skyrmion,  $\gamma$  is the helicity and  $n$  is the vorticity of the skyrmion. We investigate skyrmions with  $k = 1$ ,  $\gamma = 0$  and  $n = 1$ , which corresponds to skyrmions with one spatial rotation, which proceeds outwards without an added perpendicular helicity. Thereby, the skyrmions employed here correspond to panel (b) in Fig. 4.1, the Néel-type skyrmion. Fig. 4.2 illustrates a lattice covered with this type of skyrmion.

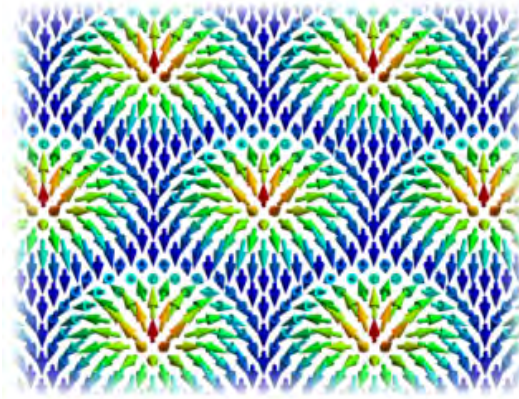


**Fig. 4.2:** Schematic plot of the spatial structure of a skyrmion lattice [24].

## 4.2 Phase Diagram

A lattice fully covered with skyrmions exhibits a wide variety of topological phases not only depending on the parameters in the Hamiltonian, but also on the chosen radius of the skyrmions. The topological phase diagram for different radii was discussed in [24], from where the phase diagram for  $R = 5$  and  $\Delta = 0.4t$  is shown in Fig. 4.3. The white areas that occur between topological phases here are a result of the numerical calculation and therefore are not meaningful in the interpretation.

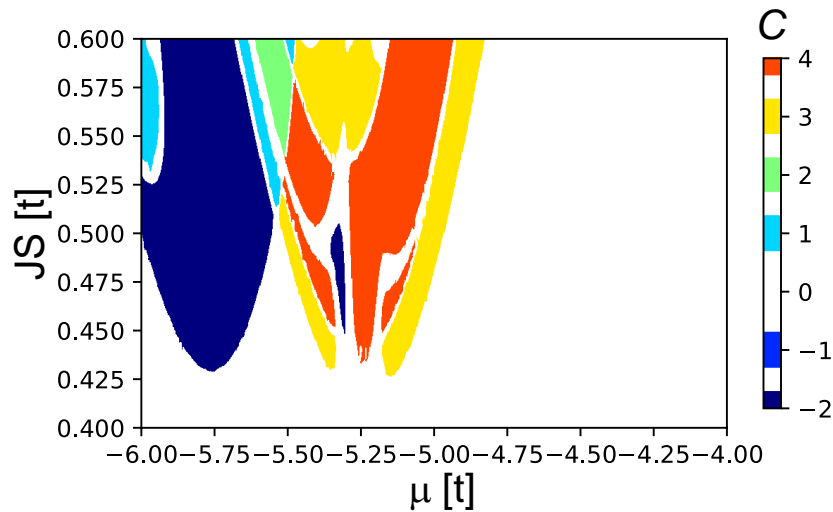


**Fig. 4.3:** Phase diagram for a skyrmion lattice with  $R = 5$  and  $\Delta = 0.4t$  [68].

In the following, the topological phase of  $C = 3$  at  $(\mu, \Delta, JS) = (-5.5t, 0.4t, 0.5t)$  is further investigated, as this set of parameters exhibits an especially strong edge current in the calculated supercurrents.

### 4.3 Edge Modes in Ribbon Structures

For a ribbon structure, a lattice of  $N_1 = 10$  sites and  $N_2 = 310$  sites is simulated for the computation of the band structure and the LDOS, where the direction of  $\mathbf{a}_1$  is chosen to be infinite and periodic boundary conditions are employed in the direction of  $\mathbf{a}_2$ . Therefore, the hoppings in this direction of the lattice are Fourier transformed analogously to the case of the 3Q structure. In this simulation, 27 skyrmions with radius  $R = 5$  were placed on the lattice. On both sides, 20 sites of the lattice remained uncovered by the spin structure, in order to create a boundary for the ribbon. The spatial structure of this ribbon is shown in Fig. 4.4 (a). In contrast, the supercurrents were calculated for a smaller ribbon of  $N_1 = 10$  and  $N_2 = 120$  with 10 skyrmions placed on the ribbon for reasons of visibility. Therein, 10 sites were left uncovered by the magnetic structure on either side of the ribbon.

#### 4.3.1 Band Structure

In order to calculate the band structure in dependence of the crystal momentum parallel to the ribbon, the Hamiltonian for the ribbon is diagonalized for  $n_k = 201$  equally distanced values of  $k_{\parallel} \in \left[-\frac{\pi}{N_1 a_0}, \frac{\pi}{N_1 a_0}\right)$ . The resulting band structure is shown in Fig. 4.4 (b). It exhibits six modes traversing the superconducting gap, which can thereby be recognized as Majorana modes. The chosen parameter set of  $(\mu, \Delta, JS) = (-5.0t, 0.4t, 0.5t)$  corresponds to a Chern number of  $C = 3$ , this number of Majorana modes matches the expected number, which is given by the number of edges times the difference in the Chern number across one edge due to the bulk-boundary correspondence.

#### 4.3.2 Local Density of States

From the eigenenergies and eigenstates of the diagonalized Hamiltonian, the local density of states at zero energy can once again be calculated on the ribbon. The result, shown in Fig. 4.4 (c) and (d), demonstrates that the LDOS is localized once again on the boundary of the ribbon. However, unlike for the 3Q structure, this result shows local minima at each skyrmion center with the maxima wrapping around the centers for the two rows of skyrmions placed closest to the edge of the magnetic

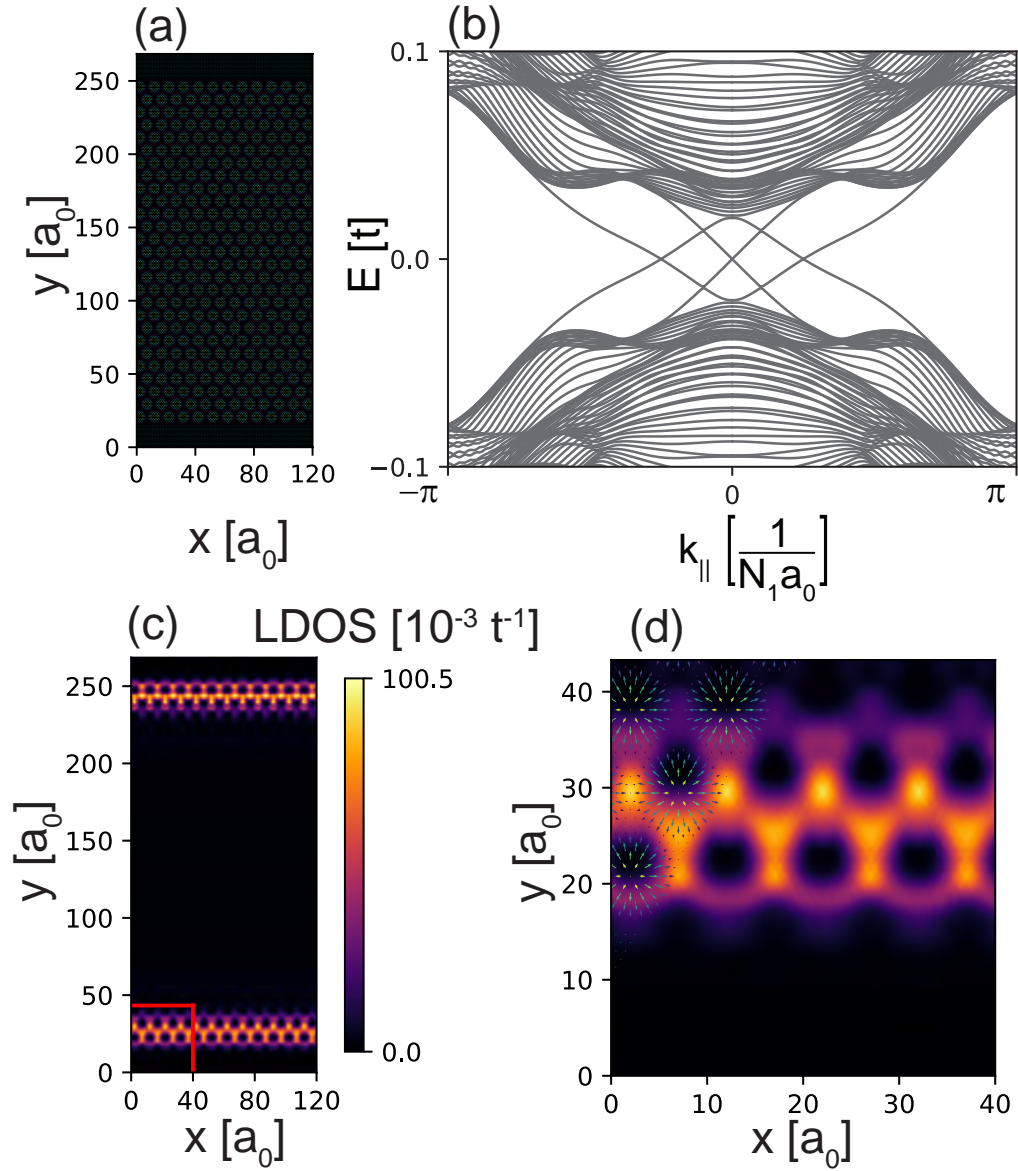


**Fig. 4.4:** (a) Spatial structure of the investigated ribbon, (b) dispersion in dependence of the crystal momentum  $k_{||}$ , (c) LDOS at zero energy with the inset shown in (d) marked by the red rectangle, where the spin structure of the skyrmions is also shown.

ribbon. This illustrates the existence of zero-energy Majorana modes on the edges of the skyrmion ribbon. This is illustrated in the inset from Fig. 4.4 (d) at the lower edge of the ribbon, where the spatial structure of the magnetic skyrmion lattice is shown at the same time.

### 4.3.3 Supercurrents

Finally, the total supercurrent was calculated for this magnetic structure, as explained in section 2.5. In Fig. 4.5, the parameter set  $(\mu, \Delta, JS) = (-5.5t, 0.4t, 0.5t)$  was considered. For these parameters, the system is in a topological phase of Chern number  $C = 3$ . As for the 3Q structure, a strong current localized on the edge of the magnetic ribbon can be observed, as can be seen in the enlarged plot in Fig. 4.5 (b).

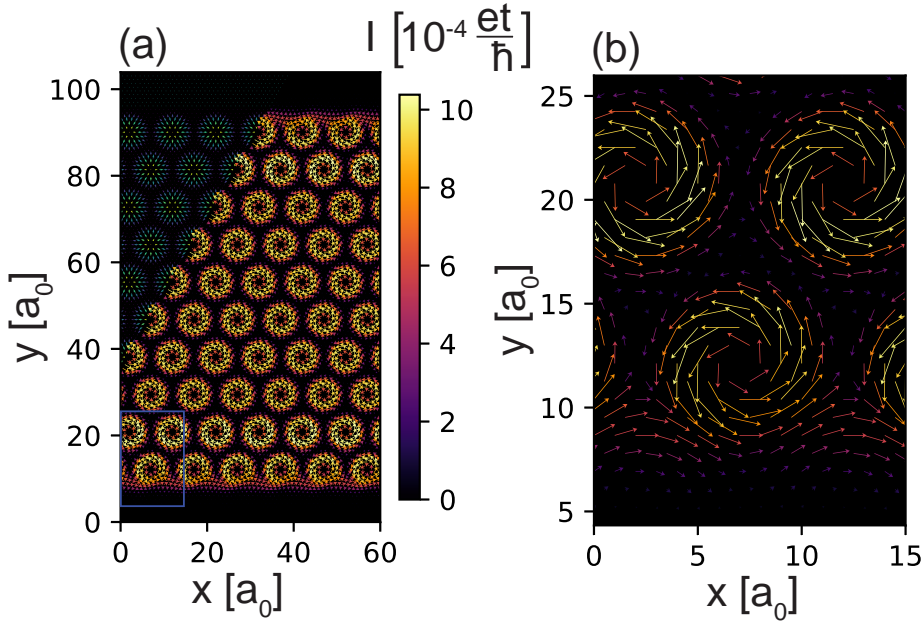


**Fig. 4.5:** Supercurrent for the topological phase of  $C = 3$  at  $(\mu, \Delta, JS) = (-5.5t, 0.4t, 0.5t)$  (a) across the entire simulated ribbon with the spin structure shown in the upper left corner and (b) for the region marked by the blue rectangle in (a).

Here, the region marked by the blue rectangle in Fig. 4.5 (a) is shown. However, the current also forms vortices around each center of a skyrmion, whereas no current emerges in the regions between two magnetic skyrmions where the spins all point

uniformly downwards. This formation of vortices around each skyrmion core is illustrated in Fig. 4.5 (a) by showing the spin structure simultaneously to the simulated currents, so that the location of the vortices relative to the spin structure is clear.

In comparison to the case of a topological phase, the supercurrent was also simulated for the trivial phase at  $(\mu, \Delta, JS) = (-5.5t, 0.4t, 0.2t)$ . This scenario is depicted in Fig. 4.6 (a) across the entire simulated ribbon.

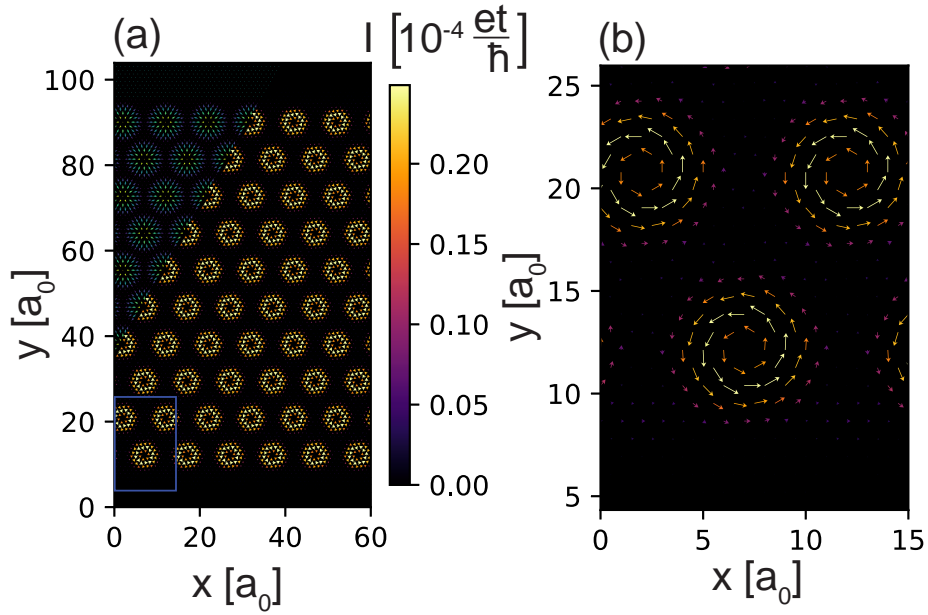


**Fig. 4.6:** Supercurrent for the trivial phase of  $C = 0$  at  $(\mu, \Delta, JS) = (-5.5t, 0.4t, 0.2t)$  (a) across the entire simulated ribbon with the spin structure shown in the upper left corner and (b) for the region marked by the blue rectangle in (a).

The result exhibits a supercurrent which is smaller by a factor of approximately 40, showing that in the trivial phase the supercurrent is much smaller. The vortices forming here do not extend further than the magnetic skyrmion, around which they form. This is illustrated by showing the spin structure and the calculated supercurrents simultaneously in Fig. 4.6 (a). Furthermore, no edge current can be observed, as illustrated by the enlarged plot in Fig. 4.6 (b). This region is marked in Fig. 4.6 (a) by the blue rectangle. Therefore, if the supercurrent would be averaged through e.g. a Gaussian filter that averages the contributions from close-lying sites, this would result in only the edge currents remaining and the vortices within the

ribbon evening out for the topological phase. For the trivial phase on the other hand, the vortices would cancel out completely, so no currents would be observed then.

This assessment is important for an experimental approach to the measurement of supercurrents. For this kind of measurement, the magnetic field induced by the supercurrent would be measured using superconducting quantum interference devices (SQUIDS) and as the relative distance between neighboring sites is very small, the SQUID could only detect the averaged field induced by a number of sites. Thereby, the edge currents from the topological phase could be detected, but most likely no current would be detected for the trivial phase.

## 5 Domain Walls

Recently, dispersing Majorana modes have been observed at a domain wall in the topological superconductor  $\text{FeSe}_{0.45}\text{Te}_{0.55}$  [22]. To address the question, which types of domain walls result in the emergence of Majorana modes, three types of domain walls will be investigated which are introduced in a 3Q-ordered magnetic layer on a superconducting substrate. These domain walls are created by sudden spatial shifts in the spin structure, inversions of the spin structure and  $\pi$ -phase shifts in the superconducting order parameter.

For the 3Q-ordered spin structure, a magnetic ribbon is investigated, which is infinite in direction of  $\mathbf{a}_1$  and has periodic boundaries applied in direction of  $\mathbf{a}_2$ . Due to the infinite number of sites in direction of  $\mathbf{a}_1$ , this direction is once again Fourier transformed, as previously discussed in section 3.5.2. We then create two domains by covering the lower half in direction of  $\mathbf{a}_2$  of the ribbon with the first type of domain, and the upper half of the ribbon with the second type of domain. Thereby, one domain wall occurs at  $y = \frac{3}{4}N_2a_0$  and a second domain wall at  $y = 0$  due to the periodic boundary conditions. As this spin structure is placed on a triangular lattice, two unique spatial shifts can be considered. The first shift consists of shifting the spin structure by the lattice vector  $\mathbf{a}_1$ , which is thus parallel to the infinite direction of the ribbon. The second shift consists of shifting the spin structure by  $\mathbf{a}_2$ .

For comparison, a lattice fully-covered with the 3Q structure with infinite sites in direction of  $\mathbf{a}_1$  and  $N_2 = 120$  is simulated for  $(\mu, \Delta, JS) = (-1.0t, 0.4t, 1.0t)$  corresponding to a Chern number of  $C = 4$ . For the purpose of calculating the band structure in dependence of  $k_{\parallel}$ , this lattice is also Fourier transformed in direction of  $\mathbf{a}_1$ , as described in section 3.5.2. For the resulting band structure shown in Fig. 5.1, the domain of the crystal momentum parallel to the infinite direction  $k_{\parallel} \in \left[-\frac{\pi}{2a_0}, \frac{\pi}{2a_0}\right)$  is split into  $n_k = 700$  equidistant points.

Due to the fact that the lattice is fully covered with spins and that there are no domain walls introduced, no boundaries are present. Therefore, the bulk-boundary correspondence does not apply, yielding only bulk bands in the band structure. This set of parameters will be applied for all of the following types of domain walls.

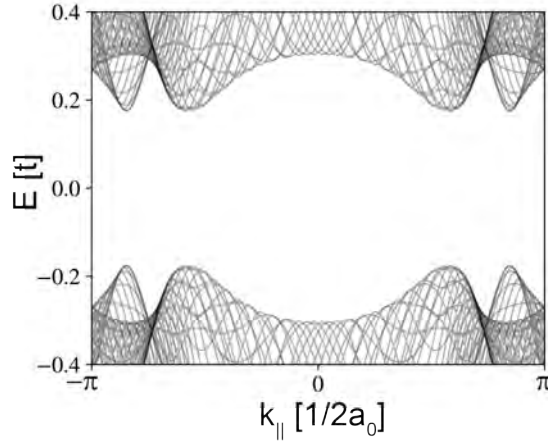


**Fig. 5.1:** Dispersion in dependence of the crystal momentum  $k_{||}$  parallel to the ribbon for a lattice fully-covered with 3Q-ordered spins.

## 5.1 Domain Walls Created from Shifts of the Spin Structure

The first possibility for a domain wall investigated here is created by a shift in the spin structure at  $y = \frac{3}{4}N_2a_0$  along  $\mathbf{a}_1$ . This action corresponds to switching  $\mathbf{S}_0$  and  $\mathbf{S}_1$  as well as  $\mathbf{S}_2$  and  $\mathbf{S}_3$  in the unit cell of the second domain. For this ribbon, the band structure is then calculated in dependence of the crystal momentum parallel to the ribbon. The result is shown in Fig. 5.2 (a), exhibiting a similar band structure as Fig. 5.1. Apart from four bands that are slightly lowered into the gap, no modes can be observed that are not associated with the bulk states and no crossings are generated. It can therefore be concluded that placing a domain wall, where the spin structure is shifted by  $\mathbf{a}_1$ , does not generate any Majorana modes in the case of the 3Q structure. This result can be expected since a shift in the spin structure does not produce a change in the Chern number.

The second domain wall of this type is created by applying a spatial shift by  $\mathbf{a}_2$  of the spin structure at  $y = \frac{3}{4}N_2a_0$ . Accordingly, the spins  $\mathbf{S}_0$  and  $\mathbf{S}_2$  as well as  $\mathbf{S}_1$  and  $\mathbf{S}_3$  are switched in the unit cell of the second domain in the upper half of the ribbon. Thereby, the Chern number has the same value in the first and the second domain.

Fig. 5.2 (b) exhibits the calculated band structure for this scenario. The dispersion shows four bands that are moved significantly into the superconducting gap. Despite the fact that these are close to reaching the energy level of zero, these modes still do not traverse the gap and thereby distinguish themselves from Majorana modes. Therefore, this shift in the spin structure does not result in the occurrence of edge modes either.

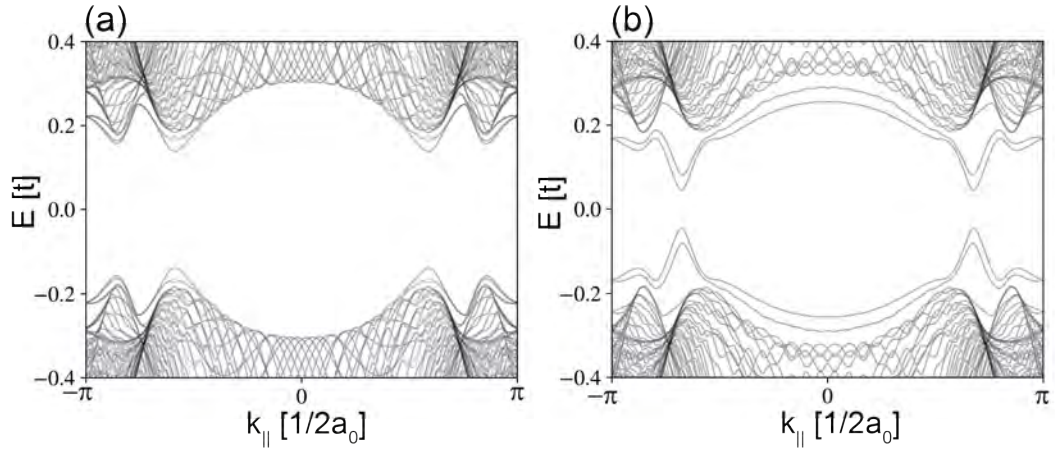


**Fig. 5.2:** Dispersion in dependence of the crystal momentum  $k_{\parallel}$  parallel to the ribbon for a domain wall with a shift in the spin structure (a) in the direction of  $\mathbf{a}_1$  and (b) in the direction of  $\mathbf{a}_2$ .

## 5.2 Domain with an Inverted Spin Structure

The second type of domain wall, which is to be investigated here, is introduced by inverting the spin structure from the first domain to the second. By calculating the Chern number for the inverted spin structure using (2.4), it is found that this inversion of the spins  $\mathbf{S}_{\mathbf{r}} \rightarrow -\mathbf{S}_{\mathbf{r}}$  also results in the opposite sign for the Chern number  $C \rightarrow -C$ . Therefore,  $2|C|$  modes are expected at each of the domain walls between the two domains due to the bulk-boundary correspondence. Fig. 5.3 (a) demonstrates the spin structure close to the domain wall in the middle of the ribbon, where the red shading marks the lower domain with the original spin structure, and the blue shading marks the upper domain with the inverted spin structure.

For a ribbon with  $N_1 = 2$  and  $N_2 = 280$  sites and  $n_k = 700$  points for the equidistant sampling of the crystal momentum  $k_{\parallel} \in \left[-\frac{\pi}{2a_0}, \frac{\pi}{2a_0}\right)$ , the Hamiltonian was diagonalized for each sampling point of  $k_{\parallel}$ . The resulting band structure is depicted in Fig. 5.3 (b). The bands are symmetric around  $k_{\parallel} = 0$  and show eight modes traversing the superconducting gap on either side of  $k_{\parallel} = 0$ . These are marked in red on the right side of the band structure, with the right-moving modes with  $\frac{\partial E}{\partial k_{\parallel}}$  marked by solid lines and the left-movers marked by dashed lines. Therefore, an overall number of sixteen Majorana modes is observed. This matches the expected eight modes at each of the two domain walls, as there is a change of  $|\Delta C| = 8$  across each domain wall due to the Chern number of  $C = 4$  of the analyzed phase for the original 3Q magnetic spin structure and  $C = -4$  for the inverted spin structure.

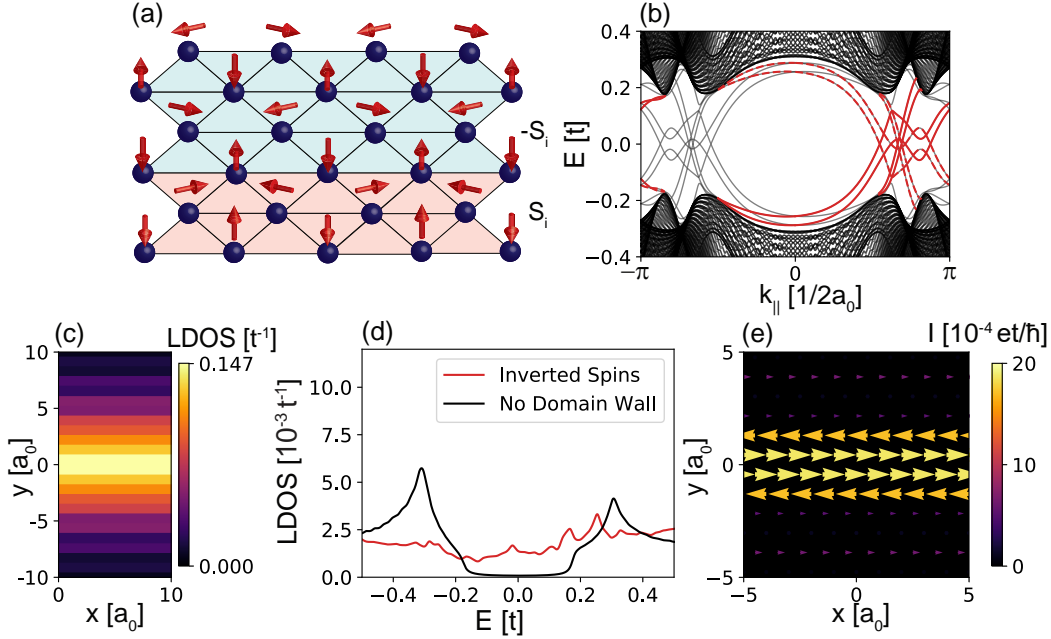


**Fig. 5.3:** (a) Spin structure, (b) dispersion in dependence of  $k_{\parallel}$ , the crystal momentum parallel to the ribbon, (c) zero-energy LDOS on the ribbon close to the domain wall, (d) energy-dependent LDOS at the domain wall (red) and at  $y = N_2 \frac{\sqrt{3}}{2}$  for a fully-covered lattice (black) and (e) supercurrent at the domain wall.

Next, the zero-energy LDOS was calculated from the diagonalized Hamiltonian. In Fig. 5.3 (c), the result for the region of the ribbon around  $-10a_0 \leq y - \frac{\sqrt{3}}{4}N_2 \leq 10a_0$  is depicted, in order to analyze the region in close proximity to the domain wall in the middle of the ribbon. This panel shows a strong localization at the domain wall, as is to be expected for the emerging Majorana modes. Panel (d) shows the energy-resolved LDOS at the domain wall compared to the result for the same site in the middle of the system without domain walls from Fig. 5.1. The result at a site for the system without domain walls, which corresponds to the black line, matches the expectation for a bulk state, as it exhibits the superconducting gap in the interval  $[-0.3, 0.3]$  lined with two coherence peaks. The black line leaks into the gap width due to numerical inaccuracies. These stem from the finite size of the analyzed ribbon and the fact that a finite value had to be chosen for  $\delta$  in Eq. (2.8a), in order to numerically approximate the  $\delta$ -distribution. In comparison, the result at the domain wall, which is shown as the red line, shows an almost constant energy-resolved LDOS.

Finally, panel (e) in Fig. 5.3 shows the supercurrent on both sides of the domain

wall for the region  $-5a_0 \leq y - \frac{\sqrt{3}}{4}N_2a_0 \leq 5a_0$ . Here, it can be observed that the supercurrent is symmetric around the domain wall and also highly localized, as it only contributes strongly for four unique rows. On the two opposite sides of the domain wall, the current has the opposite chirality which is related to the sign of the Chern number. Thereby, the currents on both sides of the domain wall flow in the same direction, thus rendering a non-vanishing current when these contributions are summed over.

### 5.3 Domain with an Inverted Superconducting Order Parameter

The final domain wall that is investigated here is constructed by changing the phase of the superconducting order parameter by  $\pi$  between the two domains. Thereby, two domains with the same spin structure and respectively inverted superconducting order parameters meet at the two domain walls at the beginning and the middle of the ribbon. The spatial appearance of the domain wall in the middle of the ribbon is illustrated in panel (a) of Fig. 5.3. It is important to note that by calculating the Chern number for both  $\Delta$  and  $-\Delta$ , it can be seen that the Chern number is independent of the sign of the superconducting order parameter. This stems from the fact that the Hamiltonian investigated here is  $U(1)$  invariant, which is a continuous symmetry. Thereby, the Chern number does not depend on the phase of the superconducting order parameter.

Firstly, the band structure was calculated for a lattice of  $N_1 = 2$  and  $N_2 = 280$  sites in dependence of the crystal momentum  $k_{\parallel} \in \left[-\frac{\pi}{2a_0}, \frac{\pi}{2a_0}\right)$ , whose domain of definition is discretized into  $n_k = 700$  equidistant points. The resulting dispersions are shown in Fig. 5.4 (b). Here, four modes enter the superconducting gap, which are doubly-degenerate, and thereby constitute possible candidates for Majorana modes. In order to check whether these modes traverse the superconducting gap, the dispersion of one of the four was traced. The second one has the same dispersion and the other two have the same dispersion with a negative energy instead of a positive one, so that the tracing of one of the modes suffices. As the corresponding normalized eigenvectors  $|E_n(k_{\parallel})\rangle$  to one momentum-resolved eigenenergy  $E_n(k_{\parallel})$  are orthonormal

$$\langle E_m(k_{\parallel}) | E_n(k_{\parallel}) \rangle = \delta_{nm} , \quad (5.1)$$

the scalar product of two eigenvectors to the same eigenenergy with slightly different crystal momenta should still be approximately equal to unity

$$\langle E_n(k_{\parallel}) | E_n(k_{\parallel} + \delta k_{\parallel}) \rangle = 1 + \mathcal{O}(\delta k_{\parallel}) . \quad (5.2)$$

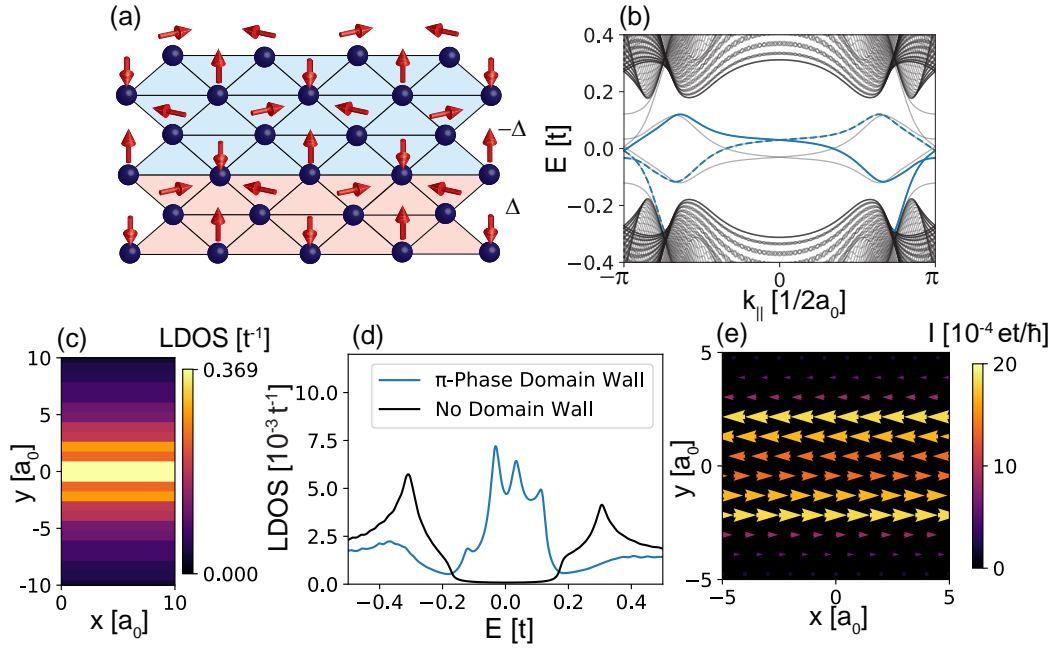


**Fig. 5.4:** (a) Spin structure, (b) dispersion in dependence of  $k_{\parallel}$ , the crystal momentum parallel to the ribbon, (c) zero-energy LDOS on the ribbon close to the domain wall, (d) energy-dependent LDOS at the domain wall (blue) and at  $y = N_2 \frac{\sqrt{3}}{2}$  for a fully-covered lattice (black) and (e) supercurrent at the domain wall.

This allows us to trace the in-gap modes despite the various mode crossings occurring. In doing so, it can be seen that the analyzed mode, which is marked by the blue line in Fig. 5.4 (b), originates from the lower bulk and disperses across the entire Brillouin zone for  $k_{\parallel}$ . Then, it crosses over the Brillouin zone another time and finally reaches the lower bulk again, which is marked by a dashed blue line for reasons of visibility. From this tracing of the eigenmode, it can be concluded that the four modes entering the superconducting gap for this type of domain wall are not Majorana modes, as they do not connect the upper and lower bands, and are thus trivial modes.

Experimentally, Majorana modes are often analyzed by measuring the local density of states at zero energy using scanning tunneling spectroscopy. A simulation of this zero-energy LDOS is depicted in Fig. 5.4 (c) and shows the region  $-10a_0 \leq y - \frac{\sqrt{3}}{4}N_2 \leq 10a_0$  of the ribbon. Despite the conclusion that the observed modes inside the gap are trivial, there is still a localized peak in the LDOS at the location of the domain wall. Therefore, this type of domain wall can not be experimentally distinguished from for example Fig. 5.3 (c), where topological modes are present. The energy-resolved LDOS at the domain wall from Fig. 5.4 (d) also shows that

the spectral weight of the trivial modes is very high inside the superconducting gap, which is marked by the blue line in this panel. Compared to the black line, which presents the energy-resolved LDOS in the middle of the fully-covered lattice for the system without domain walls, the spectral weight at the domain wall is much smaller outside the superconducting gap.

Finally, Fig. 5.4 (e) demonstrates the supercurrent close to the domain wall for  $-5a_0 \leq y - \frac{\sqrt{3}}{4}N_2a_0 \leq 5a_0$ . Compared to Fig. 5.3 (e), the current is not only spread out further, it also reverses its direction at the domain wall, which is marked by  $y = 0$  in this panel. As the chirality of the current is linked to the sign of the Chern number, this explains that the current reverses its direction at the domain wall, because it has the same chirality in both of the domains. Therefore, the two currents from the separate domains cancel at the domain wall, when they are summed over. This is important from an experimental point of view, as the supercurrent would be measured via a SQUID through the induced magnetic field, which sums the contributions, as the sites are in close proximity. Thus, no current would be measured for this domain wall, where the order parameter was abruptly inverted. In contrast, for two domains with respectively inverted spin structures, the SQUID would detect a finite magnetic field induced by the supercurrent. Thereby, the supercurrent can be employed as a means to distinguish between the trivial and topological modes induced by these two types of domain walls.

## 6 Non-Equilibrium Magnetic Perturbations

An essential step in the path towards topological quantum computing is the realization of Clifford gates [69]. As both the quantum engineering of complex systems as well as the experimental methods to analyze these have made significant advances, real time processes at the nanoscale can be investigated nowadays, which is crucial for the creation of Clifford gates. One proposal [30] to realize them is based on the Majorana zero modes located in vortex cores of topological superconductors [27–29]. The MZMs in vortex cores have also been found experimentally in the static case [20, 21].

By moving these vortices in space, the braiding operations needed for Clifford gates can be realized. The theoretical investigation of such braiding operations require the use of the full Keldysh non-equilibrium Green’s function formalism [70] in real time. As a first step in realizing this project, we study the effect of time dependent perturbations in metallic and superconducting systems. Therein, the moving vortex is modelled as an applied perturbation to a lattice site. Based on the results here, the objective is to further develop the employed methods, so that they can be used as guidance in current experimental efforts [71], where vortex core MZMs in topological superconductors are braided.

### 6.1 Metallic System

For a metallic system, the objective is to calculate the time dependent current between a metallic lattice site and a metallic STS tip, after a perturbation is applied to the lattice site. Here, a bias voltage  $V_{\text{Bias}}$  is applied between the two interacting parts and a tunneling amplitude  $t_{\text{tun}}$  allows hopping between them. A sketch of this system is shown in Fig. 6.1.

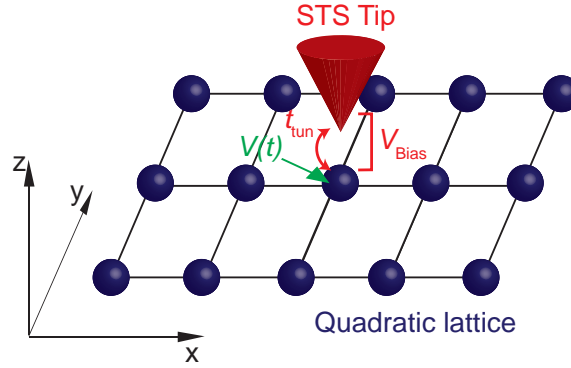


**Fig. 6.1:** Schematic depiction of the investigated system: A STS tip measures the current from a singular lattice site, to which a time dependent perturbation is applied. The site is part of a quadratic lattice. Between the lattice site and the STS tip, a bias voltage  $V_{\text{Bias}}$  is applied and a tunneling amplitude  $t_{\text{tun}}$  is present.

### 6.1.1 Theoretical Method

The Hamiltonian for the quadratic lattice depicted in Fig. 6.1, reads

$$\mathcal{H} = \sum_{\mathbf{k}, \sigma} \epsilon_{\mathbf{k}} c_{\mathbf{k}, \sigma}^{\dagger} c_{\mathbf{k}, \sigma} \quad (6.1a)$$

with the dispersion

$$\epsilon_{\mathbf{k}} = -2t_m[\cos(k_x) + \cos(k_y)] - \mu. \quad (6.1b)$$

Here,  $k_x$  and  $k_y$  are the crystal momenta in directions of  $x$  and  $y$  in the Brillouin zone,  $t_m$  refers to the hopping parameter in the metallic system and  $\mu$  is the chemical potential.

From this diagonalized Hamiltonian, the momentum-resolved, energy dependent retarded Green's function of the isolated system can be obtained analytically as

$$g_{ss}^R(k, \omega) = \frac{1}{\omega - \epsilon_{\mathbf{k}} + i\delta}. \quad (6.2)$$

where the double index  $ss$  denotes that this Green's function refers solely to the lattice. Here, the term isolated refers to the fact that this Green's function is the result for the case where the lattice does not interact with the STS tip in any way. In the following, lower case letters will be employed for the Green's functions referring

to this uncoupled state. In contrast, all Green's functions, referring to the coupled system of the perturbed site and the measuring tip, will be denoted by upper case letters.

In the following, only one metallic site is considered. Therefore, a Fourier transformation is applied to  $g_{ss}^R(k, \omega)$  as

$$g_{ss}^R(\mathbf{r} = 0, \omega) = \int \frac{d^2k}{(2\pi)^2} g_{ss}^R(k, \omega). \quad (6.3)$$

For the tip in the uncoupled state, we assume the same uncoupled Green's function, such that  $g_{ss}^R(\omega) = g_{tt}^R(\omega)$ . The respective advanced Green's functions are obtained by replacing  $+i\delta \rightarrow -i\delta$ .

Then, the two isolated states of the lattice site and the STS tip need to be coupled, in order to arrive at the Green's functions, that describe the complete system investigated here. The full matrix of coupled Green's functions [16] is derived from

$$\hat{G}_0^R(\omega) = \begin{pmatrix} G_{0,tt}^R(\omega) & G_{0,ts}^R(\omega) \\ G_{0,st}^R(\omega) & G_{0,ss}^R(\omega) \end{pmatrix} = [(\hat{g}^R)^{-1} - \hat{t}]^{-1}, \quad (6.4)$$

where  $\hat{t}$  characterizes the hopping between the tip and the metallic site through the matrix

$$\hat{t} = -t_{\text{tun}} \begin{pmatrix} 0 & 1 \\ 1 & 0 \end{pmatrix}. \quad (6.5)$$

In Eq. (6.4), a combined matrix for the uncoupled Green's functions

$$\hat{g}^R(\omega) = \begin{pmatrix} g_{tt}^R(\omega) & 0 \\ 0 & g_{ss}^R(\omega) \end{pmatrix} \quad (6.6)$$

was also defined, which is diagonal as it describes the uncoupled case.

For the calculation of the current, the lesser Green's function is required. In the uncoupled state, it is given by

$$\hat{g}^< = \begin{pmatrix} -2i n_F^t(\omega) \text{Im} g_{tt}^R(\omega) & 0 \\ 0 & -2i n_F^s(\omega) \text{Im} g_{ss}^R(\omega) \end{pmatrix}. \quad (6.7)$$

Here, it can be seen that the uncoupled lesser Green's function corresponds to the imaginary part of the retarded Green's function, with a Fermi-Dirac distribution applied to it. This Fermi-Dirac distribution has different Fermi energy levels set for

the tip and the metallic site respectively, which is denoted by the index t or s in Eq. (6.7). These two versions of the Fermi-Dirac distribution are given by

$$n_{\text{F}}^{\text{t}}(\omega) = \frac{1}{\exp[-\beta(\omega - eV_{\text{Bias}})] + 1} \quad (6.8)$$

$$n_{\text{F}}^{\text{s}}(\omega) = \frac{1}{\exp[-\beta\omega] + 1}, \quad (6.9)$$

where it can be seen that the Fermi energy is higher by  $eV_{\text{Bias}}$ , the energy difference introduced by the bias voltage, for the Fermi-Dirac distribution referring to the tip.

Finally, the coupled, lesser Green's function is computed from the uncoupled one through the formula [16]

$$\hat{G}_0^<(\omega) = [\hat{1} - \hat{g}^R \hat{t}]^{-1} \hat{g}^< [\hat{1} - \hat{t} \hat{g}^A]^{-1}. \quad (6.10)$$

For the calculation, the time dependent unperturbed Green's function is required, which is derived from the Green's function in the frequency domain by a Fourier transformation

$$\hat{G}_0^<(t, t') = \hat{G}_0^<(t - t') = \int \frac{d\omega}{2\pi} \hat{G}_0^<(\omega) e^{i\omega(t-t')}. \quad (6.11)$$

Then, in order to calculate the time dependence of the induced current between the lattice site and the STS tip, the time dependent lesser Green's function of the coupled lattice site and the STS tip has to be calculated. As a magnetic perturbation is applied to the coupled system, the perturbed lesser Green's function  $\hat{G}^<(t, t')$  at times  $t$  and  $t'$  is determined from the Dyson equation [72, 73]

$$\begin{aligned} \hat{G}^<(t, t') &= \hat{G}_0^<(t, t') + \int dt_1 \hat{G}_0^R(t, t_1) \hat{V}(t_1) \hat{G}^<(t_1, t') \\ &+ \int dt_1 \hat{G}_0^<(t, t_1) \hat{V}(t_1) \hat{G}^A(t_1, t'). \end{aligned} \quad (6.12)$$

Here,  $\hat{G}_0^{R,<,A}(t, t_1)$  refer to the retarded, lesser and advanced Green's function of the coupled system of the lattice site and the STS tip, to which the perturbation  $\hat{V}(t_1, t_1)$  is not applied. Note that all Green's functions that were included so far are matrices. As we look at the coupled system of the metallic site and the STS tip, this matrix consists of four separate Green's functions, as given by

$$\hat{G}_0^<(t, t') = \begin{pmatrix} G_{0,\text{tt}}^<(t, t') & G_{0,\text{ts}}^<(t, t') \\ G_{0,\text{st}}^<(t, t') & G_{0,\text{ss}}^<(t, t') \end{pmatrix} \quad (6.13)$$

and

$$\hat{G}^<(t, t') = \begin{pmatrix} G_{tt}^<(t, t') & G_{ts}^<(t, t') \\ G_{st}^<(t, t') & G_{ss}^<(t, t') \end{pmatrix}, \quad (6.14)$$

where we listed all components of  $\hat{G}_0^<(t, t')$  and  $\hat{G}^<(t, t')$ .  $\hat{G}_{R,A}^<(t, t')$  have analogous structures. The indices  $t$  and  $s$  indicate the parts of the Green's function referring to the STS tip and the system site, respectively. In the case investigated here, the perturbation  $\hat{V}(t_1)$  in the Dyson equation, which occurs at the time  $t_1$ , is only applied to the metallic site and thereby takes the form

$$\hat{V}(t_1) = \begin{pmatrix} 0 & 0 \\ 0 & V(t_1) \end{pmatrix}, \quad (6.15)$$

where  $V(t_1)$  is a function describing the form of the perturbation. The induced tunneling current [74] between the metallic site and the STS tip is then given by

$$I(t) = \frac{e}{\hbar} (-t_{\text{tun}}) [G_{ts}^<(t, t) - G_{st}^<(t, t)]. \quad (6.16)$$

Inserting (6.12) into this equation, yields

$$\begin{aligned} I(t) = & \frac{e}{\hbar} (-t_{\text{tun}}) \{ G_{0,ts}^<(t, t) - G_{0,st}^<(t, t) \\ & + \int dt_1 [G_{0,ts}^R(t, t_1)V(t_1)G_{0,ss}^<(t_1, t) + G_{0,ts}^<(t, t_1)V(t_1)G_{0,ss}^A(t_1, t)] \\ & - \int dt_1 [G_{0,ss}^R(t, t_1)V(t_1)G_{0,st}^<(t_1, t) + G_{0,ss}^<(t, t_1)V(t_1)G_{0,st}^A(t_1, t)] \}, \end{aligned} \quad (6.17)$$

where we only took contributions of the first order in the perturbation into account, which is justified for small values of  $J$ . In this case  $\hat{G}^{R,<,A}(t_1, t')$  is simply replaced by  $\hat{G}_0^{R,<,A}(t_1, t')$  in Eq. (6.12). Finally, we determine the exact formula to calculate the current for the special case of a  $\delta$ -pulse perturbation at the point of time  $t_0$ , which is given through

$$V(t_1) = V_0 \delta(t_1 - t_0). \quad (6.18)$$

Including this form for  $V(t_1)$  into Eq. (6.17) yields the final formula

$$I(t) = I_0 + \delta I(t) \quad (6.19)$$

with

$$I_0 = \frac{e}{\hbar} (-t_{\text{tun}}) [G_{0,ts}^<(t, t) - G_{0,st}^<(t, t)], \quad (6.20a)$$

and

$$\begin{aligned} \delta I(t_0 + \Delta t) = & \frac{e}{\hbar} (-t_{\text{tun}}) V_0 [G_{0,ts}^r(\Delta t)G_{0,ss}^<(-\Delta t) + G_{0,ts}^<(\Delta t)G_{0,ss}^a(-\Delta t) \\ & - G_{0,ss}^r(\Delta t)G_{0,st}^<(-\Delta t) - G_{0,ss}^<(\Delta t)G_{0,st}^a(-\Delta t)] \end{aligned} \quad (6.20b)$$

Here, we introduced  $\Delta t = t - t_0$  as the time interval between the perturbation at  $t_0$  and the time of observation  $t$ .

### 6.1.2 Result for the Induced Current

With the methods introduced in the preceding section, the induced current between the metallic site and the STS tip can now be calculated in first order approximation. As the result is strongly dependent on the chosen value of the bias voltage  $V_{\text{Bias}}$ , the current was calculated for 361 equidistant points across the entire band width  $eV_{\text{Bias}} \in [-4t - \mu, 4t - \mu]$  for  $V_0 = 1.2t_m$ . The resulting current is shown for the three values  $V_{\text{Bias}} = [-0.5t_m, 1.4t_m, 3.5t_m]$  in Fig. 6.2.

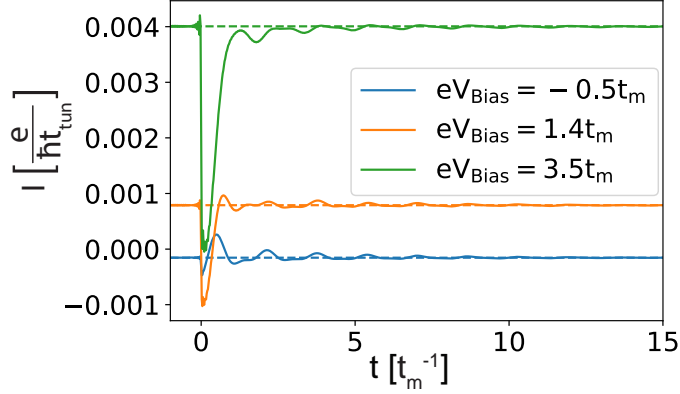


**Fig. 6.2:** Result for the time dependent current  $I(t)$  for  $V_{\text{Bias}} = [-0.5t_m, 1.4t_m, 3.5t_m]$  for corrections in first order. The dashed lines show the constant current determined for the system in equilibrium.

It can be seen here that the current oscillates from the time of perturbation at  $t = 0$  and slowly approaches the constant value of the unperturbed system in equilibrium again. The amplitude of the oscillation is strongest for  $V_{\text{Bias}} = 3.5t_m$  out of the three values shown here and decreases with  $V_{\text{Bias}}$ . Another interesting quantity to consider is  $\frac{dI}{dV_{\text{Bias}}}(V_{\text{Bias}}, t)$ , as it is proportional to the density of states in the case of an unperturbed system  $\frac{dI_0}{dV_{\text{Bias}}} \sim N(V_{\text{Bias}})$ . The result for this quantity is depicted in Fig. 6.3 (a), with Fig. 6.3 (b) showing only the part of the derivative originating from the time dependent part of the current.

Here, it can be deduced that the derivative  $\frac{d(\Delta I)}{dV_{\text{Bias}}}$  switches its sign at the van-Hove singularity  $eV_{\text{Bias}} = -\mu$ . This singularity can be deduced from the dispersion  $\epsilon_{\mathbf{k}}$  from Eq. (6.1b), as  $\epsilon_{\mathbf{k}=0} = -\mu$  and thereby the uncoupled Green's function from Eq. (6.2) has a singularity for  $\omega = -\mu$ .

As there is no band structure above  $eV_{\text{Bias}} = 4t_m - \mu$  and below  $eV_{\text{Bias}} = -4t_m - \mu$ , both derivatives vanish in these regions. From the full derivative, it can be seen that the derivative is mostly positive, resembling the shape of the unperturbed retarded

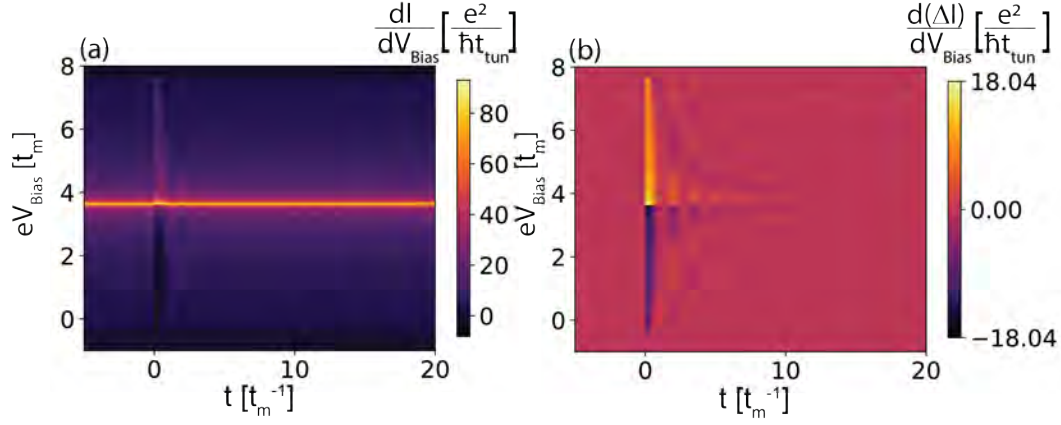


**Fig. 6.3:** Result for (a)  $\frac{dI}{dV_{\text{Bias}}}$  and (b)  $\frac{d(\Delta I)}{dV_{\text{Bias}}}$  for corrections in first order.

Green's function. The perturbation results in a partially negative full derivative  $\frac{dI}{dV_{\text{Bias}}}$  due to the large derivative resulting from  $\delta I(t)$ . This result stands in contrast to the unperturbed system, where the derivative is positive  $\frac{dI_0}{dV_{\text{Bias}}} > 0$ .

## 6.2 Superconducting System

In order to adapt our simulation further towards a vortex in a superconductor, the approach for a metallic site needs to be extended to the case of a superconducting site. For superconducting systems, we start from the Hamiltonian

$$\mathcal{H} = \sum_{\mathbf{k}, \sigma} \epsilon_{\mathbf{k}} c_{\mathbf{k}, \sigma}^{\dagger} c_{\mathbf{k}, \sigma} + \sum_{\mathbf{k}} \Delta_0 (c_{\mathbf{k}, \uparrow}^{\dagger} c_{-\mathbf{k}, \downarrow}^{\dagger} + c_{-\mathbf{k}, \downarrow} c_{\mathbf{k}, \uparrow}) \quad (6.21a)$$

$$= \sum_{\mathbf{k}} \epsilon_{\mathbf{k}} c_{\mathbf{k}, \uparrow}^{\dagger} c_{\mathbf{k}, \uparrow} - \epsilon_{-\mathbf{k}} c_{-\mathbf{k}, \downarrow} c_{-\mathbf{k}, \downarrow}^{\dagger} + \Delta_0 c_{\mathbf{k}, \uparrow}^{\dagger} c_{-\mathbf{k}, \downarrow}^{\dagger} + \Delta_0 c_{-\mathbf{k}, \downarrow} c_{\mathbf{k}, \uparrow} \quad (6.21b)$$

$$= \sum_{\mathbf{k}} \begin{pmatrix} c_{\mathbf{k}, \uparrow}^{\dagger} & c_{-\mathbf{k}, \downarrow} \end{pmatrix} \begin{pmatrix} \epsilon_{\mathbf{k}} & \Delta_0 \\ \Delta_0 & -\epsilon_{-\mathbf{k}} \end{pmatrix} \begin{pmatrix} c_{\mathbf{k}, \uparrow} \\ c_{-\mathbf{k}, \downarrow}^{\dagger} \end{pmatrix} \quad (6.21c)$$

$$= \sum_{\mathbf{k}} \begin{pmatrix} c_{\mathbf{k}, \uparrow}^{\dagger} & c_{-\mathbf{k}, \downarrow} \end{pmatrix} \hat{H}_{\mathbf{k}} \begin{pmatrix} c_{\mathbf{k}, \uparrow} \\ c_{-\mathbf{k}, \downarrow}^{\dagger} \end{pmatrix}. \quad (6.21d)$$

Here,  $\Delta_0$  corresponds to the superconducting order parameter and  $\epsilon_{\mathbf{k}}$  refers to the dispersion in the metallic phase. The superconducting Green's function, expressed through the fermionic Matsubara frequencies  $\omega_n = \frac{\pi}{\beta} (2n + 1)$  and Nambu notation,

is then given through

$$\hat{G}^{-1}(\mathbf{k}, i\omega_n) = i\omega_n \mathbb{1} - \hat{H}_{\mathbf{k}} \quad (6.22a)$$

$$= \begin{pmatrix} i\omega_n - \epsilon_{\mathbf{k}} & -\Delta_0 \\ -\Delta_0 & i\omega_n + \epsilon_{\mathbf{k}} \end{pmatrix}, \quad (6.22b)$$

where  $\epsilon_{\mathbf{k}} = \epsilon_{-\mathbf{k}}$  was used. Thus,

$$\hat{G}(\mathbf{k}, i\omega_n) = \frac{1}{(i\omega_n - \epsilon_{\mathbf{k}})(i\omega_n + \epsilon_{\mathbf{k}}) - \Delta_0^2} \begin{pmatrix} i\omega_n + \epsilon_{\mathbf{k}} & \Delta_0 \\ \Delta_0 & i\omega_n - \epsilon_{\mathbf{k}} \end{pmatrix} \quad (6.23a)$$

$$= \frac{1}{(i\omega_n)^2 - E_{\mathbf{k}}^2} \begin{pmatrix} i\omega_n + \epsilon_{\mathbf{k}} & \Delta_0 \\ \Delta_0 & i\omega_n - \epsilon_{\mathbf{k}} \end{pmatrix} \quad (6.23b)$$

is determined, with the dispersion in the superconducting state  $E_{\mathbf{k}} = \sqrt{\epsilon_{\mathbf{k}}^2 + \Delta_0^2}$ . The one-particle uncoupled, retarded or advanced Green's function is a  $2 \times 2$  matrix, which follows from the analytic continuation  $i\omega_n \rightarrow \omega \pm i\delta$ , which yields

$$\hat{g}_{ss,0}^{R,A}(\mathbf{k}, \omega) = \frac{1}{(\omega \pm i\delta)^2 - E_{\mathbf{k}}^2} \begin{pmatrix} \omega \pm i\delta + \epsilon_{\mathbf{k}} & \Delta_0 \\ \Delta_0 & \omega \pm i\delta - \epsilon_{\mathbf{k}} \end{pmatrix} \quad (6.24a)$$

$$= \begin{pmatrix} g_{ss,0,11}^{R,A}(\mathbf{k}, \omega) & f_{ss,0}^{R,A}(\mathbf{k}, \omega) \\ f_{ss,0}^{R,A}(\mathbf{k}, \omega) & g_{ss,0,22}^{R,A}(\mathbf{k}, \omega) \end{pmatrix}. \quad (6.24b)$$

In the final step of Eq. (6.24), we introduced denominations for both the off-diagonal, anomalous Green's functions  $f_{ss,0}^{R,A}(\mathbf{k}, \omega)$  and the diagonal, normal Green's functions  $g_{ss,0,11/22}^{R,A}(\mathbf{k}, \omega)$  for electronic and hole-like components. Once again, we only need the local Green's function for one site at  $\mathbf{r} = 0$ , such that the momentum dependency can be integrated out as part of a Fourier transformation at this specific site. Thereby, the energy-dependent retarded and advanced Green's functions are computed from

$$\hat{g}_0^{R,A}(\mathbf{r} = 0, \omega) = \int \frac{d^2k}{(2\pi)^2} g_0^{R,A}(\mathbf{k}, \omega). \quad (6.25)$$

For the Green's function of the tip, a metallic phase is still assumed. This Green's function also becomes a matrix, but with vanishing off-diagonal elements. The procedure for obtaining the coupled version of the retarded and advanced Green's functions remains the same, so that Equation (6.4) still applies. In this formula, it only needs to be taken into account that both uncoupled Green's functions are now matrices in the superconducting case.

Finally, the lesser Green's function is still derived from Equation (6.10). Nevertheless, electronic and hole-like components couple differently to the applied bias voltage. Therefore, the computation of the uncoupled, lesser Green's function for the tip has

an opposite relative sign for  $eV_{\text{Bias}}$  in the multiplied Fermi-Dirac distribution, as given by

$$\hat{g}_{\text{tt},0}^< = \begin{pmatrix} -2in_{\text{F}}(\omega - eV_{\text{Bias}}) \text{Im} g_{\text{tt},11}^r(\omega) & 0 \\ 0 & -2in_{\text{F}}(\omega + eV_{\text{Bias}}) \text{Im} g_{\text{tt},22}^r(\omega) \end{pmatrix}. \quad (6.26)$$

### 6.2.1 Time Dependence of the Induced Current for Constant Perturbations

With the adapted version of the retarded, lesser and advanced Green's function for the superconducting site, the current can now be calculated. Firstly, this is conducted for a constant perturbation. For the superconducting site and the metallic tip, the perturbation  $\hat{V}(t)$  is a  $4 \times 4$  matrix, which reads

$$\hat{V}(t) = \hat{V}(0) = \begin{pmatrix} 0 & 0 & 0 & 0 \\ 0 & 0 & 0 & 0 \\ 0 & 0 & J & 0 \\ 0 & 0 & 0 & J \end{pmatrix} \quad (6.27)$$

for a constant perturbation for  $t \in (-\infty, \infty)$ . For this case, the perturbation theory can also be conducted in frequency space, as the Dyson equation from Eq. (6.12) then reads

$$\begin{aligned} \hat{G}^<(t, t') &= \hat{G}_0^<(t, t') + \int dt_1 \hat{G}_0^R(t, t_1) \hat{V}(0) \hat{G}^<(t_1, t') \\ &+ \int dt_1 \hat{G}_0^<(t, t_1) \hat{V}(0) \hat{G}^A(t_1, t'). \end{aligned} \quad (6.28)$$

As the perturbation is constant in time and the unperturbed Green's function only depends on time differences, the perturbed Green's function  $\hat{G}_0^R(t, t') = \hat{G}_0^R(t - t')$  will also depend solely on time differences. Therefore, the frequency-dependent Green's function can be substituted into Eq. (6.28), which results in

$$\begin{aligned} \int \frac{d\omega}{2\pi} \hat{G}^<(\omega) e^{i\omega(t-t')} &= \int \frac{d\omega}{2\pi} \hat{G}_0^<(\omega) e^{i\omega(t-t')} \\ &+ \int dt_1 \int \frac{d\omega}{2\pi} \int \frac{d\omega'}{2\pi} \hat{G}_0^R(\omega) \hat{V}(0) \hat{G}^<(\omega') e^{i\omega(t-t_1)} e^{i\omega'(t_1-t')} \\ &+ \int dt_1 \int \frac{d\omega}{2\pi} \int \frac{d\omega'}{2\pi} \hat{G}_0^<(\omega) \hat{V}(0) \hat{G}^A(\omega') e^{i\omega(t-t_1)} e^{i\omega'(t_1-t')}. \end{aligned} \quad (6.29)$$

Then, with  $\int dt_1 e^{i(\omega' - \omega)t_1} = 2\pi\delta(\omega' - \omega)$  follows

$$\begin{aligned} \int \frac{d\omega}{2\pi} \hat{G}^<(\omega) e^{i\omega(t-t')} &= \int \frac{d\omega}{2\pi} \hat{G}_0^<(\omega) e^{i\omega(t-t')} \\ &+ \int \frac{d\omega}{2\pi} \hat{G}_0^R(\omega) \hat{V}(0) \hat{G}^<(\omega) e^{i\omega(t-t')} \\ &+ \int \frac{d\omega}{2\pi} \hat{G}_0^<(\omega) \hat{V}(0) \hat{G}^A(\omega) e^{i\omega(t-t')} . \end{aligned} \quad (6.30)$$

Here, the Dyson equation in frequency space is derived as

$$\hat{G}^<(\omega) = \hat{G}_0^<(\omega) + \hat{G}_0^R(\omega) \hat{V}(0) \hat{G}^<(\omega) + \hat{G}_0^<(\omega) \hat{V}(0) \hat{G}^A(\omega) . \quad (6.31)$$

This result looks rather similar to the Dyson equations for the retarded and advanced Green's functions [72]

$$\hat{G}^R(\omega) = \hat{G}_0^R(\omega) + \hat{G}_0^R(\omega) \hat{V}(0) \hat{G}^R(\omega) , \quad (6.32a)$$

$$\hat{G}^A(\omega) = \hat{G}_0^A(\omega) + \hat{G}_0^A(\omega) \hat{V}(0) \hat{G}^A(\omega) . \quad (6.32b)$$

### First and Second Order Approximation

From equation (6.31), the current's first and second order contributions can both be deduced by inserting the Dyson equation Eq. (6.31) and Eq. (6.32b) into Eq. (6.31), resulting in

$$\begin{aligned} \hat{G}^<(\omega) &= \hat{G}_0^<(\omega) + \hat{G}_0^R(\omega) \hat{V}(0) \hat{G}_0^<(\omega) + \hat{G}_0^<(\omega) \hat{V}(0) \hat{G}_0^A(\omega) \\ &+ \hat{G}_0^R(\omega) \hat{V}(0) \hat{G}_0^R(\omega) \hat{V}(0) \hat{G}_0^<(\omega) + \hat{G}_0^R(\omega) \hat{V}(0) \hat{G}_0^<(\omega) \hat{V}(0) \hat{G}_0^A(\omega) \\ &+ \hat{G}_0^<(\omega) \hat{V}(0) \hat{G}_0^A(\omega) \hat{V}(0) \hat{G}_0^A(\omega) . \end{aligned} \quad (6.33)$$

Here, the perturbed Green's functions are replaced by the unperturbed ones as  $\hat{G}^<(\omega) \rightarrow \hat{G}_0^<(\omega)$  and  $\hat{G}^A(\omega) \rightarrow \hat{G}_0^A(\omega)$ , in order to approximate  $\hat{G}^<(\omega)$  to the second order in the perturbation

$$\begin{aligned} \hat{G}^<(\omega)^{(2)} &= \hat{G}_0^<(\omega) + \hat{G}_0^R(\omega) \hat{V}(0) \hat{G}_0^<(\omega) + \hat{G}_0^<(\omega) \hat{V}(0) \hat{G}_0^A(\omega) \\ &+ \hat{G}_0^R(\omega) \hat{V}(0) \hat{G}_0^R(\omega) \hat{V}(0) \hat{G}_0^<(\omega) + \hat{G}_0^R(\omega) \hat{V}(0) \hat{G}_0^<(\omega) \hat{V}(0) \hat{G}_0^A(\omega) \\ &+ \hat{G}_0^<(\omega) \hat{V}(0) \hat{G}_0^A(\omega) \hat{V}(0) \hat{G}_0^A(\omega) . \end{aligned} \quad (6.34)$$

Then, the submatrices  $\hat{G}_{st}^{\leq}(\omega)^{(2)}$  and  $\hat{G}_{ts}^{\leq}(\omega)^{(2)}$  are calculated by inserting all the matrices

$$\begin{aligned} \hat{G}_0^{R,<,A}(\omega) &= \begin{pmatrix} \hat{G}_{0,tt}^{R,<,A}(\omega) & \hat{G}_{0,ts}^{R,<,A}(\omega) \\ \hat{G}_{0,st}^{R,<,A}(\omega) & \hat{G}_{0,ss}^{R,<,A}(\omega) \end{pmatrix} \\ &= \begin{pmatrix} G_{0,tt,11}^{R,<,A}(\omega) & F_{0,tt}^{R,<,A}(\omega) & G_{0,ts,11}^{R,<,A}(\omega) & F_{0,ts}^{R,<,A}(\omega) \\ F_{0,tt}^{R,<,A}(\omega) & G_{0,tt,22}^{R,<,A}(\omega) & F_{0,ts}^{R,<,A}(\omega) & G_{0,ts,22}^{R,<,A}(\omega) \\ G_{0,st,11}^{R,<,A}(\omega) & F_{0,st}^{R,<,A}(\omega) & G_{0,ss,11}^{R,<,A}(\omega) & F_{0,ss}^{R,<,A}(\omega) \\ F_{0,st}^{R,<,A}(\omega) & G_{0,st,22}^{R,<,A}(\omega) & F_{0,ss}^{R,<,A}(\omega) & G_{0,ss,22}^{R,<,A}(\omega) \end{pmatrix} \end{aligned} \quad (6.35)$$

and the form of the perturbation  $\hat{V}(0)$  from Eq. (6.27). The current can thereby be derived as

$$\hat{I}(\omega) = \hat{I}_0(\omega) + \delta^{(1)}\hat{I}(\omega) + \delta^{(2)}\hat{I}(\omega) \quad (6.36)$$

with

$$\hat{I}_0 = \frac{e}{\hbar} (-t_{\text{tun}}) \left[ \hat{G}_{0,ts}^{\leq}(\omega) - \hat{G}_{0,st}^{\leq}(\omega) \right], \quad (6.37)$$

$$\begin{aligned} \delta^{(1)}\hat{I}(\omega) &= \frac{e}{\hbar} (-t_{\text{tun}}) J \left[ \hat{G}_{0,ts}^R(\omega)\hat{G}_{0,ss}^{\leq}(\omega) + \hat{G}_{0,ts}^{\leq}(\omega)\hat{G}_{0,ss}^A(\omega) \right. \\ &\quad \left. - \hat{G}_{0,ss}^R(\omega)\hat{G}_{0,st}^{\leq}(\omega) - \hat{G}_{0,ss}^{\leq}(\omega)\hat{G}_{0,st}^A(\omega) \right] \end{aligned} \quad (6.38)$$

and

$$\begin{aligned} \delta^{(2)}\hat{I}(\omega) &= \frac{e}{\hbar} (-t_{\text{tun}}) J^2 \left[ \hat{G}_{0,ts}^R(\omega)\hat{G}_{0,ss}^R(\omega)\hat{G}_{0,ss}^{\leq}(\omega) + \hat{G}_{0,ts}^R(\omega)\hat{G}_{0,ss}^{\leq}(\omega)\hat{G}_{0,ss}^A(\omega) \right. \\ &\quad + \hat{G}_{0,ts}^{\leq}(\omega)\hat{G}_{0,ss}^A(\omega)\hat{G}_{0,ss}^A(\omega) - \hat{G}_{0,ss}^R(\omega)\hat{G}_{0,ss}^R(\omega)\hat{G}_{0,st}^{\leq}(\omega) \\ &\quad \left. - \hat{G}_{0,ss}^R(\omega)\hat{G}_{0,ss}^{\leq}(\omega)\hat{G}_{0,st}^A(\omega) - \hat{G}_{0,ss}^{\leq}(\omega)\hat{G}_{0,ss}^A(\omega)\hat{G}_{0,st}^A(\omega) \right], \end{aligned} \quad (6.39)$$

which is a  $2 \times 2$  matrix. Out of this matrix, we focus on the diagonal components and especially the 11-component  $I_{11}$ . The full current is then obtained by a Fourier transformation

$$\hat{I}(t) = \hat{I}(0) = \int \frac{d\omega}{2\pi} \hat{I}(\omega), \quad (6.40)$$

in order to calculate the constant current in real-time. We once again take the derivative  $\frac{dI}{dV_{\text{Bias}}}$  by  $V_{\text{Bias}}$  to check whether the result is proportional to the density of states. For the graph shown in Fig. 6.4, the 11-component of the current was calculated for 101 equidistant points in the interval  $[-0.5t_m, 0.5t_m]$  for  $J = 1.2t_m$ ,  $\Delta_0 = 0.3t_m$ ,  $t_{\text{tun}} = 0.01t_m$  and  $\mu = -3.618t_m$ .

There, the unperturbed version of the current's derivative (blue line) is compared with the result including first order contributions (orange line) and the result including second order contributions (green line) of the perturbation. It can be seen that

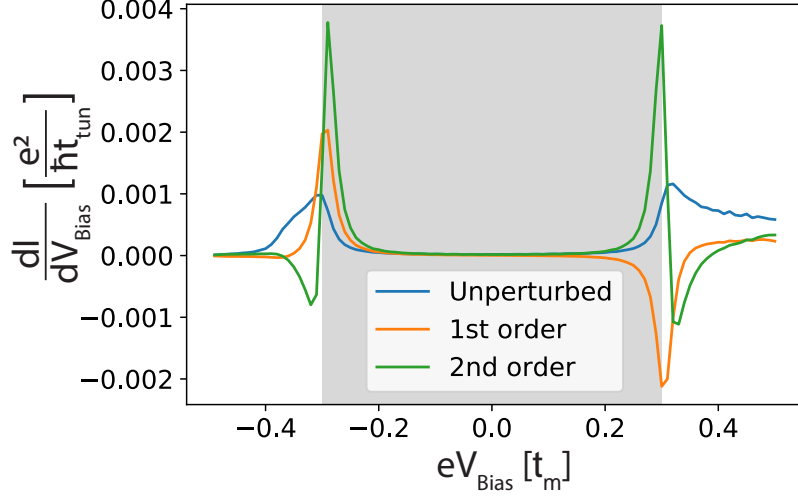


**Fig. 6.4:** Corrections to  $\frac{d\hat{I}_{11}}{dV_{\text{Bias}}}$  in first and second order of the perturbation.

the unperturbed version resembles the well-known version of the density of states for a superconductor. The coherence peaks lie at  $\pm\Delta_0$ , which is marked by the grey-shaded area.

The expected result for a superconducting system, where a magnetic perturbation is present permanently, is the occurrence of a Shiba state in the gap [31, 75, 76], which is visible in the density of states. This Shiba state takes the form of a peak with its position dependent on the strength of the perturbation  $J$ . However, the first and second order approximation of  $\frac{dI}{dV_{\text{Bias}}}$  do not exhibit such a state. Additionally, at the values of  $V_{\text{Bias}}$  where the coherence peaks are visible for the unperturbed system, the first and second order approximations show high peaks and unphysical negative values. If even higher orders are taken into account, the unphysical peaks become even more prominent. Therefore, it is clear that an order-by-order approach will not result in visible Shiba states.

### $\hat{T}$ -matrix Solution

Instead of calculating  $\frac{d\hat{I}_{11}}{dV_{\text{Bias}}}$  order by order, an approach using a  $\hat{T}$ -matrix can be taken, where an infinite number of orders is taken into account. By employing the two Dyson equations for the retarded and advanced Green's functions from Eq. (6.32) with Eq. (6.31), when the three matrices of Green's functions  $\hat{G}^{R,<,A}(\omega)$  are combined into one matrix [73], for both the perturbed and unperturbed case,

determined by

$$\hat{G}(\omega) = \begin{pmatrix} \hat{G}^R(\omega) & \hat{G}^<(\omega) \\ 0 & \hat{G}^A(\omega) \end{pmatrix} \quad (6.41)$$

and

$$\hat{G}_0(\omega) = \begin{pmatrix} \hat{G}_0^R(\omega) & \hat{G}_0^<(\omega) \\ 0 & \hat{G}_0^A(\omega) \end{pmatrix}. \quad (6.42)$$

With these two generalized matrices of Green's functions, the three Dyson equations become

$$\hat{G}(\omega) = \hat{G}_0(\omega) + \hat{G}_0(\omega)\hat{U}\hat{G}(\omega), \quad (6.43)$$

where we introduced the perturbation matrix

$$\hat{U} = \begin{pmatrix} 0 & 0 & 0 & 0 & 0 & 0 & 0 & 0 & 0 \\ 0 & 0 & 0 & 0 & 0 & 0 & 0 & 0 & 0 \\ 0 & 0 & J & 0 & 0 & 0 & 0 & 0 & 0 \\ 0 & 0 & 0 & J & 0 & 0 & 0 & 0 & 0 \\ 0 & 0 & 0 & 0 & 0 & 0 & 0 & 0 & 0 \\ 0 & 0 & 0 & 0 & 0 & 0 & 0 & 0 & 0 \\ 0 & 0 & 0 & 0 & 0 & 0 & J & 0 & 0 \\ 0 & 0 & 0 & 0 & 0 & 0 & 0 & 0 & J \end{pmatrix}. \quad (6.44)$$

In a  $\hat{T}$ -matrix approach, the Dyson equation can be solved by replacing  $\hat{U}\hat{G}(\omega)$  with  $\hat{T}(\omega)\hat{G}_0(\omega)$ , such that the solved Dyson equation becomes

$$\hat{G}(\omega) = \hat{G}_0(\omega) + \hat{G}_0(\omega)\hat{T}(\omega)\hat{G}_0(\omega). \quad (6.45)$$

From there,  $\hat{T}(\omega)$  can be determined from

$$\hat{T}(\omega)\hat{G}_0(\omega) = \hat{U}\hat{G}(\omega), \quad (6.46a)$$

which yields with Eq. (6.43)

$$\hat{T}(\omega)\hat{G}_0(\omega) = \hat{U}(\hat{G}_0(\omega) + \hat{G}_0(\omega)\hat{U}\hat{G}(\omega)) \quad (6.46b)$$

$$= \hat{U}\hat{G}_0(\omega) + \hat{U}\hat{G}_0(\omega)\hat{T}(\omega)\hat{G}_0(\omega). \quad (6.46c)$$

From here the following equation for the matrix  $\hat{T}$

$$\hat{T}(\omega) = \hat{U} + \hat{U}\hat{G}_0(\omega)\hat{T}(\omega), \quad (6.47)$$

is obtained, which can be rearranged to

$$(1 - \hat{U}\hat{G}_0(\omega))\hat{T}(\omega) = \hat{U} , \quad (6.48)$$

when  $\hat{T}(\omega)$  is factored out. A final operation of inversion then renders

$$\hat{T}(\omega) = (1 - \hat{U}\hat{G}_0(\omega))^{-1}\hat{U} . \quad (6.49)$$

This result can then be employed to calculate the lesser, advanced and retarded Green's function. We then use the lesser Green's function to calculate the current using Eq. (6.16) for the same 101 equidistant bias voltages from the interval  $V_{\text{Bias}} \in [-0.5t, 0.5t]$  as before and take the derivative  $\frac{dI}{dV_{\text{Bias}}}$ . The result is shown in Fig. 6.5 for  $J = 1.2t_m$ ,  $\Delta_0 = 0.3t_m$ ,  $t_{\text{tun}} = 0.01t_m$  and  $\mu = -3.618t_m$ , where the electronic and hole-like components, the derivatives of the 11- and 22-elements of the current, are compared to the unperturbed derivative.

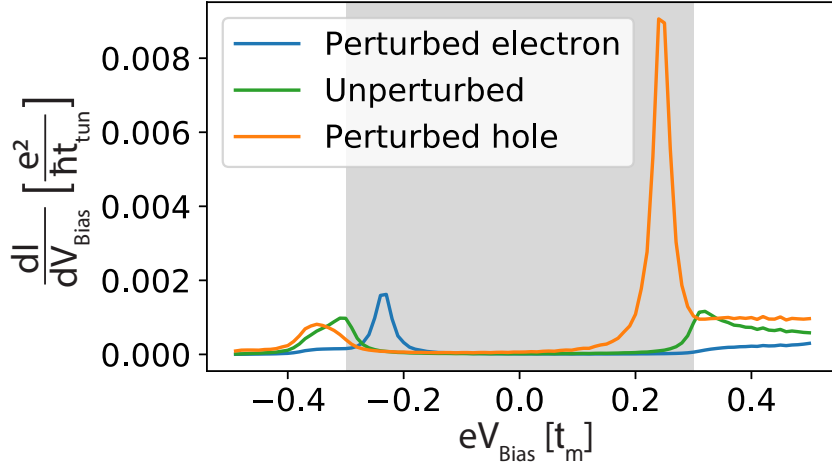


**Fig. 6.5:** Result for  $\frac{d\hat{I}_{11}}{dV_{\text{Bias}}}$  and  $\frac{d\hat{I}_{22}}{dV_{\text{Bias}}}$  compared to the unperturbed result for the  $\hat{T}$ -matrix approach, which exhibit two Shiba states in the superconducting gap.

In this plot, it can be seen that for both the derivative of the electronic and the hole-like component of the current, a Shiba state emerges. Both of these lie in the gap emerging for the unperturbed derivative, which is marked by the grey-shaded area. The peak from the electronic component lies on the left side of zero energy, while the Shiba state from the hole-like component lies at the symmetric position on the opposite side of zero energy. These two particle-like and hole-like branches of the Shiba state possess opposite spin polarizations, which can be seen from the

corresponding creation operator in Eq. (6.21). The Shiba state from the hole-like component has a much higher magnitude than the one from the particle-like branch. Furthermore, due to the emergence of the peaks, the rest of the density of states is flattened out for the two perturbed results, which is especially prominent at the energies where the coherence peaks are visible for the unperturbed result.

For constant perturbations, the density of states can also be derived directly through the energy-dependent, retarded Green's function from

$$N(\omega) = -\frac{1}{\pi} \text{Im} \hat{G}_{ss,11}^R(\omega), \quad (6.50)$$

where the perturbed, retarded Green's function is calculated from Eq. (6.45). This eliminates the necessity of calculating the current for a variety of bias voltages and then taking the derivative, which reduces the computation time significantly. Thereby,  $N(\omega)$  can be calculated for an interval of different perturbation strengths  $J$  and the effect on the position of the Shiba state can be analyzed. The result for  $N(\omega)$  from this procedure is illustrated in Fig. 6.6 in dependence of  $\omega$  and  $J$ .  $N(\omega)$  was calculated here for  $J \in [0t_m, 5t_m]$ . For the numerical calculation, this interval is discretized into 501 equidistant points.

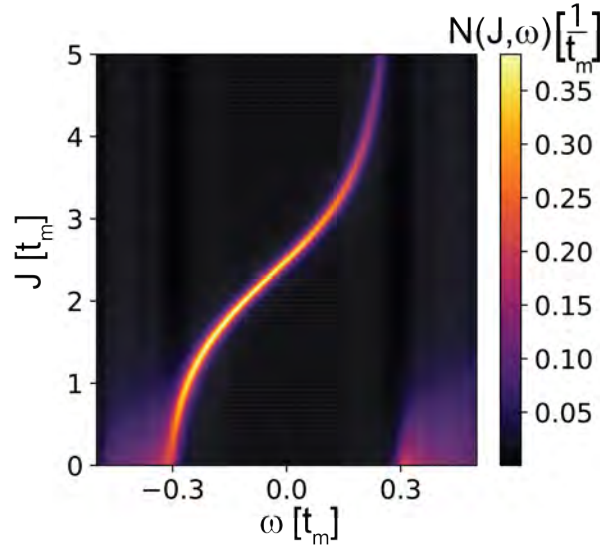


**Fig. 6.6:**  $N(J, \omega)$  showing the energy and intensity of the Shiba state in the superconducting gap and its dependence on  $J$ .

The result shows that the Shiba state of the electronic state emerges for small  $J$  on the left side of the gap visible in the density of states. As  $J$  increases, its position varies slowly from the left side of the gap over to the right side, which is approximately reached at  $J \approx 5t_m$ . The density of states of the Shiba state reaches its maximum at zero energy, at approximately  $J \approx 2.5t_m$ . Here, a phase transition occurs from a singlet  $S = 0$  state to a doublet  $S = 1/2$  state, as the particle-like and hole-like branches cross zero energy [75].

### 6.2.2 Time Dependence of the Induced Current for Instantaneous Perturbations

Since a  $\hat{T}$ -matrix approach worked best for the case of constant magnetic perturbations, this procedure is now transferred to  $\delta$ -pulse perturbations. For this kind of perturbation

$$\hat{V}(t) = \hat{V}\delta(t - t_0) = \begin{pmatrix} 0 & 0 & 0 & 0 \\ 0 & 0 & 0 & 0 \\ 0 & 0 & J & 0 \\ 0 & 0 & 0 & J \end{pmatrix} \delta(t - t_0), \quad (6.51)$$

the Dyson equations in real-time read

$$\hat{G}^R(t, t') = \hat{G}_0^R(t, t') + \hat{G}_0^R(t, t_0)\hat{V}\hat{G}^R(t_0, t'), \quad (6.52a)$$

$$\hat{G}^<(t, t') = \hat{G}_0^<(t, t') + \hat{G}_0^R(t, t_0)\hat{V}\hat{G}^<(t_0, t') + \hat{G}_0^A(t, t_0)\hat{V}(0)\hat{G}^A(t_0, t'), \quad (6.52b)$$

$$\hat{G}^A(t, t') = \hat{G}_0^A(t, t') + \hat{G}_0^A(t, t_0)\hat{V}\hat{G}^A(t_0, t'). \quad (6.52c)$$

Using the same combined matrices as introduced in Eq. (6.42) for the real times  $t$  and  $t'$  as

$$\hat{G}(t, t') = \begin{pmatrix} \hat{G}^R(t, t') & \hat{G}^<(t, t') \\ 0 & \hat{G}^A(t, t') \end{pmatrix} \quad (6.53)$$

and

$$\hat{G}_0(t, t') = \begin{pmatrix} \hat{G}_0^R(t, t') & \hat{G}_0^<(t, t') \\ 0 & \hat{G}_0^A(t, t') \end{pmatrix}, \quad (6.54)$$

the Dyson equation becomes

$$\hat{G}(t, t') = \hat{G}_0(t, t') + \hat{G}_0(t, t_0)\hat{U}\hat{G}(t_0, t'). \quad (6.55)$$

With the same perturbation matrix as for the constant case, listed in Eq. (6.44). A  $\hat{T}(t_0)$ -matrix for the solution of this problem can then be found for  $\hat{G}(t_0, t')$  and is determined from

$$\hat{G}(t_0, t') = \hat{G}_0(t_0, t') + \hat{G}_0(t_0, t_0)\hat{T}(t_0)\hat{G}_0(t_0, t') , \quad (6.56)$$

where it can be deduced that  $\hat{T}(t_0)\hat{G}_0(t_0, t') = \hat{U}\hat{G}(t_0, t')$ . Accordingly, it follows that

$$\hat{T}(t_0)\hat{G}_0(t_0, t') = \hat{U} \left( \hat{G}_0(t_0, t') + \hat{G}_0(t_0, t_0)\hat{U}\hat{G}(t_0, t') \right) , \quad (6.57)$$

where  $\hat{T}$  can be resubstituted to yield

$$\hat{T}(t_0)\hat{G}_0(t_0, t') = \hat{U}\hat{G}_0(t_0, t') + \hat{U}\hat{G}_0(t_0, t_0)\hat{T}(t_0)\hat{G}_0(t_0, t') . \quad (6.58)$$

Thus

$$\hat{T}(t_0) = \hat{U} + \hat{U}\hat{G}_0(t_0, t_0)\hat{T}(t_0) , \quad (6.59)$$

which yields the solution

$$\hat{T}(t_0) = (1 - \hat{U}\hat{G}_0(t_0, t_0))^{-1}\hat{U} . \quad (6.60)$$

Then, the perturbed Green's function can be calculated by combining equations (6.55) and (6.56) to

$$\hat{G}(t, t') = \hat{G}_0(t, t') + \hat{G}_0(t, t_0)\hat{U}\hat{G}_0(t_0, t') + \hat{G}_0(t, t_0)\hat{U}\hat{G}_0(t_0, t_0)\hat{T}(t_0)\hat{G}_0(t_0, t') . \quad (6.61)$$

The current is then calculated from Eq. (6.16), yielding a  $2 \times 2$ -matrix. In Fig. 6.7 (a), the result for the current is shown at  $V_{\text{Bias}} = 0t_m$ . The plot exhibits a vanishing constant contribution, from which it deviates when the perturbation is applied. This oscillation vanishes over time with the current relaxing to zero again. Finally, the derivative  $\frac{dI}{dV_{\text{Bias}}}$  was taken with the result shown in Fig. 6.7 (b) for  $J = 1.2t_m$ ,  $\Delta_0 = 0.3t_m$ ,  $t_{\text{tun}} = 0.01t_m$  and  $\mu = -3.618t_m$ .

Here, the coherence peaks from the unperturbed result are still visible. However, contrary to the result in equilibrium, this derivative shows negative values and thus cannot be interpreted as a density of states any longer.

### 6.2.3 Time Dependence of the Superconducting Order Parameter for Instantaneous Perturbations

For the case of a superconducting site, the magnetic perturbation will also have an effect on the superconducting order parameter. In the following, this influence will be

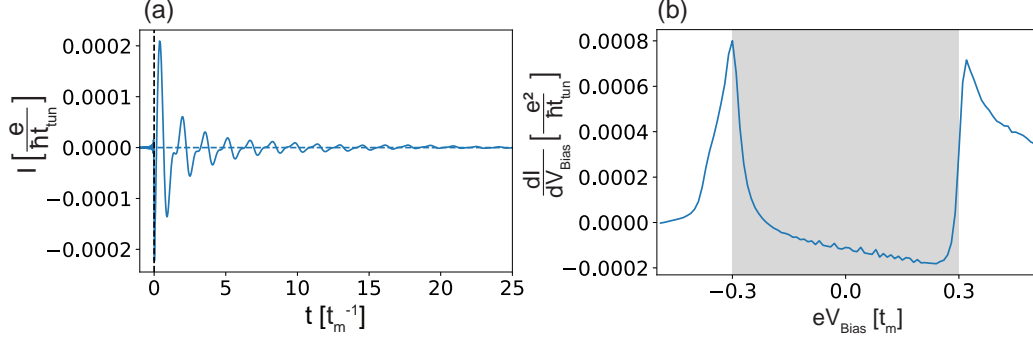


**Fig. 6.7:** (a) Time dependent current  $\hat{I}_{11}(t)$  at  $eV_{\text{Bias}} = 0t_m$  with the dashed line marking the constant value of the current in equilibrium, (b) result for  $\frac{d\hat{I}_{11}}{dV_{\text{Bias}}}$  for  $\delta$ -pulse perturbations.

analyzed using the Keldysh formalism [70, 73]. The dynamics of the superconducting order parameter out of equilibrium have been investigated previously. Most notably, an exact solution for all initial conditions and a complete set of integrals of motion for the mean-field BCS dynamics was found by Yuzbashyan et al. [77]. Here, the time dependence of the superconducting order parameter is investigated, in order to determine whether this time dependence needs to be included in the introduced approach and the conducted calculations.

### Theoretical Method

The superconducting order parameter can be determined from the gap equation [78–80]

$$\Delta(t) = -V \langle c_{\mathbf{r}=0,\uparrow}^\dagger c_{\mathbf{r}=0,\downarrow}^\dagger \rangle = iV f^<(\mathbf{r} = 0, t), \quad (6.62)$$

for which the uncoupled lesser anomalous Green's function  $f^<(\mathbf{r} = 0, t)$  is required. Here,  $V$  is the pairing interaction. This lesser Green's function can be computed via

$$\hat{g}^<(t, t) = \hat{g}_0^<(t, t) + \int dt_1 \hat{g}_0^R(t, t_1) \hat{J}(t_1) \hat{g}^<(t_1, t) + \int dt_1 \hat{g}_0^<(t, t_1) \hat{J}(t_1) \hat{g}^A(t_1, t), \quad (6.63)$$

where  $\hat{J}(t_1)$  is the time dependent perturbation and the spatial coordinate was omitted, as only a single site is considered. A magnetic perturbation is assumed that only occurs at a time  $t = t_0$ , given by

$$\hat{J}(t_1) = J \begin{pmatrix} 1 & 0 \\ 0 & 1 \end{pmatrix} \delta(t_1 - t_0). \quad (6.64)$$

For a small perturbation, the lesser Green's function is expanded to the second order in the perturbation as

$$\begin{aligned}
 \hat{g}^<(t, t) &= \hat{g}_0^<(t, t) + \int dt_1 \hat{g}_0^R(t, t_1) J \sigma_0 \delta(t_1 - t_0) \hat{g}_0^<(t_1, t) \\
 &+ \int dt_1 \hat{g}_0^<(t_1, t) J \sigma_0 \delta(t - t_0) \hat{g}_0^A(t_1, t) \\
 &+ \int dt_1 \int dt_2 \hat{g}_0^R(t, t_1) J \sigma_0 \delta(t_1 - t_0) \hat{g}_0^R(t_1, t_2) J \sigma_0 \delta(t_2 - t_0) \hat{g}_0^<(t_2, t) \\
 &+ \int dt_1 \int dt_2 \hat{g}_0^R(t, t_1) J \sigma_0 \delta(t_1 - t_0) \hat{g}_0^<(t_1, t_2) J \sigma_0 \delta(t_2 - t_0) \hat{g}_0^A(t_2, t) \\
 &+ \int dt_1 \int dt_2 \hat{g}_0^<(t, t_1) J \sigma_0 \delta(t_1 - t_0) \hat{g}_0^A(t_1, t_2) J \sigma_0 \delta(t_2 - t_0) \hat{g}_0^A(t_2, t)
 \end{aligned} \tag{6.65a}$$

$$\begin{aligned}
 &= \hat{g}_0^<(t, t) + J [\hat{g}_0^R(t, t_0) \hat{g}_0^<(t_0, t) + \hat{g}_0^<(t, t_0) \hat{g}_0^A(t_0, t)] \\
 &+ J^2 [\hat{g}_0^R(t, t_0) \hat{g}_0^R(t_0, t_0) \hat{g}_0^<(t_0, t) + \hat{g}_0^R(t, t_0) \hat{g}_0^<(t_0, t_0) \hat{g}_0^A(t_0, t) \\
 &+ \hat{g}_0^<(t, t_0) \hat{g}_0^A(t_0, t_0) \hat{g}_0^A(t_0, t)] .
 \end{aligned} \tag{6.65b}$$

The final result is then

$$\begin{aligned}
 \hat{g}^<(t, t) &= \hat{g}_0^<(0) + J [\hat{g}_0^R(\Delta t) \hat{g}_0^<(-\Delta t) + \hat{g}_0^<(\Delta t) \hat{g}_0^A(-\Delta t)] \\
 &+ J^2 [\hat{g}_0^R(\Delta t) \hat{g}_0^R(0) \hat{g}_0^<(-\Delta t) + \hat{g}_0^R(\Delta t) \hat{g}_0^<(0) \hat{g}_0^A(-\Delta t) \\
 &+ \hat{g}_0^<(\Delta t) \hat{g}_0^A(0) \hat{g}_0^A(-\Delta t)] ,
 \end{aligned} \tag{6.66}$$

where we defined  $\Delta t = t - t_0$ . The pairing interaction can be calculated from the gap equation for the unperturbed, lesser anomalous Green's function. In the unperturbed system, the superconducting order parameter is given through

$$\Delta_0 = i V f_0^<(r = 0, t = 0) , \tag{6.67a}$$

which leads to

$$\Delta_0 = -V \int_{-\infty}^0 \frac{d\omega}{\pi} \text{Im} f_0^<(r = 0, \omega) \tag{6.67b}$$

$$= -V \int_{-\infty}^0 \frac{d\omega}{\pi} \int \frac{d^2 k}{(2\pi)^2} \text{Im} \left[ \frac{\Delta_0}{(\omega + i\delta)^2 - E_{\mathbf{k}}^2} \right] , \tag{6.67c}$$

with  $f_0^<(\omega) = n_{\text{F}}(\omega) \text{Im} f_0^R(r = 0, \omega)$  and  $T = 0$ . Rearranging this equation then yields the final result for the pairing interaction

$$V = - \frac{1}{\int_{-\infty}^0 \frac{d\omega}{\pi} \int \frac{d^2 k}{(2\pi)^2} \text{Im} \left[ \frac{1}{(\omega + i\delta)^2 - E_{\mathbf{k}}^2} \right]} . \tag{6.68}$$

### First Order Contribution

The first order correction to the lesser, anomalous Green's function at a point of time  $t$  with a perturbation  $J\delta(t_1 - t_0)\mathbb{1}_{2 \times 2}$  occurring at  $t_0$  is given by

$$\begin{aligned} \Delta f^<(t, t)^{(1)} = & J [g_{0,11}^R(\Delta t) f_0^<(-\Delta t) + f_0^R(\Delta t) g_{0,22}^<(-\Delta t) + g_{0,11}^<(\Delta t) f_0^A(-\Delta t) \\ & + f_0^<(\Delta t) g_{0,22}^A(-\Delta t)] \end{aligned} \quad (6.69)$$

with  $\Delta t = t - t_0$ .

From the definition of the uncoupled Green's function matrix in Eq. (6.24), the symmetry relations

$$g_{0,11}^R(k, \omega) = g_{0,11}^A(\mathbf{k}, \omega)^* = -g_{0,22}^A(\mathbf{k}, -\omega), \quad (6.70)$$

$$g_{0,22}^R(k, \omega) = g_{0,22}^A(\mathbf{k}, \omega)^* = -g_{0,11}^A(\mathbf{k}, -\omega), \quad (6.71)$$

$$f_0^R(k, \omega) = f_0^A(\mathbf{k}, \omega)^* = f_0^A(\mathbf{k}, -\omega) \quad (6.72)$$

can be determined. In the time domain, these are analogous to the following symmetry relations

$$g_{0,11}^A(\mathbf{k}, \Delta t) = \frac{1}{2\pi} \int_{-\infty}^{\infty} \frac{d\omega}{\pi} \frac{\omega - i\delta \pm \epsilon_{\mathbf{k}}}{(\omega - i\delta)^2 - E_{\mathbf{k}}^2} e^{-i\omega\Delta t} \quad (6.73a)$$

$$= \frac{1}{2\pi} \int_{-\infty}^{\infty} \frac{d\omega}{\pi} \left( \frac{\omega + i\delta \pm \epsilon_{\mathbf{k}}}{(\omega + i\delta)^2 - E_{\mathbf{k}}^2} \right)^* e^{-i\omega\Delta t} \quad (6.73b)$$

$$= \left( \frac{1}{2\pi} \int_{-\infty}^{\infty} \frac{d\omega}{\pi} \frac{\omega + i\delta \pm \epsilon_{\mathbf{k}}}{(\omega + i\delta)^2 - E_{\mathbf{k}}^2} e^{-i\omega(-\Delta t)} \right)^* \quad (6.73c)$$

$$= g_{0,11}^R(\mathbf{k}, -\Delta t)^* \quad (6.73d)$$

and equally

$$g_{0,22}^A(\mathbf{k}, \Delta t) = g_{0,22}^R(\mathbf{k}, -\Delta t)^*, \quad (6.74)$$

as well as

$$g_{0,11}^R(\mathbf{k}, \Delta t) = \frac{1}{2\pi} \int_{-\infty}^{\infty} \frac{d\omega}{\pi} g_{0,11}^R(\mathbf{k}, \omega) e^{-i\omega\Delta t} \quad (6.75a)$$

$$= -\frac{1}{2\pi} \int_{-\infty}^{\infty} \frac{d\omega}{\pi} g_{0,22}^A(\mathbf{k}, -\omega) e^{-i\omega\Delta t} \quad (6.75b)$$

$$\stackrel{\omega \rightarrow -\omega}{=} -\frac{1}{2\pi} \int_{-\infty}^{\infty} \frac{d\omega}{\pi} g_{0,22}^A(\mathbf{k}, \omega) e^{i\omega\Delta t} \quad (6.75c)$$

$$= -g_{0,22}^A(\mathbf{k}, -\Delta t) \quad (6.75d)$$

and

$$f_0^R(\mathbf{k}, \Delta t) = \frac{1}{2\pi} \int_{-\infty}^{\infty} \frac{d\omega}{\pi} f_0^R(\mathbf{k}, \omega) e^{-i\omega\Delta t} \quad (6.76a)$$

$$= \frac{1}{2\pi} \int_{-\infty}^{\infty} \frac{d\omega}{\pi} f_0^A(\mathbf{k}, \omega)^* e^{-i\omega\Delta t} \quad (6.76b)$$

$$= \left( \frac{1}{2\pi} \int_{-\infty}^{\infty} \frac{d\omega}{\pi} f_0^A(\mathbf{k}, \omega) e^{-i\omega(-\Delta t)} \right)^* \quad (6.76c)$$

$$= f_0^A(\mathbf{k}, -\Delta t)^* . \quad (6.76d)$$

The anomalous, retarded and advanced Green's functions are also completely real, which can be seen from the property

$$f_0^A(\mathbf{k}, -\Delta t) = \frac{1}{2\pi} \int_{-\infty}^{\infty} \frac{d\omega}{\pi} f_0^A(\mathbf{k}, \omega) e^{i\omega\Delta t} \quad (6.77a)$$

$$= \frac{1}{2\pi} \int_{-\infty}^{\infty} \frac{d\omega}{\pi} f_0^A(\mathbf{k}, -\omega) e^{-i\omega\Delta t} \quad (6.77b)$$

$$= \frac{1}{2\pi} \int_{-\infty}^{\infty} \frac{d\omega}{\pi} f_0^R(\mathbf{k}, \omega) e^{-i\omega\Delta t} \quad (6.77c)$$

$$= f_0^R(\mathbf{k}, \Delta t) . \quad (6.77d)$$

Thereby  $f_0^{R,A}(\mathbf{k}, \Delta t) = f_0^{R,A}(\mathbf{k}, \Delta t)^*$ , so that its respective imaginary part has to be equal to zero.

Thus, Eq. (6.69) can be expressed solely in terms of the retarded Green's functions through

$$\Delta f^<(t, t)^{(1)} = J [g_{0,11}^R(\Delta t)(f_0^<(-\Delta t) - f_0^<(\Delta t)) + f_0^R(\Delta t)g_{0,22}^<(-\Delta t) + g_{0,11}^<(\Delta t)f_0^R(\Delta t)^*] \quad (6.78a)$$

$$= J [g_{0,11}^R(\Delta t)(f_0^<(-\Delta t) - f_0^<(\Delta t)) + f_0^R(\Delta t)(g_{0,22}^<(-\Delta t) + g_{0,11}^<(\Delta t))] . \quad (6.78b)$$

Because the imaginary part of  $f_0^R(\omega)$  is an odd function and the real part is an even function, the Fourier transformation is entirely real, so that the two terms with  $f_0^R(\Delta t)^{(*)}$  can be summarized in the last step. In order to show that the first order vanishes, it is useful to employ the greater Green's functions  $\hat{g}^>(\omega)$ . In the frequency domain, these can be derived from the retarded and advanced Green's functions through

$$g^>(\omega) = (1 - n_F(\omega))(\hat{g}_0^R(k, \omega) - \hat{g}_0^A(k, \omega)) \quad (6.79a)$$

$$= 2i(1 - n_F(\omega))\text{Im}[\hat{g}^R(\omega)] \quad (6.79b)$$

and another useful property is

$$\hat{g}^>(\omega) - \hat{g}^<(\omega) = \hat{g}^R(\omega) - \hat{g}^A(\omega) . \quad (6.80)$$

With the greater Green's function, the symmetry properties

$$f_0^<(-\Delta t) = f_0^>(\Delta t) \quad (6.81)$$

and

$$g_{0,22}^<(-\Delta t) = -g_{0,11}^>(\Delta t) \quad (6.82)$$

between its entries and those of the lesser Green's function can be employed. Thereby the expression for the first order correction can be further simplified, while using Eq.(6.80) in the final step, and vanishes as

$$\Delta f^<(t, t)^{(1)} = J [g_{0,11}^R(\Delta t)(f_0^>(\Delta t) - f_0^<(\Delta t)) + f_0^R(\Delta t)(-g_{0,11}^>(\Delta t) + g_{0,11}^<(\Delta t))] \quad (6.83a)$$

$$= J [g_{0,11}^R(\Delta t)(f_0^R(\Delta t) - f_0^A(\Delta t)) - f_0^R(\Delta t)(g_{0,11}^R(\Delta t) - g_{0,11}^A(\Delta t))] \quad (6.83b)$$

$$= 0 , \quad (6.83c)$$

because the advanced Green's function is equal to zero at positive time intervals  $\Delta t > 0$ .

## Second Order Contribution

The correction to the lesser Green's functions in second order is given through

$$\Delta \hat{g}^<(t, t)^{(2)} = J^2 (\hat{g}^R(\Delta t) \hat{g}^R(0) \hat{g}^<(-\Delta t) + \hat{g}^R(\Delta t) \hat{g}^<(0) \hat{g}^A(-\Delta t) + \hat{g}^<(\Delta t) \hat{g}^A(0) \hat{g}^A(-\Delta t)) . \quad (6.84)$$

From there, the correction for the anomalous, lesser Green's function at position (1, 2) in the matrix above can be derived to be

$$\begin{aligned} \Delta f_{12}^<(t, t)^{(2)} = & g_{0,11}^R(\Delta t) g_{0,11}^R(0) f_0^<(-\Delta t) + f_0^R(\Delta t) f_0^R(0) f_0^<(-\Delta t) \\ & + g_{0,11}^R(\Delta t) f_0^R(0) g_{0,22}^<(-\Delta t) + f_0^R(\Delta t) g_{0,22}^R(0) g_{0,22}^<(-\Delta t) \\ & + g_{0,11}^R(\Delta t) g_{0,11}^<(0) f_0^A(-\Delta t) + f_0^R(\Delta t) f_0^<(0) f_0^A(-\Delta t) \\ & + g_{0,11}^R(\Delta t) f_0^<(0) g_{0,22}^A(-\Delta t) + f_0^R(\Delta t) g_{0,22}^<(0) g_{0,22}^A(-\Delta t) \\ & + g_{0,11}^<(\Delta t) g_{0,11}^A(0) f_0^A(-\Delta t) + f_0^<(\Delta t) f_0^A(0) f_0^A(-\Delta t) \\ & + g_{0,11}^<(\Delta t) f_0^A(0) g_{0,22}^A(-\Delta t) + f_0^<(\Delta t) g_{0,22}^A(0) g_{0,22}^A(-\Delta t) . \end{aligned} \quad (6.85)$$

This can be structured better by ordering it in the following way

$$\begin{aligned}
 \Delta f_{12}^{\leq}(t, t)^{(2)} &= g_{0,11}^R(\Delta t)g_{0,11}^R(0)f_0^{\leq}(-\Delta t) + g_{0,11}^R(\Delta t)f_0^{\leq}(0)g_{0,22}^A(-\Delta t) \\
 &\quad + f_0^{\leq}(\Delta t)g_{0,22}^A(0)g_{0,22}^A(-\Delta t) \\
 &\quad + f_0^R(\Delta t)f_0^R(0)f_0^{\leq}(-\Delta t) + f_0^R(\Delta t)f_0^{\leq}(0)f_0^A(-\Delta t) \\
 &\quad + f_0^{\leq}(\Delta t)f_0^A(0)f_0^A(-\Delta t) \\
 &\quad + g_{0,11}^R(\Delta t)f_0^R(0)g_{0,22}^{\leq}(-\Delta t) + f_0^R(\Delta t)g_{0,22}^R(0)g_{0,22}^{\leq}(-\Delta t) \\
 &\quad + f_0^R(\Delta t)g_{0,22}^{\leq}(0)g_{0,22}^A(-\Delta t) \\
 &\quad + g_{0,11}^R(\Delta t)g_{0,11}^{\leq}(0)f_0^A(-\Delta t) + g_{0,11}^{\leq}(\Delta t)g_{0,11}^A(0)f_0^A(-\Delta t) \\
 &\quad + g_{0,11}^{\leq}(\Delta t)f_0^A(0)g_{0,22}^A(-\Delta t) .
 \end{aligned} \tag{6.86}$$

Complex conjugating this yields

$$\begin{aligned}
 (\Delta f_{12}^{\leq}(t, t)^{(2)})^* &= -g_{0,11}^A(-\Delta t)g_{0,11}^A(0)f_0^{\leq}(-\Delta t) - g_{0,11}^A(-\Delta t)f_0^{\leq}(0)g_{0,22}^R(\Delta t) \\
 &\quad - f_0^{\leq}(-\Delta t)g_{0,22}^R(0)g_{0,22}^R(\Delta t) \\
 &\quad - f_0^A(-\Delta t)f_0^A(0)f_0^{\leq}(\Delta t) - f_0^A(-\Delta t)f_0^{\leq}(0)f_0^R(\Delta t) \\
 &\quad - f_0^{\leq}(\Delta t)f_0^R(0)f_0^R(\Delta t) \\
 &\quad - g_{0,11}^A(-\Delta t)f_0^A(0)g_{0,22}^{\leq}(\Delta t) - f_0^A(-\Delta t)g_{0,22}^A(0)g_{0,22}^{\leq}(\Delta t) \\
 &\quad - g_{0,11}^A(-\Delta t)g_{0,11}^{\leq}(0)f_0^R(\Delta t) + g_{0,11}^{\leq}(-\Delta t)g_{0,11}^R(0)f_0^R(\Delta t) \\
 &\quad - g_{0,11}^{\leq}(-\Delta t)f_0^R(0)g_{0,22}^R(\Delta t)
 \end{aligned} \tag{6.87}$$

by using

$$g_{0,11/22}^R(\Delta t)^* = g_{0,11/22}^A(-\Delta t) \tag{6.88a}$$

$$f_0^R(\Delta t)^* = f_0^A(-\Delta t) \tag{6.88b}$$

$$g_{0,11/22}^{\leq}(\Delta t)^* = -g_{0,11/22}^{\leq}(-\Delta t) \tag{6.88c}$$

$$f_0^{\leq}(\Delta t)^* = -f_0^{\leq}(-\Delta t) . \tag{6.88d}$$

Here, it can be deduced that the second order contribution is not entirely imaginary, thereby allowing the superconducting order parameter to become complex.

## Result

With the theoretical method introduced previously, the superconducting order parameter was calculated for  $\mu = -3.618t_m$ ,  $\Delta_0 = 0.3t_m$  and  $J = 0.1t_m$ , with the result shown in Fig. 6.8. The value of the pairing interaction obtained for this case is

$$V = 3.856t_m.$$

Here, it can be seen that the superconducting order parameter deviates from its original value of  $\Delta_0$  at  $t = 0$ , when the perturbation is applied. At the same time, the order parameter becomes complex. Over time, the real part oscillates back to  $\Delta_0$ , and the imaginary part vanishes again.

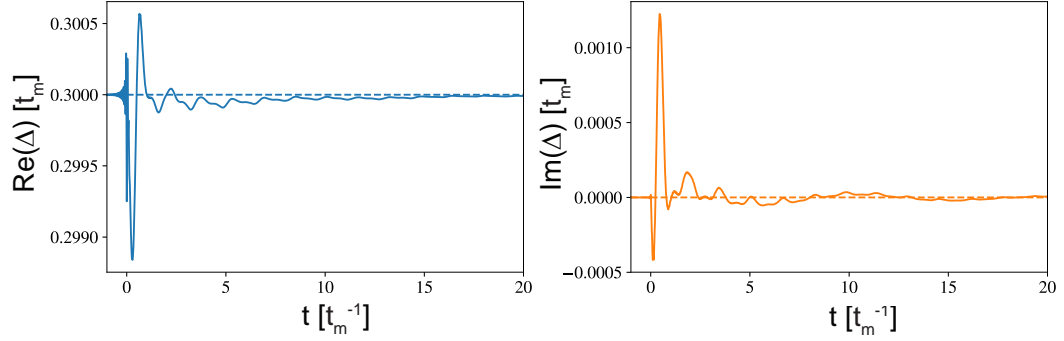


**Fig. 6.8:** Calculated time dependence of the superconducting gap for  $(\mu, \Delta_0, J) = (-3.618t_m, 0.3t_m, 0.1t_m)$ .

Here, the relaxation time of the system towards the instantaneous perturbation can be interpreted. Because instantaneous perturbations are applied, it is natural for the superconducting order parameter to return to its original value. The oscillations decay very quickly, so that after approximately  $t \approx 10 \frac{1}{t_m}$ , the oscillations in the real part are hardly perceivable. Thereby, the relaxation time is of the order of magnitude  $T_{\text{relax}} \sim \frac{\hbar}{\Delta_0}$ , where  $\hbar$  is included, so that the correct units are clear. In the calculations, it is set to unity. Thereby, the system's superconducting order parameter approaches its equilibrium value quickly enough that this influence does not have to be included in the calculations of the current.

## 7 Conclusion and Outlook

In conclusion, it was demonstrated successfully that the 3Q magnetic ordering, which was discovered recently, possesses topological properties when it is employed for the creation of an MSH structure. Due to the non-collinearity of the spin structure, an effective Rashba spin-orbit coupling is induced, which allows for the MSH structure to enter topological phases. The rich phase diagram obtained by the calculation of the Chern number of this magnetic ordering shows that this phenomenon is robust for a variety of parameters. Here, all the phase transitions originated from the high symmetry points of the Brillouin zone.

Furthermore, the emergence of edge modes was shown both for finite islands of magnetic adatoms as well as for semi-infinite ribbons. Here, we showed that both the LDOS at an energy of zero and the supercurrents are strongly localized on the edge of the investigated magnetic structure and that the supercurrents have a defined chirality depending on the sign of the Chern number. The supercurrents also serve to distinguish between topological and trivial phases through their magnitude, since the supercurrents are smaller by a factor of approximately 10 in the trivial case.

Finally, the experimentally motivated model illustrated that the topological properties also occur in a more realistic scenario and are a robust phenomenon for a large set of parameters. Here, phase transitions also originated from other points in the Brillouin zone instead of its high symmetry points.

For further investigations of the 3Q structure, an interesting step would be to experimentally construct an MSH structure with a 3Q-ordered magnetic layer and test the theoretical predictions made in this work. Here, it should be noted again that the chosen set of parameters included an unrealistically large superconducting order parameter, in order to reduce the program's run time.

Next, the topological properties for a ribbon filled with skyrmions were analyzed. Similar to the 3Q structure, a lattice filled with skyrmions has a rich phase diagram. The calculated band structure, in dependence of the crystal momentum parallel to the ribbon's infinite direction, matches the number of Majorana modes traversing the gap expected from the Chern number of the investigated phase. The LDOS at zero energy is strongly localized at the edge of the ribbon, but shows local minima around the skyrmion centers.

For this MSH structure, the supercurrents are present throughout the ribbon and form vortices around each skyrmion center. In the topological case, these vortices are

even stronger at the edge of the ribbon, where the LDOS is also strongest, and exhibit a perceivable edge current. In comparison to this result for the topological phase, the investigated trivial set of parameters leads to a supercurrent whose magnitude is two orders of magnitude smaller. Moreover, no edge current is present on the ribbon and the vortices have the same strength over the entire ribbon. Hence, these supercurrents cancel when the contributions on both sides of the domain wall are summed over.

Thus, the investigation of the supercurrents offers an interesting option to show the existence of topological edge modes, as the magnetic field they induce can also be measured experimentally. Furthermore, the skyrmionic spin structure is much more complicated than the 3Q structure, which offers further possibilities for the creation of domain walls.

Additionally, we investigated which types of domain walls introduced into a 3Q-ordered magnetic layer result in the occurrence of Majorana edge modes at the domain walls. A domain wall stemming from spatial shifts along the two lattice vectors of the investigated triangular lattice leads to the conclusion that this type of domain wall does not produce any edge modes. However, the band structures suggest that stronger spatial shifts, which could be realized for more complicated magnetic structures such as skyrmionic lattices, could result in emerging edge modes.

Nevertheless, domain walls at which the spin structure is inverted produce a change of sign for the Chern number  $C$  and thereby result in the occurrence of  $2|C|$  edge modes. These were observed in the theoretical simulations of the band structure for a ribbon of magnetic adatoms. The LDOS as well as the supercurrents confirm the emergence of edge modes in this scenario, which offers two promising options for an experimental assessment.

However, the supercurrents are the more suitable candidate from an experimental point of view. The results for a  $\pi$ -phase domain wall, where the superconducting order parameter is inverted, exhibit trivial in-gap modes that show a strong localization at the domain wall as well. Their trivial character can be distinguished from the topological one of the former case through the calculated supercurrents. These cancel out for the  $\pi$ -phase domain wall, while the sum remains finite for the spin inversion domain wall.

Finally, we investigated the effects of magnetic perturbations on a metallic as well as a superconducting site connected to an STM tip by employing the Keldysh formalism. For the case of a metallic site, the results for the simulated current between the site and the tip shows a strongly oscillating current for a  $\delta$ -pulse perturbation, which slowly relaxes back to its equilibrium value. The derivative of the current by the bias voltage is proportional to the density of states in equilibrium. The perturbed version shows a decreased value for bias voltages below the van-Hove singularity and increased values above. This derivative also returns back to its equilibrium value

---

over time.

For superconducting sites, we first tested whether a Shiba state can be detected in the current's derivative for a constant perturbation. While an approach, where order by order is included into the calculation, leads to unphysical values and divergences in the derivative of the current, a  $\hat{T}$ -matrix approach proves successful in calculating the emerging Shiba state in the superconducting gap. Employing this method, the exact location of the Shiba state was calculated for a large range of magnetic perturbation strengths, which showed how the Shiba state moves from one side of the superconducting gap to the other with increasing perturbation strength.

An equivalent method using a  $\hat{T}$ -matrix was then developed for  $\delta$ -pulse perturbations. However, the calculated derivative of the current does not exhibit any Shiba states for this scenario, but instead shows negative values on the right side of the superconducting gap. In how far this result still relates to the density of states as it does in the equilibrium, remains unclear so far. In order to understand this phenomenon, further investigations in this direction are required.

Finally, the response of the superconducting order parameter to a  $\delta$ -pulse perturbation was analyzed. Just like the current between the tip and the site, the order parameter shows a strong oscillation after the perturbation. Furthermore, the order parameter, which was entirely real before the perturbation, becomes complex during the process. The imaginary part relaxes back to zero and the real part back to the equilibrium value, as can be expected since the perturbation is only applied for a very short time.

Overall, further investigations in this direction could enable a simulation of moving quantum vortices, so that it is useful to further develop the methods introduced here.

## Bibliography

- [1] E. Majorana, “Teoria simmetrica dell’elettrone e del positrone”, *Il Nuovo Cimento* (1924-1942) **14**, 171 (2008).
- [2] C. Nayak, S. H. Simon, A. Stern, M. Freedman, and S. Das Sarma, “Non-Abelian anyons and topological quantum computation”, *Rev. Mod. Phys.* **80**, 1083 (2008).
- [3] C. Beenakker, “Search for Majorana Fermions in Superconductors”, *Annual Review of Condensed Matter Physics* **4**, 113 (2013), eprint: <https://doi.org/10.1146/annurev-conmatphys-030212-184337>.
- [4] M. Leijnse and K. Flensberg, “Introduction to topological superconductivity and Majorana fermions”, *Semiconductor Science and Technology* **27**, 124003 (2012).
- [5] A. Y. Kitaev, “Unpaired Majorana fermions in quantum wires”, *Physics-Uspekhi* **44**, 131 (2001).
- [6] T.-P. Choy, J. M. Edge, A. R. Akhmerov, and C. W. J. Beenakker, “Majorana fermions emerging from magnetic nanoparticles on a superconductor without spin-orbit coupling”, *Phys. Rev. B* **84**, 195442 (2011).
- [7] I. Martin and A. F. Morpurgo, “Majorana fermions in superconducting helical magnets”, *Phys. Rev. B* **85**, 144505 (2012).
- [8] J. Klinovaja, P. Stano, A. Yazdani, and D. Loss, “Topological Superconductivity and Majorana Fermions in RKKY Systems”, *Phys. Rev. Lett.* **111**, 186805 (2013).
- [9] F. Pientka, L. I. Glazman, and F. von Oppen, “Topological superconducting phase in helical Shiba chains”, *Phys. Rev. B* **88**, 155420 (2013).
- [10] S. Nadj-Perge, I. K. Drozdov, J. Li, H. Chen, S. Jeon, J. Seo, A. H. MacDonald, B. A. Bernevig, and A. Yazdani, “Observation of Majorana fermions in ferromagnetic atomic chains on a superconductor”, *Science* **346**, 602 (2014).
- [11] M. Ruby, F. Pientka, Y. Peng, F. von Oppen, B. W. Heinrich, and K. J. Franke, “End States and Subgap Structure in Proximity-Coupled Chains of Magnetic Adatoms”, *Phys. Rev. Lett.* **115**, 197204 (2015).

- 
- [12] R. Pawlak, M. Kisiel, J. Klinovaja, T. Meier, S. Kawai, T. Glatzel, D. Loss, and E. Meyer, “Probing atomic structure and Majorana wavefunctions in mono-atomic Fe chains on superconducting Pb surface”, *npj Quantum Information* **2** (2016).
- [13] H. Kim, A. Palacio-Morales, T. Posske, L. Rózsa, K. Palotás, L. Szunyogh, M. Thorwart, and R. Wiesendanger, “Toward tailoring Majorana bound states in artificially constructed magnetic atom chains on elemental superconductors”, *Science Advances* **4** (2018), eprint: <https://advances.sciencemag.org/content/4/5/eaar5251.full.pdf>.
- [14] J. Röntynen and T. Ojanen, “Topological Superconductivity and High Chern Numbers in 2D Ferromagnetic Shiba Lattices”, *Physical Review Letters* **114**, 236803 (2015).
- [15] J. Li, T. Neupert, Z. Wang, A. H. Macdonald, A. Yazdani, and B. Andrei Bernevig, “Two-dimensional chiral topological superconductivity in Shiba lattices”, *Nature Communications* **7** (2016).
- [16] S. Rachel, E. Mascot, S. Cocklin, M. Vojta, and D. K. Morr, “Quantized charge transport in chiral Majorana edge modes”, *Phys. Rev. B* **96**, 205131 (2017).
- [17] E. Mascot, S. Cocklin, S. Rachel, and D. K. Morr, “Dimensional tuning of Majorana fermions and real space counting of the Chern number”, *Physical Review B* **100** (2019).
- [18] V. Mourik, K. Zuo, S. Frolov, S. Plissard, E. Bakkers, and L. Kouwenhoven, “Signatures of Majorana fermions in hybrid superconductor-semiconductor nanowire devices”, *Science* **336**, 1003 (2012).
- [19] G. C. Ménard, S. Guissart, C. Brun, R. T. Leriche, M. Trif, F. Debontridder, D. Demaille, D. Roditchev, P. Simon, and T. Cren, “Two-dimensional topological superconductivity in Pb/Co/Si(111)”, *Nat. Commun.* **8**, 2040 (2017), eprint: 1607.06353.
- [20] T. Machida, Y. Sun, S. Pyon, S. Takeda, Y. Kohsaka, T. Hanaguri, T. Sasagawa, and T. Tamegai, “Zero-energy vortex bound state in the superconducting topological surface state of Fe(Se,Te)”, *Nature Materials* **18**, 811 (2019).
- [21] G. Ménard, A. Mesaros, C. Brun, F. Debontridder, D. Roditchev, P. Simon, and T. Cren, “Isolated pairs of Majorana zero modes in a disordered superconducting lead monolayer”, *Nature Communications* **10**, 2587 (2019).
- [22] Z. Wang, J. O. Rodriguez, L. Jiao, S. Howard, M. Graham, G. Gu, T. L. Hughes, D. K. Morr, and V. Madhavan, “Evidence for dispersing 1D Majorana channels in an iron-based superconductor”, *Science (New York, N.Y.)* **367**, 104 (2020).

- [23] A. Palacio-Morales, E. Mascot, S. Cocklin, H. Kim, S. Rachel, D. K. Morr, and R. Wiesendanger, “Atomic-scale interface engineering of Majorana edge modes in a 2D magnet-superconductor hybrid system”, *Science Advances* **5** (2019), eprint: <https://advances.sciencemag.org/content/5/7/eaav6600.full.pdf>.
- [24] E. Mascot, J. Bedow, M. Graham, S. Rachel, and D. K. Morr, *Topological Superconductivity in Skyrmion Lattices*, 2020, arXiv:2005.00027 [cond-mat.supr-con].
- [25] P. Kurz, G. Bihlmayer, K. Hirai, and S. Blügel, “Three-Dimensional Spin Structure on a Two-Dimensional Lattice: Mn/Cu(111)”, *Phys. Rev. Lett.* **86**, 1106 (2001).
- [26] J. Spethmann, S. Meyer, K. von Bergmann, R. Wiesendanger, S. Heinze, and A. Kubetzka, “Discovery of magnetic single- and triple-Q states in Mn/Re(0001)”, (2020), arXiv:2003.02210.
- [27] N. B. Kopnin and M. M. Salomaa, “Mutual friction in superfluid  $^3\text{He}$ : Effects of bound states in the vortex core”, *Phys. Rev. B* **44**, 9667 (1991).
- [28] G. E. Volovik, “Fermion zero modes on vortices in chiral superconductors”, *Journal of Experimental and Theoretical Physics Letters* **70**, 609 (1999).
- [29] N. Read and D. Green, “Paired states of fermions in two dimensions with breaking of parity and time-reversal symmetries and the fractional quantum Hall effect”, *Phys. Rev. B* **61**, 10267 (2000).
- [30] D. A. Ivanov, “Non-Abelian Statistics of Half-Quantum Vortices in  $p$ -Wave Superconductors”, *Phys. Rev. Lett.* **86**, 268 (2001).
- [31] H. Shiba, “Classical Spins in Superconductors”, *Progress of Theoretical Physics* **40**, 435 (1968), eprint: <https://academic.oup.com/ptp/article-pdf/40/3/435/5185550/40-3-435.pdf>.
- [32] A. I. Rusinov, “On the Theory of Gapless Superconductivity in Alloys Containing Paramagnetic Impurities”, *Journal of Experimental and Theoretical Physics* **29** (1969).
- [33] K. von Klitzing, “The quantized Hall effect”, *Rev. Mod. Phys.* **58**, 519 (1986).
- [34] K. v. Klitzing, G. Dorda, and M. Pepper, “New Method for High-Accuracy Determination of the Fine-Structure Constant Based on Quantized Hall Resistance”, *Phys. Rev. Lett.* **45**, 494 (1980).
- [35] D. J. Thouless, M. Kohmoto, M. P. Nightingale, and M. den Nijs, “Quantized Hall Conductance in a Two-Dimensional Periodic Potential”, *Phys. Rev. Lett.* **49**, 405 (1982).
- [36] M. Kohmoto, “Topological invariant and the quantization of the Hall conductance”, *Annals of Physics* **160**, 343 (1985).

- 
- [37] Q. Niu, D. J. Thouless, and Y.-S. Wu, “Quantized Hall conductance as a topological invariant”, *Phys. Rev. B* **31**, 3372 (1985).
- [38] M. Ezawa, Y. Tanaka, and N. Nagaosa, “Topological Phase Transition without Gap Closing”, *Scientific Reports* **3** (2013).
- [39] S. Ryu and Y. Hatsugai, “Topological Origin of Zero-Energy Edge States in Particle-Hole Symmetric Systems”, *Phys. Rev. Lett.* **89**, 077002 (2002).
- [40] R. S. K. Mong and V. Shivamoggi, “Edge states and the bulk-boundary correspondence in Dirac Hamiltonians”, *Phys. Rev. B* **83**, 125109 (2011).
- [41] T. Fukui, K. Shiozaki, T. Fujiwara, and S. Fujimoto, “Bulk-Edge Correspondence for Chern Topological Phases: A Viewpoint from a Generalized Index Theorem”, *Journal of the Physical Society of Japan* **81**, 114602 (2012), eprint: <https://doi.org/10.1143/JPSJ.81.114602>.
- [42] B. A. BERNEVIG and T. L. Hughes, *Topological Insulators and Topological Superconductors*, STU - Student edition (Princeton University Press, 2013).
- [43] A. Kitaev, V. Lebedev, and M. Feigel'man, “Periodic table for topological insulators and superconductors”, *AIP Conference Proceedings* (2009).
- [44] M. R. Zirnbauer, “Riemannian symmetric superspaces and their origin in random-matrix theory”, *Journal of Mathematical Physics* **37**, 4986 (1996), eprint: <https://doi.org/10.1063/1.531675>.
- [45] A. Altland and M. R. Zirnbauer, “Nonstandard symmetry classes in mesoscopic normal-superconducting hybrid structures”, *Phys. Rev. B* **55**, 1142 (1997).
- [46] A. P. Schnyder, S. Ryu, A. Furusaki, and A. W. W. Ludwig, “Classification of topological insulators and superconductors in three spatial dimensions”, *Phys. Rev. B* **78**, 195125 (2008).
- [47] M. Nakahara, *Differentialgeometrie, Topologie und Physik* (Springer Spektrum, Berlin, Heidelberg, 2015).
- [48] E. Prodan, T. L. Hughes, and B. A. Bernevig, “Entanglement Spectrum of a Disordered Topological Chern Insulator”, *Phys. Rev. Lett.* **105**, 115501 (2010).
- [49] A. M. Clogston, “Upper Limit for the Critical Field in Hard Superconductors”, *Phys. Rev. Lett.* **9**, 266 (1962).
- [50] B. S. Chandrasekhar, “A NOTE ON THE MAXIMUM CRITICAL FIELD OF HIGH-FIELD SUPERCONDUCTORS”, *Applied Physics Letters* **1**, 7 (1962), eprint: <https://doi.org/10.1063/1.1777362>.
- [51] D. K. Morr, Personal Communication, Dec. 17, 2019.
- [52] M. Stone and R. Roy, “Edge modes, edge currents, and gauge invariance in  $p_x+ip_y$  superfluids and superconductors”, *Physical Review B* **69** (2004).

- [53] C. Kallin and J. Berlinsky, “Chiral superconductors”, *Reports on Progress in Physics* **79**, 054502 (2016).
- [54] G. D. Mahan, *Many-particle physics* (Plenum Press New York, 1981), p. 97.
- [55] D. K. Morr, Personal Communication, Apr. 23, 2020.
- [56] J. Bedow, E. Mascot, T. Posske, G. S. Uhrig, R. Wiesendanger, S. Rachel, and D. K. Morr, *Topological superconductivity induced by a triple-Q magnetic structure*, 2020, arXiv:2006.02039 [cond-mat.supr-con].
- [57] C. Grossmann, H.-G. Roos, and M. Stynes, *Numerical treatment of partial differential equations. Revised translation of the 3rd German edition of ‘Numerische Behandlung partieller Differentialgleichungen’ by Martin Stynes* (Jan. 2007), p. 23.
- [58] E. Prodan, “Disordered Topological Insulators: A Non-Commutative Geometry Perspective”, (2010), arXiv:1010.0595.
- [59] B. Fornberg, in *Numerical Modeling of Seismic Wave Propagation: Gridded Two-way Wave-equation Methods* (Society of Exploration Geophysicists, Jan. 2012).
- [60] B. Nijholt, J. Weston, J. Hoofwijk, and A. Akhmerov, *Adaptive: parallel active learning of mathematical functions*, 2019.
- [61] W. R. Inc., *Mathematica, Version 12.1*, Champaign, IL, 2020.
- [62] C. W. Groth, M. Wimmer, A. R. Akhmerov, and X. Waintal, “Kwant: a software package for quantum transport”, *New Journal of Physics* **16**, 063065 (2014).
- [63] E. Mascot, Personal Communication, Oct. 4, 2019.
- [64] H.-Y. Hui, J. Sau, and S. Das Sarma, “Generalized Eilenberger theory for Majorana zero-mode-carrying disordered p-wave superconductors”, *Physical Review B* **90** (2014).
- [65] P. Kaghazchi and T. Jacob, “Structure of rhenium surfaces in an oxygen environment”, *Phys. Rev. B* **83**, 035417 (2011).
- [66] K. Everschor-Sitte, J. Masell, R. M. Reeve, and M. Kläui, “Perspective: Magnetic skyrmions—Overview of recent progress in an active research field”, *Journal of Applied Physics* **124**, 240901 (2018), eprint: <https://doi.org/10.1063/1.5048972>.
- [67] N. Romming, C. Hanneken, M. Menzel, J. Bickel, B. Wolter, K. von Bergmann, A. Kubetzka, and R. Wiesendanger, “Writing and Deleting Single Magnetic Skyrmions”, *Science (New York, N.Y.)* **341**, 636 (2013).
- [68] E. Mascot, Personal Communication, Nov. 11, 2019.

- 
- [69] A. Kitaev, “Fault-tolerant quantum computation by anyons”, *Annals of Physics* **303**, 2 (2003).
- [70] L. V. Keldysh, “Diagram Technique for Nonequilibrium Processes”, *Journal of Experimental and Theoretical Physics* **20**, 1018 (1964).
- [71] B. H. November, J. D. Sau, J. R. Williams, and J. E. Hoffman, *Scheme for Majorana Manipulation Using Magnetic Force Microscopy*, 2019, arXiv:1905.09792 [cond-mat.supr-con].
- [72] G. Stefanucci and R. van Leeuwen, *Nonequilibrium Many-Body Theory of Quantum Systems: A Modern Introduction* (Cambridge University Press, 2013).
- [73] J. Rammer and H. Smith, “Quantum field-theoretical methods in transport theory of metals”, *Rev. Mod. Phys.* **58**, 323 (1986).
- [74] C. Caroli, R. Combescot, P. Nozieres, and D. Saint-James, “Direct calculation of the tunneling current”, *Journal of Physics C: Solid State Physics* **4**, 916 (1971).
- [75] N. Hatter, B. W. Heinrich, M. Ruby, J. I. Pascual, and K. J. Franke, “Magnetic anisotropy in Shiba bound states across a quantum phase transition”, *Nature Communications* **6** (2015).
- [76] A. Yazdani, B. A. Jones, C. P. Lutz, M. F. Crommie, and D. M. Eigler, “Probing the Local Effects of Magnetic Impurities on Superconductivity”, *Science* **275**, 1767 (1997), eprint: <https://science.sciencemag.org/content/275/5307/1767.full.pdf>.
- [77] E. A. Yuzbashyan, B. L. Altshuler, V. B. Kuznetsov, and V. Z. Enolskii, “Nonequilibrium cooper pairing in the nonadiabatic regime”, *Phys. Rev. B* **72**, 220503 (2005).
- [78] J. Bardeen, L. N. Cooper, and J. R. Schrieffer, “Theory of Superconductivity”, *Phys. Rev.* **108**, 1175 (1957).
- [79] N. Bogolyubov, “A New method in the theory of superconductivity. I”, *Sov. Phys. JETP* **7**, 41 (1958).
- [80] M. Graham and D. K. Morr, “Imaging the spatial form of a superconducting order parameter via Josephson scanning tunneling spectroscopy”, *Phys. Rev. B* **96**, 184501 (2017).



## Acknowledgements

I would like to express my gratitude towards a number of colleagues and friends that have helped me during the course of my masters studies.

Firstly and above all, I would like to thank my supervisors Götz Uhrig and Dirk Morr for their guidance and support in writing this thesis and for introducing me to the intriguing field of topological superconductivity. During the course of the last year, I have profited immensely from their expertise and I have learned so much from them. It was also a huge honour to be given the chance to study both at TU Dortmund University as well as the University of Illinois at Chicago. Here, I would also like to express my gratitude towards the *Studienstiftung des deutschen Volkes*, as their funding of my stay abroad not only allowed me to concentrate fully on my research, but also made one of the fondest memories I now hold possible.

In Chicago, I would like to thank Eric Mascot who welcomed me on my very first day and immediately helped me to start my research. Not only did he answer all of my many questions regarding both topological superconductors and programming, but also showed me the very first restaurants I knew in Chicago.

In Dortmund, I would like to thank my colleagues Vanessa Sulaiman, Leanna Müller and Joachim Stolze. Vanessa Sulaiman, with whom I shared an office, most of the time virtually, always discussed my problems with me, proofread my research representations and offered words of encouragement, even when I was 6000 miles away. Furthermore, Leanna Müller always had words of encouragement for me and was a huge inspiration to me. Finally, Joachim Stolze was a great mentor to me throughout all of my studies. I owe him great thanks for all of his advice and support.

Outside of the research group, I owe great thanks to my friends Carlo Tasillo, Katharina Klioba, Philippe Suchsland, Anno Knierim, Jan Ellbracht and Kay Wohlfarth. All of them partially or completely, in the case of Carlo Tasillo, proofread this thesis despite their busy schedules and without them, this work would have contained many more mistakes than it probably still does. Next, my thanks goes out to my best virtual huggers and sponsors of chocolate and coffee, Anneke Reinold, Janina Bolles and Talea von Essen, who were always there for me, sat in coffee shops with me for hours and sent postcards back and forth with me.

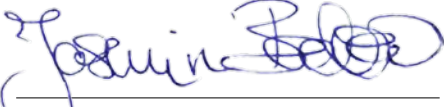
Last but not least, I would like to thank my parents Birgit and Rüdiger and my sister Alice for their continued support and their endless encouragement to pursue my dreams. They really went through all the good and bad times with me during this last year and this would not have been possible without the three of them. Thank you guys for everything.

## Eidesstattliche Versicherung

Ich versichere hiermit an Eides statt, dass ich die vorliegende Abschlussarbeit mit dem Titel "Edge Modes in Magnet-Superconductor Hybrid Structures" selbstständig und ohne unzulässige fremde Hilfe erbracht habe. Ich habe keine anderen als die angegebenen Quellen und Hilfsmittel benutzt, sowie wörtliche und sinngemäße Zitate kenntlich gemacht. Die Arbeit hat in gleicher oder ähnlicher Form noch keiner Prüfungsbehörde vorgelegen.

Essen, 12. August 2020

Ort, Datum



---

Unterschrift

## Belehrung

Wer vorsätzlich gegen eine die Täuschung über Prüfungsleistungen betreffende Regelung einer Hochschulprüfungsordnung verstößt, handelt ordnungswidrig. Die Ordnungswidrigkeit kann mit einer Geldbuße von bis zu 50 000 € geahndet werden. Zuständige Verwaltungsbehörde für die Verfolgung und Ahndung von Ordnungswidrigkeiten ist der Kanzler/die Kanzlerin der Technischen Universität Dortmund. Im Falle eines mehrfachen oder sonstigen schwerwiegenden Täuschungsversuches kann der Prüfling zudem exmatrikuliert werden (§ 63 Abs. 5 Hochschulgesetz –HG–).

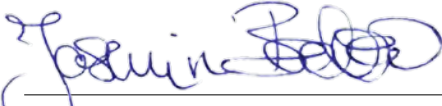
Die Abgabe einer falschen Versicherung an Eides statt wird mit Freiheitsstrafe bis zu 3 Jahren oder mit Geldstrafe bestraft.

Die Technische Universität Dortmund wird ggf. elektronische Vergleichswerkzeuge (wie z. B. die Software "turnitin") zur Überprüfung von Ordnungswidrigkeiten in Prüfungsverfahren nutzen.

Die oben stehende Belehrung habe ich zur Kenntnis genommen.

Essen, 12. August 2020

Ort, Datum



---

Unterschrift